CHAPTER 9

Growth and Characterization of MBE-Grown Cubic GaN, $In_xGa_{1-x}N$, and $Al_yGa_{1-y}N$

D.J. AS

Universität Paderborn, FB-6 Physik, Warburger Strasse 100, D-33095 Paderborn, Germany;
E-mail: d.as@uni-paderborn.de

9.1 INTRODUCTION . . . 325
9.2 ELECTRONIC STRUCTURE AND BASIC PROPERTIES OF CUBIC GROUP III-NITRIDES . . . 327
9.3 GROWTH OF CUBIC GaN . . . 332
9.3.1 Selection of a Suitable Substrate . . . 332
9.3.2 Growth Methods . . . 334
9.3.2.1 HVPE . . . 335
9.3.2.2 MOCVD . . . 335
9.3.2.3 MBE . . . 336
9.3.3 Plasma-Assisted MBE . . . 338
9.4 CHARACTERIZATION OF NOMINALLY UNDOPED CUBIC GaN . . . 345
9.4.1 Phase Purity . . . 345
9.4.2 Structural Properties . . . 346
9.4.2.1 TEM measurements . . . 346
9.4.2.2 X-ray measurements . . . 348
9.4.2.3 Rutherford backscattering . . . 350
9.4.3 Optical Properties . . . 352
9.4.3.1 Refractive index and extinction coefficient . . . 352
9.4.3.2 PL data . . . 353

9.4.3.3 Cathodoluminescence (CL) data 360
9.4.4 Stimulated Emission and Optical Gain 362
9.4.5 Electrical Properties 366
9.4.6 As: An Isoelectronic Impurity or An Ideal Surfactant 373
9.5 *p*-TYPE DOPING OF CUBIC GaN 378
9.5.1 Theoretical Aspects of Different Acceptors . . . 378
9.5.2 Doping of Cubic GaN by Mg 380
9.5.2.1 Incorporation of the Mg acceptor 380
9.5.2.2 Optical properties of the Mg acceptor . . 382
9.5.2.3 Electrical properties of the Mg acceptor . 384
9.5.3 Alternative Acceptors 387
9.6 *n*-TYPE DOPING OF CUBIC GaN 389
9.6.1 Theoretical Aspects of Different Donors 389
9.6.2 Doping of Cubic GaN by Si 390
9.6.2.1 Incorporation of the Si donor 390
9.6.2.2 Optical properties of Si-doped cubic GaN 391
9.6.2.3 Electrical properties of the Si donor . . . 394
9.6.3 Alternative Donors 397
9.7 *p-n* HOMOJUNCTION OF CUBIC GaN 398
9.8 GROWTH AND CHARACTERIZATION OF MBE-GROWN CUBIC $In_xGa_{1-x}N$ 404
9.8.1 Growth of Cubic $In_xGa_{1-x}N$ 405
9.8.2 Structural and Vibrational Properties 407
9.8.3 Optical Properties 412
9.8.4 Optical Gain 416
9.8.5 Electrical Properties 419
9.8.6 Phase-Separation in Cubic $In_xGa_{1-x}N$ 422
9.8.7 In: An Ideal Surfactant? 427
9.9 GROWTH AND CHARACTERIZATION OF MBE GROWN CUBIC $Al_yGa_{1-y}N$ 429
9.9.1 Growth of Cubic $Al_yGa_{1-y}N$ 429
9.9.2 Structural and Vibrational Properties 430
9.9.3 Optical and Electrical Properties 435
9.10 CONCLUSIONS 439
Acknowledgments 441
References 441

9.1 INTRODUCTION

The metastable cubic phase of group-III nitrides (GaN, AlN, InN) offers interesting technological advantages compared with its hexagonal modification [1,2]. Specifically, epitaxially grown layers of cubic GaN (*c*-GaN) lend themselves to the production of cleaved laser cavities. As cubic crystals have higher crystallographic symmetry the *c*-III-nitrides are expected to show different electronic and optical properties (bandgap, impurity levels, electron drift velocity, etc.). Cubic GaN can further be grown on (001) substrates, eliminating the influence of piezoelectric (PZ) fields on the optical and electrical properties. Due to the smaller bandgap of *c*-GaN, the visible (blue and green) spectral region will further require smaller amounts of In than in the case of the hexagonal phase [3]. Gain and stimulated emission experiments on cleaved *c*-GaN underline the possible application of this material for laser diodes [4]. Recently, the first *c*-GaN based blue light-emitting diodes (LEDs) grown on GaAs substrates were demonstrated by Yang and colleagues [5] and As and colleagues [6]. For electronic devices such as high electron mobility transistors (HEMTs), cubic GaN has the potential of a high saturated electron drift velocity. This property could increase its applicability for high-frequency devices. The large bandgaps of these nitrides further predestinates them to be used at high temperatures and high powers and its chemical stability enables applications in hostile environments. Finally, cubic III-nitrides are primarily grown on GaAs or Si substrates, which further enables possible future integration of III-nitrides with advanced GaAs or Si technology.

Several different growth techniques, such as molecular beam epitaxy (MBE), metalorganic chemical vapor deposition (MOCVD), and hydride vapor-phase epitaxy (HVPE), have successfully been used to grow cubic group III-nitrides on various cubic substrates (GaAs, ß-SiC, Si, GaP, and MgO) [1]. One particular difficulty, which is similar to hexagonal GaN (*h*-GaN), is the absence of a readily available, thermodynamically stable, single-crystal phase for homoepitaxy. Thus, heteroepitaxy is a practical necessity with all its drawbacks, and the choice of substrate is critical. The large misfit in lattice constants of the used substrates to the group III-nitrides (in the case of GaAs, 20 percent) introduces a large number of extended defects which severely degrade the crystal quality of the material. As a figure of merit for crystal quality, the linewidth of the x-ray diffraction profile taken in the ω-mode across the lowest order symmetric reflection is frequently used. The linewidth of this reflection is, in fact, almost two orders of magnitude larger for *c*-GaN ($30'$) compared with that measured for *h*-GaN ($1'$) of similar thickness [7]. Even when considering that symmetric reflections are insensitive to threading dislocations, asymmetric reflections are still as broad as $3'$ for *h*-GaN, and thus still an order of magnitude below the best values

of c-GaN. In addition, one should have in mind that the crystal quality of h-GaN is still far from that of state-of-the-art GaAs or Si epilayers. Threading dislocations densities in excess of 10^{10} cm^{-2} are therefore reported in both h-GaN and c-GaN. Nevertheless, LEDs having an impressively high quantum efficiency are fabricated on the basis of this highly defective materials [8]. This implies that, at least in h-GaN the structural defects are much less detrimental to the optical properties than in other semiconductors such as GaAs or InP. Because the electronic impact of extended defects in hexagonal material may differ from that in cubic material, it is not clear if the extended defects present in cubic group III-nitrides are of a similarly forgiving nature as those in the hexagonal counterparts.

Due to the metastability of the zincblende phase of group III-nitrides, a major difficulty in the growth of c-III-nitrides originates from the polytypism and, as a result, an increased tendency of forming wurtzite-phase subdomains within the cubic lattice. Growth conditions far from thermodynamical equilibrium are therefore advantageous to synthesize phase pure cubic epilayers. In addition, it has been recognized that precise control of stoichiometry is of critical importance in determining material properties [7,9]. This predestinates MBE with its possibility to carefully control the growth process in situ by reflection high-energy electron diffraction (RHEED) for the growth of cubic group III-nitrides. Indeed, MBE has played a major role in the growth of zincblende III-nitrides and, under optimized conditions, a phase purity better than 99.9 percent has been demonstrated for c-GaN epilayers [10].

The two prerequisites for optoelectronic applications of cubic III-nitrides are the fabrication of the required alloys $In_{1-x}Ga_xN$ and $Al_{1-y}Ga_yN$ and their heterostructures and p-type and n-type doping of all group III-nitrides. However, little work has been done on these topics [11–17]. The growth of c-$In_{1-x}Ga_xN$ layers is extremly difficult for several reasons: first, because of the metastability of the cubic phase itself, and second due to strong spatial fluctuations of the In-content caused by spinodal decomposition of the material [15]. In additon, a strong variation of the sticking coefficient of In with temperature further complicates the epitaxial growth [16]. Cubic $Al_{1-y}Ga_yN$ alloys seem not to suffer on phase separation problems, however, the strong affinity of Al to O may cause a strong residual n-type background doping. Quantum well (QW) structures based on cubic nitrides are still absent. Up to now, only c-GaN has been investigated with respect of n-type and p-type doping by Si [18,19] and Mg [20–22], respectively. Si acts as a shallow donor and can easily be incorporated in c-GaN up to concentrations of more than 5×10^{19} cm^{-3} [19]. p-type doping by Mg suffers on self-compensation, segregation, and solubility effects which limit the room-temperature hole concentration to the low 10^{17} cm^{-3} range. p-type doping by Mg under N-rich growth conditons, which has been shown to be benefitable in Mg-doping of hexagonal GaN, results in increased hexagonal inclusions [21,22]. A novel

and perhaps promising approach to p-type doping has been reported recently [23], where co-doping of c-GaN by Be and O was shown. Doping of the alloys is still lacking.

This chapter will concentrate on heteroepitaxy of cubic III-nitrides on GaAs (001) substrates grown by MBE, and review recent results on c-GaN and the cubic alloys $In_xGa_{1-x}N$ and $Al_yGa_{1-y}N$. Doping experiments of c-GaN with Mg and Si are reported and the influence of the large number of extended defects on the optical and electrical properties is discussed. The experimental data reported were obtained with samples grown by radio frequency (RF)-plasma-assisted MBE at the University of Paderborn.

In recent years, several excellent books with review papers have appeared addressing various aspects of primarily hexagonal III-V nitrides technology, physics, and applications [24–29]. Current news in this research area is available on the World Wide Web [30].

9.2 ELECTRONIC STRUCTURE AND BASIC PROPERTIES OF CUBIC GROUP III-NITRIDES

In addition to the commonly appearing hexagonal (wurtzite, or α-polytype) crystal structure all group III-nitrides form the thermodynamically less-stable zincblende modification, which is also known as sphalerite, or ß-polytype. It is the metastable form of the group III-nitrides, which has been stabilized by epitaxial growth of thin films on the (001) crystal planes of cubic substrates such as Si, SiC, GaAs, GaP, and MgO.

The zincblende structure has a cubic unit cell, containing three group III elements (Al, Ga, In) and four nitrogen elements (Figure 9.1). The space grouping for the zincblende structure is $\bar{F}43m$ (T_d^2). The position of the atoms within the unit cell is identical to the diamond crystal structure; both structures consist of two interpenetrating face centered cubic (fcc) sublattices, offset by one-quarter of the distance along a body diagonal.

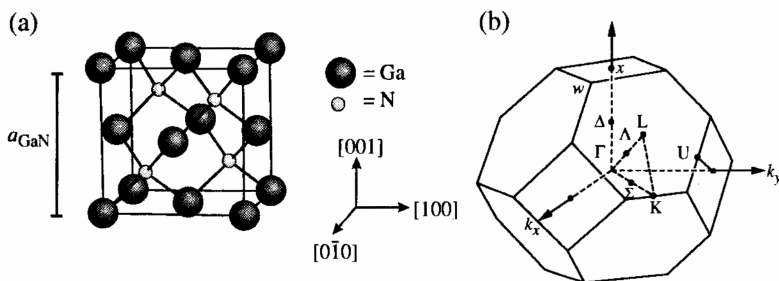

Figure 9.1 (a) Ball and stick model of the zinc blende structure of cubic GaN; (b) 1. Brillouin zinc of the zincblende structure.

Each atom in the structure may be viewed as positioned at the center of a tetrahedron, with its four nearest neighbors defining the four corners of the tetrahedron. The bond length, R_{cub}, is therefore connected to the cubic lattice constant, a_{cub}, by $R_{cub} = \sqrt{3}/4 \cdot a_{cub}$. The main difference in the stable hexagonal structure is the stacking sequence of closed packed diatomic planes. Whereas for the hexagonal structure, the stacking sequence of (0001) planes is ABABAB in the $\langle 0001 \rangle$ direction, the stacking sequences of (111) planes is ABCABC in the $\langle 11\bar{1} \rangle$ direction for zincblende structure. This difference occurs due to an eclipsed bond configuration of the second nearest neighbors in the wurtzite structure, whereas in the zincblende structure the bonding configuration is staggered. All group III-nitrogen bond lengths are equivalent in the zincblende structure but there are two slightly different bond lengths in the wurtzite structure. Because the wurtzite structure has an hexagonal unit cell, it is thus characterized by two different lattice constants, c_{hex} and a_{hex}. One bond length R_{hex} is equal to $u \cdot c_{hex}$, whereas the other three bonds are equal to

$$a_{hex} \cdot \left[\frac{1}{3} + \left(\frac{1}{2} - u \right)^2 \cdot \left(\frac{c_{hex}}{a_{hex}} \right)^2 \right]^{1/2} \tag{9.1}$$

where u is a dimensionless cell internal structure parameter. For an ideal wurtzite structure $u = 8/3$ and $c_{hex}/a_{hex} = \sqrt{8/3}$. In real crystals, u and c_{hex}/a_{hex} deviate from these values; for h-AlN, h-GaN, and h-InN, c_{hex}/a_{hex} is slightly less.

For the ideal structures, therefore, the lattice constant of cubic and hexagonal crystals are correlated by a simple expression by

$$a_{cub} = \sqrt[3]{\sqrt{3} \cdot a_{hex}^2 \cdot c_{hex}} \tag{9.2}$$

which allows the calculation of the cubic lattice parameters from the more studied hexagonal parameter.

In addition, the cubic lattice constant can further be estimated from the covalent radii of group III elements and N by

$$a_{cub} = \frac{4}{\sqrt{3}} \cdot (r_{cov_{\mathrm{III}}} + r_{cov_{\mathrm{N}}}) \tag{9.3}$$

The covalent radii of the four elements Al, Ga, In, and N are 1.25 Å, 1.26 Å, 1.50 Å, and 0.70 Å, respectively, resulting in cubic lattice constants of 4.50 Å, 4.53 Å, and 5.08 Å for c-AlN, c-GaN, and c-InN. As a representative for all group III-nitrides, the crystal structure of cubic GaN is shown in Figure 9.1 (left picture). One immediately sees that the size of the N-atom

is much smaller than that of any group III element. This has important consequences for doping, as we will see later, because the dopant has to fit to the replaced atom. Otherwise large deformations within the crystal structure may occur, which may hinder the incorporation of the dopant species, resulting in insufficient *p*-type or *n*-type conductivity of the semiconductor.

The first Brillouin zone of the zincblende crystal structure is also shown in Figure 9.1 (right picture). Included in this plot are the most important points (Γ, L, U, X, W, and K—full points) as well as the directions (Λ, Σ, Δ, Q, and Z—open points at the center of the lines) in the reciprocal space, which are important for band structure calculations.

Band structure calculations of cubic group III-nitrides have been performed by several different groups using various theoretical approaches [31,32]. A summary and comparison of the results are given by Lambrecht and Segall [33], and by Suzuki and Uenoyama [34]. Within all these different approaches, pseudo-potential theory incorporating self-interaction and relaxation corrections (SIRC-PP) [32] are in reasonable agreement with available experimental data. The band structure of cubic GaN calculated using Ab-inito SIRC and Tight binding $sp^3s^*d^5$ are shown in Figure 9.2 [35].

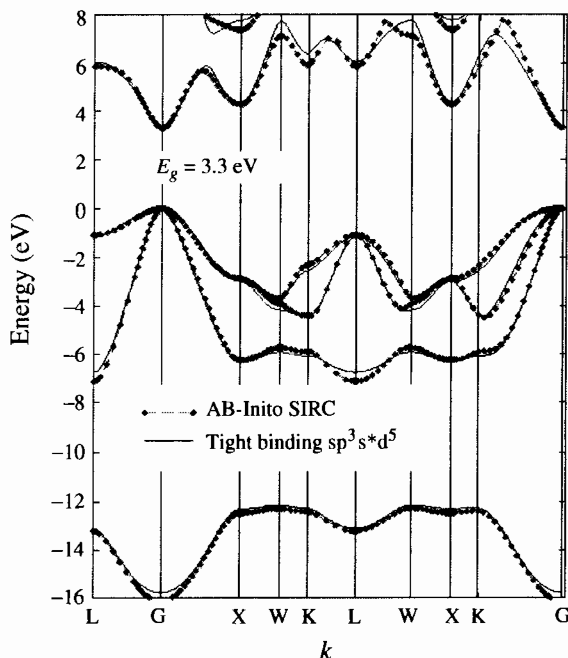

Figure 9.2 Band diagram calculated for cubic GaN. The calculations were performed using the method of Vogel et al. [32] by F. de Salla and F. Scholz (private communication).

A direct bandgap of 3.3 eV at the Γ-point of the Brillouin zone is estimated. Whereas cubic GaN and cubic InN are direct semiconductors, cubic AlN shows an indirect behavior. This is in contrast to the hexagonal phase, where all three binary compounds are direct semiconductors. For the cubic alloys $Al_yGa_{1-y}N$, a direct to indirect energy gap transition is predicted for 0.52 [36] and 0.57 [37].

The optical and transport properties of semiconductors are primarily governed by the electronic band structures in the close vicinity of the valence band maximum and conduction band minimum. Thus, the **k·p** theory is not only an appropriate method to describe the electronic structures around the band extrema but also a convenient method to analyze the electronic structure of alloys and QW devices on the basis of the effective mass approximation. It further enables us to incorporate strain effects if the deformation potentials are known. In the analysis of conventional zincblende semiconductors, a parabolic conduction band is frequently assumed and the 4×4 and/or 6×6 Luttinger-Kohn Hamiltonians are used to describe the upper valence bands [38]. For the group III-nitrides, the spin-orbit splitting is very small and makes all three bands in the valence band closely situated in energy. Consequently, the three valence bands and the conduction band must be considered in unison, making the use of an 8×8 **k·p** Hamiltonian [39] (Kane model) imperative. Because the bandgaps of the cubic nitrides are very large, the coupling of the conduction to the valence bands is weak and can be treated as a second order perturbation. This allows the 8×8 **k·p** Hamiltonian to be split into a 6×6 **k·p** Hamiltonian for the valence bands (Luttinger-Kohn model) and a 2×2 **k·p** Hamiltonian dealing with the conduction band [34]. Formally, the Kane model transforms into the Luttinger-Kohn model if Kane's momentum matrix element P [39] between valence and conduction band states is taken to be zero. Recently, Pugh and colleagues [40] derived accurate 8×8 **k·p** parameters from semi-empirical band structure calculations. For zincblende structure, these parameters are the bandgaps at the Γ-point (E_{gap}), the quantity E_p, which contain Kane's momentum matrix element P between the conduction band and the valence band, the spin-orbit splitting Δ_{so}, the modified Luttinger parameters (γ_i'), and a conduction band dispersion parameter, s, which is correlated to the effective conduction band mass m_c^*. The modified Luttinger parameters γ_i' are related to the effective masses of the heavy hole m_{hh}^*, light hole m_{lh}^*, and spin split-off m_{so}^* valence bands and also to the more commonly used Luttinger parameters γ_i, which results if a 6×6 **k·p** Hamiltonian is used. In Enderlein and coworkers [41] the relationship between the different effective masses, the modified Luttinger parameters γ_i', and the Luttinger parameters γ_i is given in detail.

Table 9.1 summarizes the physical parameters of cubic AlN, GaN, and InN together with elastic properties as well as the deformation potentials. For nearly all of these parameters only theoretical estimations exist.

Table 9.1 Physical parameters of cubic GaN, AlN, and InN

Parameter	*AlN*	*GaN*	*InN*
Lattice constant (Å)			
a	4.38[a] (exp)	4.52[b] (exp)	4.98[c] (exp)
Energy parameters (eV)			
E_{gap}	6.02[d]	3.17[d]	2.18[d]
		3.302[e] (exp)	
E_{gap} (X)	4.92[d]	—	—
Δ_0	0.011[d]	0.011[d]	0.011[d]
		0.017[e] (exp)	
E_p	25.0[d]	25.4[d]	29.9[d]
	29.3[f]	24.6[f]	18.1[f]
Conduction band effective mass	0.19[d]	0.11[d]	0.10[d]
m_c^*/m_0		0.15–0.22[g] (exp)	
Valence band effective masses			
m_{hh}^*/m_0	1.20[d]	0.80[d]	0.84[d]
m_{lh}^*/m_0	0.33[d]	0.18[d]	0.16[d]
m_{so}^*/m_0	0.49[d]	0.26[d]	0.24[d]
Luttinger parameters[§]			
γ_1	1.924	3.571	5.332
γ_2	0.552	1.165	2.086
γ_3	0.882	1.575	2.446
Deformation potentials (eV)			
a_c	−6.8[h]	−2.77[i]	−3.3[h]
a_v	2.3[h]	3.63[j]	1.7[h]
B	−1.5[h]	−2.67[j]	−1.2[h]
D	−4.5[h]	−4.62[j]	−3.0[h]
Dielectric constant			
$\varepsilon(0)/\varepsilon_0$	8.5[k] (hex)	8.9[g]	15.3[k] (hex)
$\varepsilon(\infty)/\varepsilon_0$	4.68[k] (hex)	5.0[g]	8.4[k] (hex)
Elastic constants (GPa)			
c_{11}	304[i]	296[i]	184[i]
c_{12}	152[i]	154[i]	116[i]
c_{44}	199[i]	206[i]	177[i]
Bulk modulus B	203[i]	201[i]	139[i]
Piezoelectric constant (C/m^2)			
e_{14}	−0.526[j]	−1.110[j]	—

[§]Calculated from modified Luttinger parameters given by Pugh et al. [40] using Eq. (9.15) of the work of Enderlein et al. [41].
[a]Reference 42; [b]Reference 43; [c]Reference 44; [d]Reference 40; [e]Reference 45; [f]Reference 46; [g]Reference 47; [h]Reference 48; [i]Reference 49; [j]Reference 50; [k]Reference 51.

9.3 GROWTH OF CUBIC GaN

9.3.1 Selection of a Suitable Substrate

A common feature of reports of cubic material growth is the use of a substrate with cubic crystal structure. This is necessary because the thermodynamically stable crystal structure of GaN is the hexagonal phase, and therefore homoepitaxy on naturally deposited GaN is excluded. Unfortunately, no suitable lattice-matched substrate is available. Cubic GaN has been deposited on a number of cubic substrates, including GaAs (001) [7,9,52–57], Si (001) [58–60], 3C-SiC (ß-SiC) (001) [18,61–67], GaP [68,69], and MgO [70]. All these substrates share the handicap of a very large lattice-mismatch to the nitrides. Table 9.2 lists the lattice parameters, thermal expansion coefficients, and the calculated lattice-mismatches to *c*-GaN. Both GaAs and Si offer significant technological advantages due to the highly developed materials, a processing base already in place for their use, and their commercial availability. 3C-SiC, normally prepared by deposition on (100) Si, is the closest in lattice-match to the nitrides and thus should, in principle, produce the highest quality GaN. Unfortunately, industrial production of bulk 3C-SiC ceased a few years ago. For the realization of a vertically

Table 9.2 Lattice parameters, thermal expansion coefficient, lattice-mismatch to *c*-GaN, and thermal conductivity of prospective substrates for III-N epitaxial growth; lattice-mismatch, *f*, is calculated by $f = (a_{sub} - a_{\mathrm{GaN}})/a_{sub}$

Crystal	*References*	*Lattice constants a (nm)*	*Thermal expansion coefficient α (*$10^{-6} K^{-1}$)*	*Lattice-mismatch f*	*Thermal conductivity ($Wcm^{-1} K^{-1}$)*
c-GaN*	71	0.452	4.78	—	1.3
c-InN*	71	0.498	5.03	0.092	0.8
c-AlN*	71	0.438	4.56	−0.032	2.8
3C SiC	72	0.436	2.7	−0.037	4.9
Si	73	0.54301	3.59	0.168	1.5
GaAs	73	0.56533	6.0	0.20	0.5
GaP	2	0.54512	4.65	0.17	0.8
InP	73	0.5859	4.5	0.229	—
MgO	73	0.4216	10.5	−0.072	—
$MgAlO_2$	73	0.8083	7.45	—	—

*The linear expansion coefficient for cubic nitrides is not available. However, the lattice constant of cubic and hexagonal crystals are correlated by $a_{cubic} = (\sqrt{3} \cdot a_{hex}^2 \cdot c_{hex})^{1/3}$. The linear thermal expansion coefficient α_{cubic} is estimated from the hexagonal values for the a and c axis $\alpha_{a_{hex}}$ and $\alpha_{c_{hex}}$ by $\alpha_{cubic} \cong 1/3 \cdot (2\alpha_{a_{hex}} + \alpha_{c_{hex}})$. The hexagonal values $\alpha_{a_{hex}}$ and $\alpha_{c_{hex}}$ are taken from Pankove [71].

structured optoelectronic device such as an LED or a laserdiode (LD), one of the most important aspects for the selection of a suitable substrate is the ability of the substrate to be highly doped, both *n*-type and *p*-type. From this point of view, this restricts the substrates that can be used to GaAs, Si, and 3C-SiC.

The use of 3C-SiC substrate is prompted by the small lattice-mismatch to *c*-GaN (−0.037) and the high thermal conductivity of 3C-SiC ($4.9\,\mathrm{Wcm^{-1}K^{-1}}$). It was first proposed by Pankove [71] and was successfully used by Paisely and colleagues [62] for preparation of zincblende thin films. However, due to the difficulties in the fabrication of cubic SiC bulk material, nowadays thick (>3 μm) 3C-SiC epilayers grown on Si (001) substrates by plasma-enhanced chemical vapor deposition (PECVD) are currently used instead [63–65]. Although such thick high-quality 3C-SiC epilayers are available, a second independent epitaxy process is indispensable and shifts the problem of growing a largly lattice-mismatched epilayer to only the 3C-SiC growth. For high-power applications where the thermal conductivity is decisive, 3C-SiC will be the material of choice.

Growth of GaN on Si substrates offers a very attractive way to incorporate future GaN devices onto Si-based integrated circuits. However, due to the large differences in lattice constant (mismatch 0.17) and thermal expansion coefficient, it is rather difficult to directly grow GaN epitaxially on Si substrates. The formation of amorphous Si_xN_y inclusions at the interface, which act as nucleation centers for the formation of hexagonal GaN, hamper the epitaxial growth of phase-pure cubic epilayers [60]. Thin (<5 nm) 3C-SiC or GaAs are therefore necessary to prevent the formation of such Si_xN_y inclusions.

GaAs as a substrate for cubic GaN growth is motivated by the potential for fabrication of heterostructure devices. Easy cleavage of laser facettes and the integration of GaN devices to the well-developed GaAs technology makes this substrate very attractive, although the thermal stability at the high growth temperatures of about 700 °C may be problematic. As seen in Table 9.2, the estimated thermal expansion coefficient, α_{cubic}, of *c*-GaN is comparable to that of the GaAs substrate, reducing cracking and thermal strain effects. The lattice mismatch, *f*, of 20 percent is within the largest of the proposed substrates. For such large misfit systems, the assumption of elastic theory is no longer valid and a breakdown of epitaxial growth is expected, resulting in polycrystalline growth. However, recent results [7,9] showed that due to the occurence of a coincidental lattice-mismatch, $f_0 = (m \cdot a_{sub} - n \cdot a_{\mathrm{GaN}})/m \cdot a_{sub}$, the residual lattice-mismatch is drastically reduced and epitaxial growth is enabled. In the case of *c*-GaN grown on GaAs, the integers *m* and *n* are 4 and 5, respectively. Therefore, if $m = 5$, an additional lattice plan with a pure-edge dislocation at the interface is incorporated into GaN.

Transmission electron microscopy (TEM) measurements of the GaN/GaAs interface confirm this explanation. Thus, this heterosystem is close to true coincidence and an array of pure-edge dislocations with a period of 5 GaN lattice planes can account for the entire misfit. The residual lattice misfit, f_0, at growth temperature was estimated to be as low as 0.0002 ± 0.002.

9.3.2 Growth Methods

The various thin-film deposition methods employed in the growth of cubic GaN and other group III-nitrides have a number of advantages for addressing different issues in order to utilize the full potential of the cubic III-nitrides for optoelectronic as well as electronic devices. However, significant progress is needed for device applications in the areas of heteroepitaxial growth, crystal structure, impurity doping, reduction of extended defects as well as point defects, alloying phenomena, and the formation of homo- and heterojunction structures.

HVPE, which uses a chloride transport method, was developed in 1969 by Maruska and Tietjen [75] and is characterized by high growth rates. This may enable the growth of thick cubic GaN epilayers with significantly reduced misfit-related defects close to the surface and is useful as a substrate material for both MOCVD and MBE [76]. However, this technique was widely abandoned in the early 1980s because of apparent difficulties in reducing the native shallow-donor concentration to nondegenerated levels and thus enabling *p*-type doping.

Metalorganic vapor phase epitaxy (MOVPE) or MOCVD has been used used by Nichia, Inc., for the fabrication of hexagonal group III-nitride–based LEDs and LDs [77]. For commercial *h*-GaN device applications, MOCVD has emerged as the leading candidate owing to its large-scale manufacturing potential [78].

MBE has a number of advantages for the study of new materials and, in particular, for the study of epitaxial phenomena. The vacuum requirements for MBE are typically better than 10^{-10} mbar, which enables one to grow epitaxial films with high purity and excellent crystal quality at relatively low substrate temperature. Additionally, the ultrahigh-vacuum environment allows one to study in situ the surface, interface, and bulk properties of the growing films in real time by employing a variety of structural and analytical probes. Modern MBE deposition systems consist of multiple chambers separated by gate valves. Although the majority of surface analytical probes (auger electron spectroscopy (AES), secondary ion mass spectroscopy (SIMS), x-ray photoelectron spectroscopy (XPS), and ultra-violet photoelectron spectroscopy (UPS)) may be accomodated in the preparation chamber to avoid possible contamination by the evaporants, RHEED and quadruple mass spectrometry (QMS) are routinely used in

the growth chamber to monitor and control the growth process. Therefore, MBE was predestinated to study the growth of the metastable cubic group III-nitrides far away from thermodynamical equilibrium. It is generally recognized that MBE has played a major role in the development of high-quality cubic group III-nitrides. The MBE method of thin film deposition and its application to the growth of III-V compounds has been reviewed by a number of authors [79–82] and a more recent review of its application to the III-V nitrides is given by Moustakas [83].

9.3.2.1 HVPE

Only a few researchers have reported on growing cubic GaN films by HVPE to achieve thick films of improved structural quality [84,85]. The most popular choice for substrate has been GaAs (001) due to the potential of first depositing a homoepitaxial GaAs buffer layer to heal surface polishing damage and to form a wetted buffering surface nitridation layer by conversion with NH. It has been reported that low growth rates (<4 μm/hr) were required to suppress the introduction of hexagonal phases into the films [86,87]. The HVPE process is a chemical vapor deposition method, which is usally carried out in a hot wall reactor at atmospheric pressure. GaCl and NH_3 are used, with H_2 as a carrier gas. Three major problems concerning the growth of cubic GaN still exist. First, nucleation seems to be insufficient, resulting in a high amount of hexagonal inclusions. Second, even if *c*-GaN were grown on gas-source MBE cubic GaN-buffer layers (30 nm), the resulting phase purity is still only 85 percent under optimized growth conditions (substrate temperature 900 °C, V/III ratio 600, growth rate 1.6 μm/hr). The thickest cubic GaN layer to date is about 5 μm thick, which is still far from a thickness necessary to severely reduce the dislocation density, as is needed for a substrate for homoepitaxy. At increasing layer thickness, the hexagonal content as well as the surface roughness dramatically increased. Finally, as reported by Tsuchiya and co-authors [86] the grown epilayer additionally have a residual high *n*-type concentration of about 1×10^{20} cm^{-3} and free electron mobilities of about 50 cm^2/Vs, which are comparable to that of *h*-GaN. To date, the only cubic group III-nitride deposited by HVPE is cubic GaN. Therefore, further work is required to develop improved material suitable for device applications or as a substrate with low structural defect density.

9.3.2.2 MOCVD

MOCVD was suggested for growth of III-V semiconductors 30 years ago [88], and matured for applications in the AlGaAs/GaAs and In- and P-related III-V systems during the 1980s. The first application to grow hexagonal III-nitride growth was reported over a decade ago [89]. Currently, it is the most popular method to grow multilayer device structures of *h*-III-nitrides and is the only technique used for commercial III-nitride device production.

For cubic group III-nitrides, however, this technique has only recently been successfully used for growth [90,91]. The precursers used for III-nitride growth are trimethyl-gallium (TMG) or triethyl-gallium (TEG), trimethyl-aluminium (TMA), and trimethyl-indium (TMI) for the group III elements, and ammonia (NH_3) or 1,1-dimethylhydrazine (DMHy) for nitrogen. The carrier gases are typically either hydrogen, nitrogen, or a mixture of both. In most cases, GaAs-substrates are used [90–92], however, 3C-SiC [93] is also reported as a substrate. Typical growth temperatures for *c*-GaN and *c*-$Al_yGa_{1-y}N$ ($y < 0.3$) are between 900 °C and 950 °C and for $In_xGa_{1-x}N$ between 700 °C and 770 °C [94]. Growth rates of *c*-GaN are in the order of about 240 nm/hr [95].

Doping in MOCVD is done in situ from the gas phase. For *n*-type doping by Si, silane (SiH_4) is used as precurser. In this way, free electron concentrations up to 10^{20} cm^{-3} are conveniently reached at room temperature in *h*-GaN. Mg is the most suitable *p*-type dopant and can be introduced via the precurser bis-cyclopentadientyl (Cp_2Mg) up to concentration of a few 10^{19} cm^{-3}. However, for activating the acceptors a postgrowth heat treatment, either by low-energy electron beam irradiation (LEEBI) [96] or in N_2-atmosphere at temperatures at about 700 °C, are necessary [97]. Although up to now no detailed study on either *p*-type or *n*-type doping of cubic group III-nitrides by MOCVD has been reported, Tanaka and colleagues reported on the first cubic GaN *p*-*n* homojunction [98]. For further details and information on the growth of cubic III-nitrides by MOCVD, see the chapter of J. Wu in this text [99].

9.3.2.3 MBE

MBE is a physical method of thin-film deposition process in which thermal beams of atoms or molecules react on the clean surface of a single-crystalline substrate that is held at high temperatures under ultrahigh vacuum conditions to form an epitaxial film. The most common way to create a molecular beam for MBE growth is through the use of Knudsen effusion cells. The crucibles employed in Knudson cells are mainly made of pyrolytic boron nitride (PBN), which contains both the elemental group III atoms (Al, Ga, In) as well as the dopants (Si, Mg). The temperature of the different crucibles must be independently controlled to within ±1 °C.

Deposition of GaN and group III-nitrides by MBE requires the development of appropriate nitrogen sources, because molecular nitrogen (N_2) does not chemisorb on Ga due to its large binding energy of 9.5 eV. To solve this problem, different approaches currently are reported for the growth of cubic and hexagonal group III-nitrides. The first approach is the use of gaseous sources such as NH_3 or 1,l-dimethylhydrazine (DMHy); this kind of MBE is also called chemical beam epitaxy (CBE) or reactive-ion molecular beam epitaxy (RMBE). In fact, the use of NH_3, which dissociates at the growth

front in a surface catalytic process, has recently become fashionable after it was shown that high-quality layers could be obtained with this method [99,100]. However, this compound is quite thermally stable and, as a result, significantly limits the growth temperature. Therefore, lower growth temperatures, such as those needed for low-temperature nucleation buffers or for layers containing In, cannot be grown as easily with NH_3 [101]. DMHy has higher reactivity than NH_3 and is expected to produce better quality crystals [54]. If additionally, metalorganic precursors are used for group III sources, the method is also called metalorganic MBE (MOMBE). MOMBE is still in the early stage of development [102,103].

The second approach utilizes plasma-activated molecular nitrogen via DC-plasma sources, microwave plasma-assisted electron cyclotron resonance (ECR) plasma sources, or radiofrequency (RF) plasma sources. DC-plasma assisted MBE was successfully applied for the growth of cubic GaN [104]. However, due to the low growth rate of 10 to 30 nm/hr, imposed by the limited nitrogen flux of the DC-source, the synthesis of a 1-μm-thick film would require approximately 50 hr, making it almost impossible to achieve stable growth conditions throughout such a run. In addition, with increasing layer thickness, the surface morphology became rougher and due to the formation of {111} facets that serve as nucleation sites for the hexagonal phase, phase purity worsened.

Compact MBE-compatible ECR sources are commercially available. ECR sources rely on coupling of microwave energy at 2.45 GHz with the resonance frequency of electrons in a static magnetic field. Such coupling allows for ignition of the plasma at low pressures and powers, and produces a high concentration of radicals. In an ECR source, approximately 10 percent of the molecular nitrogen is converted into atomic nitrogen. Because these sources operate very efficiently at fairly low powers, they are usually cooled only by air. A typical growth rate of an ECR source is about 200 nm/hr but it can be raised up to 1 μm/hr if exit apertures with a large number of holes are used [83]. A detailed description of the design and principle of operation of microwave plasma-assisted ECR-sources is given by Moustakas [83].

RF plasma sources are among the most common sources in MBE growth of III-V materials. Nitrogen plasmas are generated by inductively coupling RF energy at a frequency of 13.56 MHz into a discharge chamber filled with nitrogen to pressures of $>10^{-6}$ mbar. The discharge tube and the beam exit plate can be fabricated from pyrolytic boron nitride (PBN), avoiding quartz, which may be a source of residual Si or O doping of GaN. The plasma sheath effect confines ions and electrons within the plasma discharge regions, allowing only low-energy (<10 eV) neutral species to escape. Therefore, these sources are believed to produce significant concentration of atomic nitrogen. Due to the very high powers used in these sources, up to 600 W, the plasma chambers usually must be water-cooled.

RF sources permit growth rates up to about 1 μm/hr and are available from a number of vendors.

The different species of N produced by the various kinds of plasma discharge may also have a profound impact on the growth kinetics, depending on whether the impinging species is an ionized molecule (N_2^+) or atomic N in an excited state (N*). In a recent study by Myers and co-authors [105] using a quadrupole mass spectrometer, two different RF plasma sources (Oxford Applied Research CARS-25 and EPI Vacuum Products Unibulb) were compared. These sources typically produce a complex mixture of active nitrogen superimposed on a background of presumed inert molecular nitrogen. Whereas the Oxford source produced primarily atomic nitrogen with little indication of the presence of molecular metastables, the EPI source produced significantly less atomic nitrogen but, a significant flux of molecular nitrogen metastables. As noted out by Newman [106], different compositions of the plasma are relevant for different mechanisms, which can participate both in the growth and in the decomposition of GaN. Ionic and neutral atomic nitrogen can take part in growth and decomposition, which is different from the molecular nitrogen metastables, for which neglectable competition to growth occur. This may explain the relatively low growth rates obtained with atomic nitrogen sources. In addition, both atomic and metastable molecular nitrogen contain significantly more energy than required for GaN formation. Incorporation of atomic nitrogen releases this energy into the lattice where it can drive unfavorable reactions. In contrast, the excited molecule can incorporate one atom into the growing GaN, whereas the other desorbs, carrying away the excess energy. Therefore, the selection of the plasma source influences the growth rate, surface morphology, and optical and electrical properties of the resulting epilayer. The detailed influence of the different active nitrogen species, however, is not yet clear and requires further study for both hexagonal as well as cubic group III-nitrides.

9.3.3 Plasma-Assisted MBE

Single phase cubic GaN epilayers were grown on GaAs (001) substrates by plasma-assisted MBE using a Riber-32 system equipped with elemental sources of Ga, In, Al, As, Mg, and Si [9]. The deposition system is schematically illustrated in Figure 9.3. For the N source, an Oxford Applied Research CARS 25 RF-activated plasma source was used. The N_2-background pressure in the growth chamber was between 2×10^{-6} mbar and 5×10^{-5} mbar. Before starting the *c*-GaN nucleation, a GaAs buffer layer was first grown at 600 °C under (2 × 4) reconstruction to ensure As-stabilized conditions. The nucleation of *c*-GaN was initiated at the same substrate temperature using an N/Ga flux ratio of about 4. After deposition of 10 to 20 monolayers (MLs),

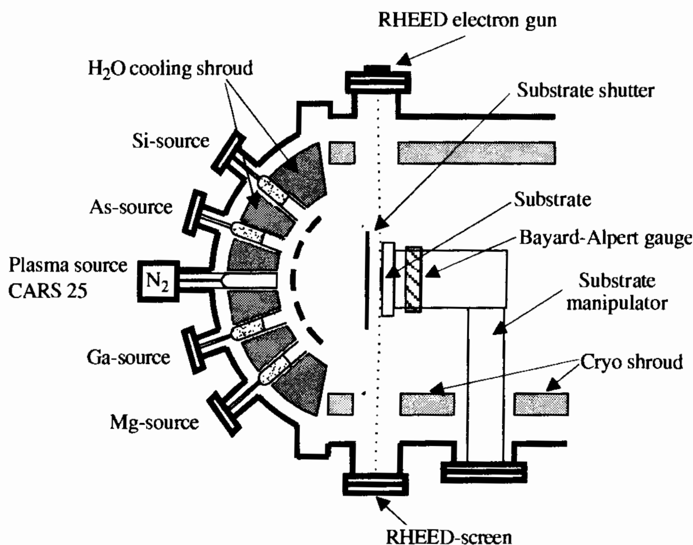

Figure 9.3 Schematic diagram of the MBE apparatus (Riber 32).

the nucleation stage was stopped and the substrate temperature was subsequently raised to 680 °C to 740 °C. The static GaN (001) surface exhibits a clear (2 × 2) reconstruction during this period. The growth was continued at the higher temperature level, varying the N/Ga flux ratio and the substrate temperature. The growth process was monitored continuously by RHEED and an RHEED image recording system.

The reconstruction of the growing surface is controlled primarily by surface stoichiometry. Figure 9.4 depicts the surface reconstruction diagram of *c*-GaN measured during growth. The V/III flux ratio is plotted versus growth temperature. In this ratio, the flux rate of atomic N is related to the Ga flux rate. We have found by mass-spectroscopic measurements that the effective flow of atomic N arriving on the surface amounts to 1 percent to 7 percent of the N_2-beam-equivalent-pressure, which is primarily dependent on the total flow rate and the RF power applied. In addition to static (2 × 2) reconstruction, we have observed *c* (2 × 2) and (2 × 2) reconstructions as well as an unreconstructed (1 × 1) surface during the growth, in agreement with other published results [54,104]. At high excess of N, the unreconstructed (1 × 1) surface is stable. Under Ga-stabilized conditions, a *c* (2 × 2) reconstruction appears; layers grown here show *n*-type conductivity in Hall effect measurements [107]. The (2 × 2) reconstruction is associated with N-stabilized conditions giving rise to *p*-type behavior. In a narrow range between the *c* (2 × 2) and (2 × 2) regime, both reconstructions occur simultaneously with different intensities of the reconstruction lines,

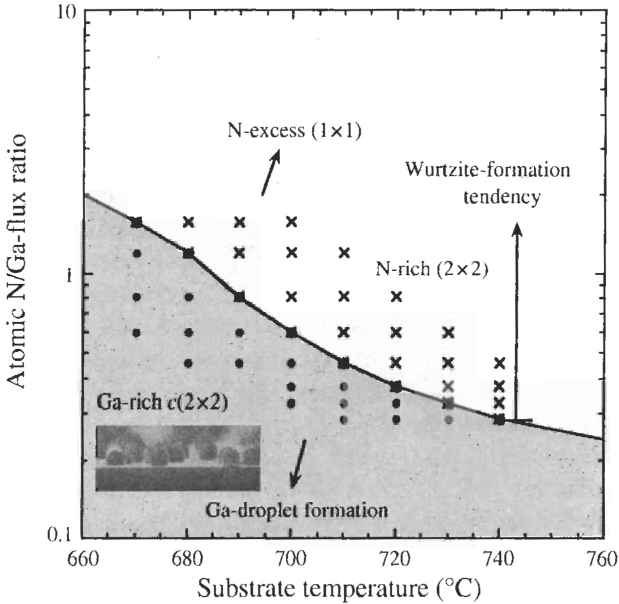

Figure 9.4 Surface reconstruction of cubic GaN (001) as a function of growth temperature and N/Ga flux ratio. The dots represent the stability range of the Ga-rich c (2 × 2) reconstruction, the crosses show the stability range of the N-rich (2 × 2) reconstruction. A superposition of both reconstructions occurs in a narrow range in between, indicating near-stoichiometric compositions.

indicating a nearly stoichiometric adatom coverage. At temperatures lower than 680 °C, this requires an N/Ga flux ratio larger than 1. For substrate temperatures higher than 700 °C, Ga re-evaporation becomes significant. The Ga loss from the surface must be compensated to stabilize stoichiometric conditions. Therefore, the N/Ga ratio decreases. Assuming that the Ga desorption is the dominant kinetic process limiting the growth rate, we have calculated the respective activation energy. From the slope of the stoichiometric line, we find a desorption energy $E_{Ga} = 2.11\,\text{eV} \pm 0.2\,\text{eV}$ by an Arrhenius plot. This is much lower than the value of 3.2 eV estimated from Gas-Source MBE data [108], and nearly comparable to 2.45 eV reported by Brandt and co-authors [109].

Under optimum flux-ratio conditions of about 0.30 and a substrate temperature of 740 °C , RHEED oscillations at the specular spot position in the [−110] azimuth can be clearly seen (Figure 9.5). With these growth conditions, the tendency to form mixed phases is suppressed and the growth becomes increasingly two-dimensional due to the enhanced surface mobility of the Ga adatoms. The oscillations shown in Figure 9.5 appear after growth interruption and opening of the Ga-cell shutter. The steep initial rise

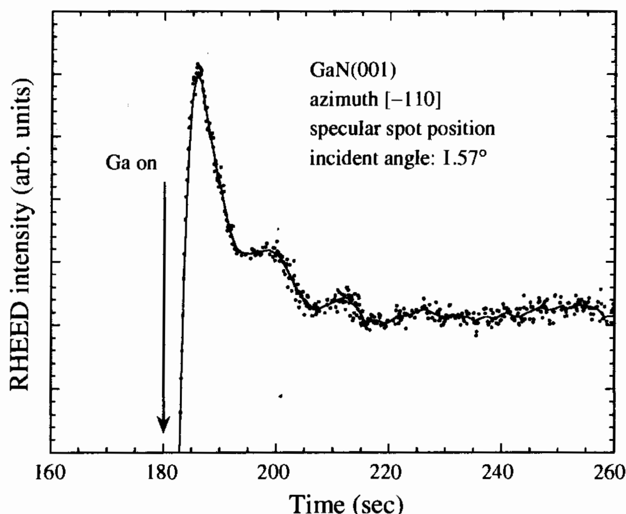

Figure 9.5 RHEED oscillations of cubic GaN (001) detected at the specular spot position in the [−110] azimuth. The angle of incidence of about 1.57° indicates an out-of-phase condition.

of the specular spot intensity suggests that the growth onset is accompanied by an effective surface smoothing. The oscillations are rapidly damped and entirely disappear when the specular beam intensity is recovered to its steady-state level. A growth rate of about 0.08 ML/sec is deduced from the oscillation period. This value is in excellent agreement with the growth rate derived from the total thickness of the layers measured by optical interference spectroscopy.

Due to the metastability of the cubic phase of GaN, the structural perfection of epitaxial layers of this material is extremely sensitive to the growth parameters. It has been found that only slight deviations from the ideal stoichiometric growth conditions can influence the structural [110], optical [10], and type of conductivity [107] of undoped *c*-GaN. Ga-excess at the surface favors the formation of Ga-droplets and μm-size crystalline inclusions [111], which are detrimental to the epilayer surface morphology. In addition, in Ga-rich conditions, different types of surface irregularities are observed as a result of successive melt-back etching in GaN and GaAs and solution growth within Ga-droplets due to the change of the saturation conditions of the liquid Ga-phase on the surface of the growing film [112]. On the other hand, N-rich conditions seem to enhance the probability of the formation of inclusions with hexagonal crystalline structure [9,104]. For these reasons, it is necessary to control the growth parameters during *c*-GaN MBE extremely accurately. To do so, a method which allows an accurate determination of the transition between the $c\ (2 \times 2)$ and the (2×2) surface reconstruction of

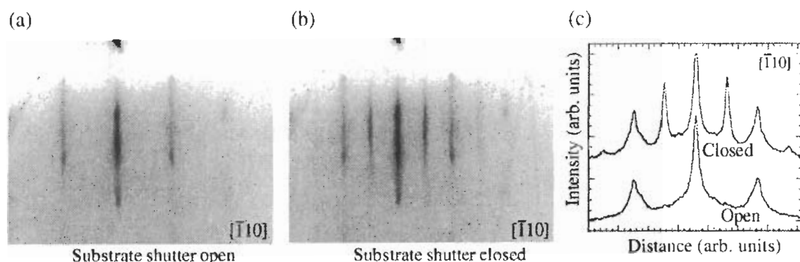

Figure 9.6 RHEED-pattern of the [−110] azimuth of a cubic GaN (001) surface under slightly Ga-rich growth conditions. (a) is taken at dynamic conditions (substrate shutter open) (b) is taken at static conditions (substrate shutter closed), (c) is linescans of both images taken at the same position.

c-GaN was developed [113]. The phase boundary, which is measured with high accuracy, is then used as a reference point to establish slightly Ga- or N-excess growth conditions. This method takes advantage of the fact that the transition between the *c* (2 × 2) and (2 × 2) surface reconstruction can be monitored by the RHEED intensity of the half-order reconstruction I_{HOS} measured along the [−110] azimuth [114].

Figure 9.6 shows the RHEED patterns of the [−110] azimuth of a *c*-GaN (001) surface under slightly Ga-rich growth conditions at dynamic (left, substrate shutter open) and static (right, substrate shutter closed) conditions. Linescans, which were taken at the same position of the RHEED-patterns are shown on the right side. One clearly sees the appearance of the half-order streak under the closed condition. In Figure 9.7 the temporal behavior of the intensity of the half-order streak I_{HOS} measured for a substrate shutter open-close sequence is indicated. I_{HOS} is zero for the *c* (2 × 2) and maximum for (2×2) surface reconstruction. Therefore, the intensity of the half-order streak is indicative for that fraction of the surface that is (2 × 2) reconstructed. It has been suggested that the Ga-coverage of a *c* (2 × 2) reconstructed surface exceeds that of a (2 × 2) reconstructed surface [114] and I_{HOS} can be related to the Ga-coverage of the growing *c*-GaN epilayer during growth. The salient feature of the curve is, however, that the increase of I_{HOS} after closing the substrate shutter is delayed by a time, t_d, indicating that during this time, the Ga-coverage of the surface exceeds that for *c* (2 × 2). Because the Ga-flux onto the surface is zero when the substrate shutter is closed, the existence of a delay time indicates that during t_d, a "reservoir" of excess Ga at the surface is emptied, thus keeping the Ga-coverage high. As can also be seen in Figure 9.7, t_d measured after a growth period (shutter open) of 4 min. is equal to twice the value of t_d obtained after 2 min. growth. This supports the assumption that t_d reflects the desorption of excess (physisorbed) Ga which is accumulated at the surface during growth. Figure 9.8 shows t_d as

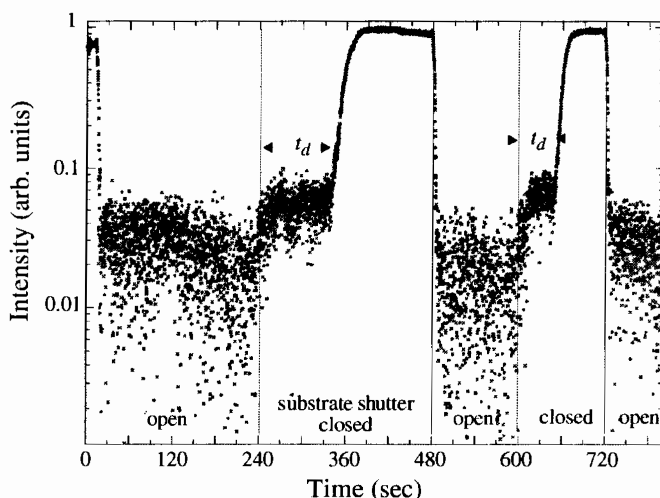

Figure 9.7 RHEED-intensity of the half-order streak in the [−110] azimuth of a cubic GaN (001) surface. Growth interruption and restart of the growth are initiated by closing and opening of the substrate shutter.

a function of the Ga-flux and a constant N-flux, clearly revealing the linear dependence between t_d (excess Ga at the surface) and the Ga-flux. It has been well-established that excess Ga leads to the formation of micrometer-sized crystals within Ga-dropets on the surface of *c*-GaN [112]. Growth conditions which give a minimum of excess Ga at the surface are therefore absolutely necessary for the growth of homogeneous, defect-free *c*-GaN layers. On the other hand, because a deficit of Ga favors the formation of hexagonal

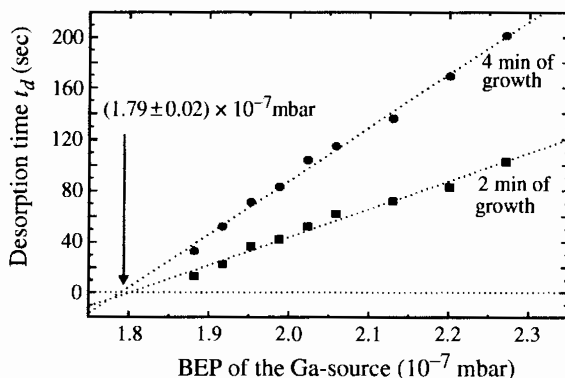

Figure 9.8 Desorption time, t_d, measured as a function of the Ga-flux (beam equivalent pressure, BEP) with a constant N-flux and a constant substrate temperature of $T_S = 720\,°\mathrm{C}$.

inclusions, the most desirable growth conditions are characterized by $t_d = 0$. In the example shown in Figure 9.8, this is given by a Ga-flux equal to $(1.79 \pm 0.02) \times 10^{-7}$ mbar. The optimum growth conditions are therefore found by performing a few sequences of RHEED measurements at slightly different Ga-flux and then extrapolating to $t_d = 0$. The delay time, t_d, also depends on the substrate temperature, T_S. At constant Ga- and N-flux, t_d is proportional to the square root of the substrate temperature, indicating that the desorption of excess Ga from the surface can be well-described by the Langmuir equation.

In order to show the effectiveness of this method, three c-GaN layers with three different sets of growth conditions equivalent to $t_d = 2$ sec, $t_d = 5$ sec, and $t_d = 10$ sec after 2 min. of growth were prepared. The total growth time was the same for all samples, resulting in a layer thickness of about 800 nm. Micrographs of these c-GaN layers reveal a dramatic reduction by a factor of nearly 100 of the droplet density with decreasing t_d (see Figure 9.9a). Plotting the droplet density versus the square of the desorption time, t_d,

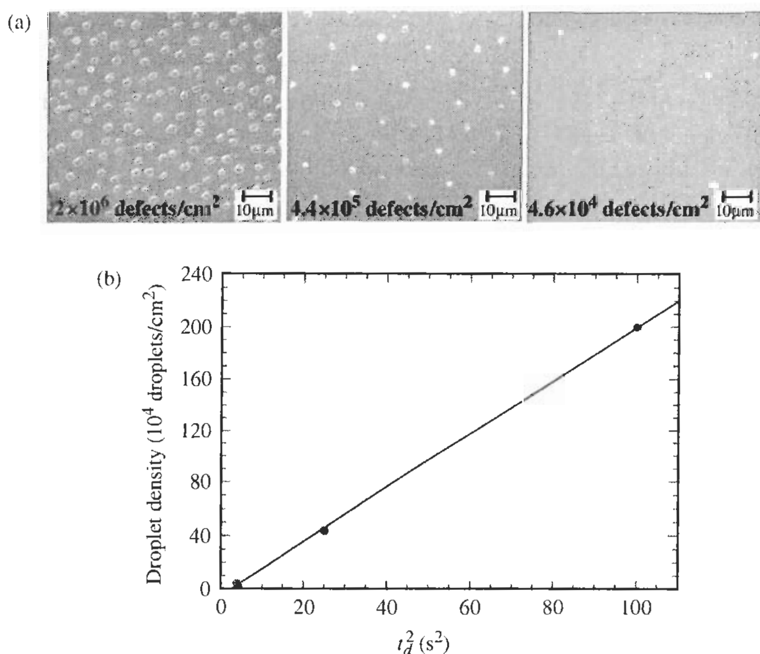

Figure 9.9 (a) Droplet density of 800-nm-thick c-GaN layers grown under different growth conditions. The layers were grown with desorption times of $t_d = 10$ sec, $t_d = 5$ sec, $t_d = 2$ sec (from left to right) corresponding to droplet densities of 2×10^6 defects/cm^2, 4.4×10^5 defects/cm^2, and 4.6×10^4 defects/cm^2, respectively; (b) droplet density as a function of the square of the desorption time, t_d.

results in a nice linear relationship, as shown in Figure 9.9b. This method therefore allows one to establish growth conditions which lead to epilayers that are nearly free of microcrystals. It also emphasizes the importance of the careful control of the growth conditions in situ by RHEED to establish optimal growth conditions just at the c (2×2) to (2×2) surface phase transition.

9.4 CHARACTERIZATION OF NOMINALLY UNDOPED CUBIC GaN

9.4.1 Phase Purity

The metastable nature of c-GaN is a major difficulty for the growth of single-phase layers. It is therefore important to clearly distinguish between the cubic and the hexagonal phase when differently grown layers are compared.

The most common method used to analyze structural properties of epitaxial films is high-resolution x-ray scattering. However, standard diffractometer $\omega - 2\Theta$ scans are unable to detect hexagonal subdomains, because their c-axis may be tilted with respect to the cubic main axis [104,115]. Therefore, so-called reciprocal space maps have been used to measure hexagonal phase inclusions in c-GaN epilayers [104]. Layers grown under N-excess showed, in addition to the cubic (002) reflex, a pronounced diffraction peak which was attributed to a (10–11) reflection from hexagonal grains with the [001] axis parallel to the [111] axis of the cubic phase. This result is in good agreement with the interpretation of RHEED patterns from c-GaN grown under N-rich conditions [9]. However, the x-ray intensity scattered by hexagonal grains is small. Therefore, a high intensity of the primary x-ray beam and relatively long measuring times are required to detect the hexagonal grains. For c-GaN epilayers on GaAs substrates, a phase purity of better than 99.9 percent has been obtained.

Raman scattering is a second, very sensitive and straightforward tool for the quantitative determination of a structural minority phase in GaN [110]. Although the electronic structures of the cubic and hexagonal modification of GaN are quite similar, their lattice vibrations are expected to be different. The wurtzite structure of GaN arises from the zincblende structure by first compressing the crystal along the [111]-axis, which becomes the c-axis of the hexagonal phase and, second, by changing the stacking of layers along this axis, resulting in a doubling of the number of atoms in a primitive unit cell. The compression splits the T_2-mode of the cubic phase into A_1 and E_1 modes of the hexagonal phase. Because the hexagonal distortion is small, this splitting is also expected to be small. The doubling of the number of atoms in the primitive cell results in six additional degrees of freedom for the relative motions, giving rise to two B_1 and two E_2 modes [116]. Because the

selection rules are different for the cubic and hexagonal phase of the materials, Raman scattering can unambiguously distinguish between both phases. By comparing the intensity ratio of the allowed cubic and hexagonal modes and by taking into account the relative Raman-coefficients [117], a quantitative estimation of the hexagonal phase content is possible. A presumption for this method is, however, that the epilayers are epitaxially grown on the substrates. This can be proved by measuring the polarization dependent of the phonon modes of the *c*-GaN epilayer and of the underlaying GaAs substrate. In our *c*-GaN epilayers, the *c*-GaN mode showed the same polarization dependence as the GaAs modes, verifying that *c*-GaN grows epitaxially on the cubic GaAs substrate. From signal-to-noise ratio considerations, the detection limit has been estimated to be about 1 percent and this enables us to verify the phase purity of our cubic GaN samples down to the 1 percent level [110].

Due to the smaller bandgap of *c*-GaN compared with *h*-GaN (by about 0.2 eV), a first hint of the phase purity of the *c*-GaN can also be obtained from PL measurements at low temperatures. All signals above the bandgap of cubic GaN (3.305 eV) may result from the hexagonal phase. However, a quantitative estimation of the hexagonal phase is difficult due to the involvement of unknown recombination processes, which influence the relative intensities from the two phases. In addition, due to the smaller bandgap, free carriers generated in the hexagonal may diffuse into the cubic phase material and recombine therein. In the best phase-pure cubic GaN epilayers, the luminescence in the range between 3.3 and 3.5 eV is suppressed by more than three orders of magnitude, compared with the near bandgap luminescence of the cubic phase. By selectively exciting the luminescence with a photon energy just between the two different bandgaps, the GaN phase from which the luminescence originates can be estimated.

9.4.2 Structural Properties

9.4.2.1 TEM measurements

The defect structure of cubic GaN on GaAs substrate has been studied in detail by high-resolution transmission electron microscopy (HRTEM) [118]. It has been shown that the nucleation occurs by the formation of nano-scale three-dimensional islands, which have a well-defined epitaxial relationship. Even in the smallest island of about 10 nm^3, the strain is relaxed by inserting misfit dislocations. Misfit dislocation cores are detected at a distance of every fifth {111} GaN lattice plane. These results directly demonstrate that pure-edge–type misfit-dislocations are instantaneously formed during the nucleation process and an extra {110} lattice plane is incorporated into the edge of the growing island without any climb or glide mechanism [119]. The classical theories of misfit dislocation formation thus cannot be applied

to this case [120]. The results can be explained by a coincidence or are also called "magic mismatch" between the epilayer lattice constant, a_{GaN}, and the substrate lattice constant, a_{GaAs}. A true coincidence would occur if the ratio of the lattice constants, a_{GaN}/a_{GaAs}, equals a ratio m/n, where m and n are integers. If $m = n \pm 1$, one additional lattice plane, that is, a simple edge dislocation, is inserted in each unit cell of the coincidence lattice. In general, however, a deviation from true coincidence is expected and a new residual coincidence-lattice-mismatch $f_0 = (ma_{GaN} - na_{GaAs})/ma_{GaAs}$ can be defined. Taking the most accurate values for the lattice constants at growth temperature, $a_{GaN} = 0.455 \pm 0.01$ nm and $a_{GaAs} = 0.568 \pm 886$ nm, a value of $f_0 = -(0.0002 \pm 0.0020)$ is obtain by taking $m/n = 4/5$. The introduction of an array of edge dislocations with a period of 5 GaN lattice planes is therefore sufficient to relieve nearly the entire misfit strain of 20 percent and explains the phenomenon of heteroepitaxy on substates with such a high lattice-mismatch. The residual deviation introduces elastic strain at the interface in addition to the strain accomodated by the misfit dislocations.

For the subsequent growth, the coalescence of the individual nuclei may be responsible for the generation of secondary defects in the layers, as seen with TEM (Figure 9.10). Whereas in isolated individual nuclei no planar defects could be measured, the most prevalent structural defects observed in thick cubic GaN epilayers are stacking faults and micro-twins. Because the distance of the individual nuclei may not necessarily be in phase with respect to their dislocation array, coalescence of individual nuclei may break its periodicity and may create locations with very high local strain. These local strain concentrations are believed to be the reason for the generation

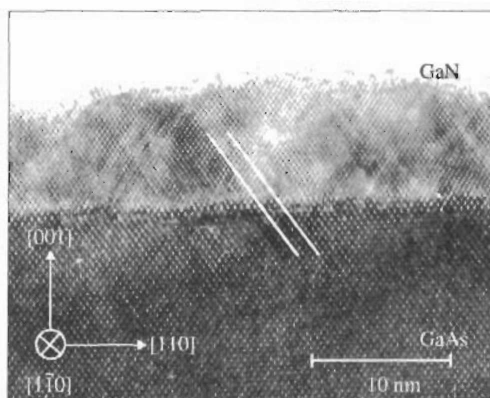

Figure 9.10 TEM image of a cubic GaN/GaAs (001) interface. Within the white lines along {111} planes one can clearly count that five planes in the GaN correspond to four lattice planes in the GaAs.

of the observed stacking faults and micro-twins, which are able to fit the coincidence lattice in the region of coalesced islands [119]. Figure 9.10 shows a cross-section TEM image of one of our cubic GaN/GaAs (001) heterostructures taken along ⟨1–10⟩ direction. The interface is flat on an atomic scale, with an overall vertical roughness of a few monolayers. A regular arrangement of pure-edge dislocations appear at the interface, and by carefully looking between the two white lines along {111} planes one can clearly count that five planes in the GaN correspond to four lattice planes in the GaAs. The periodicy is broken just at those locations from which stacking faults originate. The density of these planar defects has its highest value near the interface. At a distance of about 40 nm from the interface, a reduction in dislocation density by about one order of magnitude is observed [121] and the remaining planar defects are frequently arranged in groups extending through the whole epilayer. Some of these stacking faults mutually terminate when intersecting. The *c*-GaN films have a mosaic nature and retrain the epitaxial relationship to the substrate throughout its thickness.

Ruvimov and co-authors [122] reported that an exposure of the layer surface to As flux during the growth of the first few monolayers resulted in a remarkably flat GaN/GaAs interface with a typical interface roughness of only three to four monolayers.

In the case of thick 3C-SiC substrate, which has a lower misfit of only −3.7 percent, the lattice discontinuity is observed every 30 to 40 atomic layers. Therefore, the defect density at the interface is much smaller than that of the GaN/GaAs interface [54].

9.4.2.2 X-ray measurements

High-resolution x-ray diffraction (HRXRD) allows to measure the density of extended defects in epitaxial layers. The full-width at half maximum (FWHM) of the Bragg reflex measured in a direction perpendicular to the diffraction vector (ω-scan) is related to the intensity of extended defects in the layer. The ω-scan measures the intensity spread for the coordinate $q_\perp$ in reciprocal space arising from both mosaicity and finite lateral domain size. Figure 9.11 compiles HRXRD data from *c*-GaN layers with a varying thickness grown by MBE on GaAs [123,124] and 3C-SiC [54] substrates, respectively. A clear decrease of FWHM with increasing layer thickness is seen and the values given by Yang and colleagues [124] are quite comparable to our data. The linewidths measured for *c*-GaN grown on 3C-SiC substrates are approximately a factor of three narrower than that for layers grown on GaAs substrates. This may be expected due to the lower lattice-mismatch of this system. The clear trend of decreasing FWHM with increasing layer thickness inmediately implies that the number of extended defects is reduced in thicker epilayers.

of the observed stacking faults and micro-twins, which are able to fit the coincidence lattice in the region of coalesced islands [119]. Figure 9.10 shows a cross-section TEM image of one of our cubic GaN/GaAs (001) heterostructures taken along ⟨1–10⟩ direction. The interface is flat on an atomic scale, with an overall vertical roughness of a few monolayers. A regular arrangement of pure-edge dislocations appear at the interface, and by carefully looking between the two white lines along {111} planes one can clearly count that five planes in the GaN correspond to four lattice planes in the GaAs. The periodicy is broken just at those locations from which stacking faults originate. The density of these planar defects has its highest value near the interface. At a distance of about 40 nm from the interface, a reduction in dislocation density by about one order of magnitude is observed [121] and the remaining planar defects are frequently arranged in groups extending through the whole epilayer. Some of these stacking faults mutually terminate when intersecting. The *c*-GaN films have a mosaic nature and retrain the epitaxial relationship to the substrate throughout its thickness.

Ruvimov and co-authors [122] reported that an exposure of the layer surface to As flux during the growth of the first few monolayers resulted in a remarkably flat GaN/GaAs interface with a typical interface roughness of only three to four monolayers.

In the case of thick 3C-SiC substrate, which has a lower misfit of only −3.7 percent, the lattice discontinuity is observed every 30 to 40 atomic layers. Therefore, the defect density at the interface is much smaller than that of the GaN/GaAs interface [54].

9.4.2.2 X-ray measurements

High-resolution x-ray diffraction (HRXRD) allows to measure the density of extended defects in epitaxial layers. The full-width at half maximum (FWHM) of the Bragg reflex measured in a direction perpendicular to the diffraction vector (ω-scan) is related to the intensity of extended defects in the layer. The ω-scan measures the intensity spread for the coordinate $q_{\perp}$ in reciprocal space arising from both mosaicity and finite lateral domain size. Figure 9.11 compiles HRXRD data from *c*-GaN layers with a varying thickness grown by MBE on GaAs [123,124] and 3C-SiC [54] substrates, respectively. A clear decrease of FWHM with increasing layer thickness is seen and the values given by Yang and colleagues [124] are quite comparable to our data. The linewidths measured for *c*-GaN grown on 3C-SiC substrates are approximately a factor of three narrower than that for layers grown on GaAs substrates. This may be expected due to the lower lattice-mismatch of this system. The clear trend of decreasing FWHM with increasing layer thickness inmediately implies that the number of extended defects is reduced in thicker epilayers.

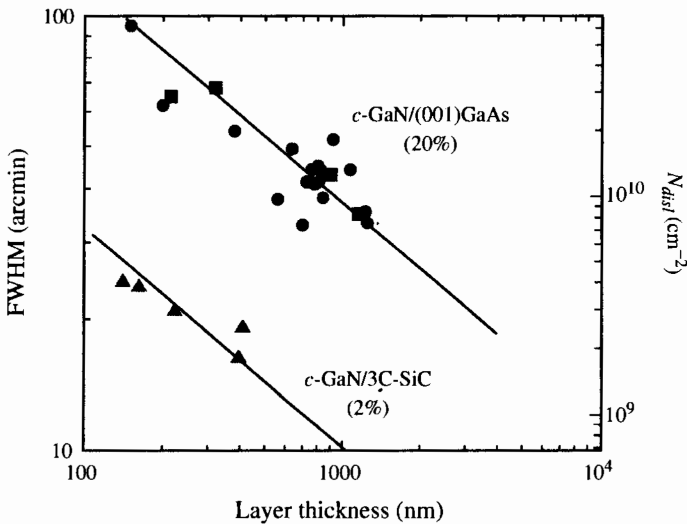

Figure 9.11 FWHM of high-resolution x-ray diffraction rocking curves (ω-scan) from *c*-GaN layers with varying thickness grown by MBE on GaAs (001) (full circles are my own data, full squares are data from Yang et al. [124]) and 3C-SiC (data from Okumura et al. [54]). The lines represent the trends using the dislocation glide model by Ayers [125].

For the 3C-SiC case, where the lattice-mismatch is only −3.7 percent, the dislocation glide model by Ayers [125] can be used to calculated the dislocation density, N_{disl}, as a function of layer thickness. This model predicted the 1/thickness dependence of the dislocation densities and also achieves an order of magnitude accuracy in quantiative predictions of the dislocation densities for a number of heteroepitaxial systems. The full line through the 3C-SiC data shows this model calculation, which gives a relation between the dislocation density, N_{disl}, the lattice-misfit between substrate and epitaxial layer and the thickness of the epilayer. In the calculation it was assumed that 60° dislocations with a Burgers vector of 0.32 nm are the predominant defects in the layers. The trend of the calculated curve is in excellent agreement with the values measured by Okumura and colleagues [54]. The estimated dislocation density, N_{disl}, is shown on the right-hand scale of the diagram. Unfortunately, this model cannot be applied to heteroepitaxial systems with mismatch greater than about 10 percent because in such systems the misfit dislocations are so closely spaced that the continuum elasticity theory cannot predict their line tension with acceptable accuracy. However, if we shift the calculated line upward, one sees that for the *c*-GaN/GaAs case, the same trend is observed (full line through our data). Therefore, we think that the same defect annihilation process is also true in the GaAs case. From the right-hand scale we estimated a dislocation density of about

10^{10} cm^{-2} for a 1-μm-thick *c*-GaN epilayer on GaAs (001). The HRXRD data are in good agreement with TEM investigations [124] which yield a defect density in the order of 10^9 to 10^{11} cm^{-2}. In addition, TEM measurements further showed that the density of stacking faults drastically decreases with increasing layer thickness.

9.4.2.3 Rutherford backscattering

Rutherford backscattering (RBS), dechanneling, and angular scan measurements have been performed to study the crystalline perfection, the type of defects responsible for dechanneling and to estimate the defect densities in cubic group III-nitrides. In addition, RBS allows to measure the layer thickness and, most important, the In or Al content independently of the influence of strain. Therefore, besides XRD-measurements, RBS has become generally accepted as a technique for measuring the composition of semiconductor alloys [126]. For RBS and channeling measurements a 2.0 meV $^4He^+$ beam with a current of about 12 nA produced by an accelerator (7.5 meV Van deGraaff at the University of Freiburg) was used with a backscattering angle of 165°. Details of the experimental setup and the measurements are found in Portman and colleagues [127]. The layer thickness and the In or Al concentrations in the samples can be determined directly from the backscattering yield of the randomized sample orientation [128]. For this purpose, the samples are rotated on an 8° cone around the beam axis during the measurement. The evaluation of these measurements is carried out using the program "RUMP" [129]. The dechanneling yields are normalized to the backscattering yield. To compare the dechanneling yields of different samples, the random backscattering yields are also normalized to each other. In Figure 9.12a the normalized yield versus channel number, which is linearly correlated to the energy of the scattered ions, is plotted for random (upper open circles, RBS spectrum) and ⟨100⟩ aligned direction (lower full circles, channeling spectrum). From RUMP simulations (solid line in Figure 9.12a), an epilayer thickness of 820 ± 40 nm is estimated for this sample. The interface between the GaN layer and the GaAs substrate can be seen around channel number 390. A low minimum yield at the surface is found in the ⟨100⟩ channel, which is increasing slowly with increasing depth. The axial angular scan in ⟨100⟩ direction of the same sample is shown in Figure 9.12b. From a numerical fit a normalized minimum yield, χ_{min}, of 0.28 and a half-width at half angles, $\Psi_{1/2}$, of the angular scan spectra of 0.69° are determined, respectively. For a second thinner sample (not shown here), both χ_{min} and $\Psi_{1/2}$ increased. This increase of the minimum yield and broadening of the channeling dip may be caused by a mosaic spread of crystallites within the epilayers.

To determine the defect type responsible for dechanneling, the minimum yield at the surface must be normalized to the minimum yield, χ_V, of a

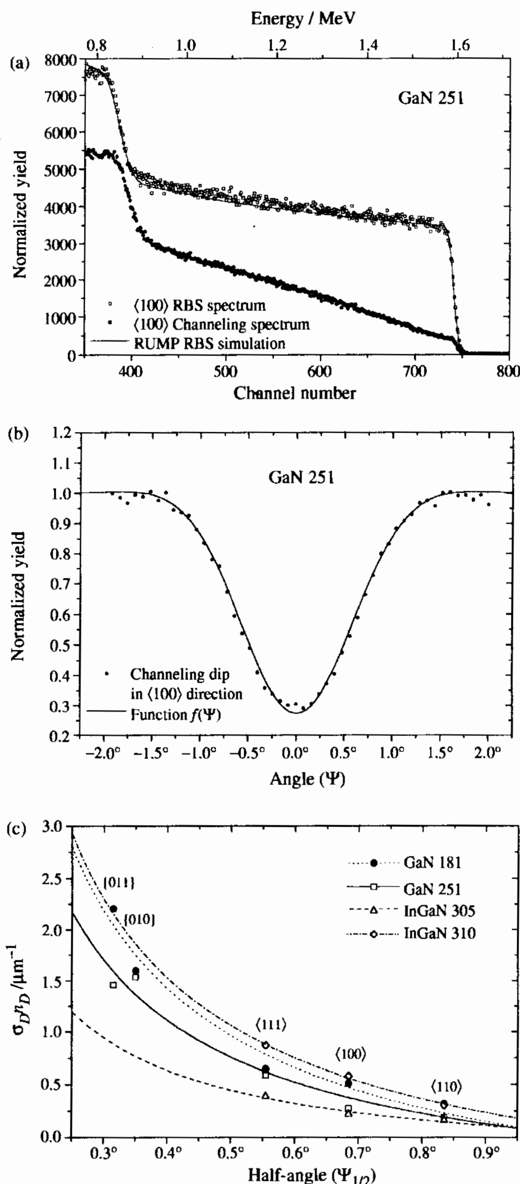

Figure 9.12 (a) RBS and channeling measurements on a cubic GaN/GaAs(001) sample. The solid line shows the RUMP [129] RBS simulation. The interface between the GaN layer and the GaAs substrate can be seen around channel number 390; (b) axial angular scan in ⟨100⟩ direction of the sample. From the fit (solid line a value of χ_{min} of 0.27 is estimated; (c) $\sigma_D n_D$ plotted versus half-angle of the angular scans of a perfect crystal. The lines approximate the data, assuming the inverse proportionality of the dechanneling factor σ_D to the half-angle $\Psi_{1/2}$. The axis or plane belonging to $\Psi_{1/2}$ are shown.

Table 9.3 Layer thickness, normalized minimum yield, χ_{min}, and half angles, $\Psi_{1/2}$, of the angular scan spectra in ⟨100⟩ channeling direction and calculated dislocation densities, n_D, of two cubic GaN/GaAs (001) epilayers

Sample	*Thickness (nm)*	χ_{min}	$\Psi_{1/2}$ (°)	n_D (cm^{-2})
GaN 181	465 ± 23	0.43	1.07	1.3×10^{11}
GaN 251	820 ± 40	0.28	0.69	7.0×10^{10}

nearly perfect crystal. Due to the lack of such a perfect, defect-free crystal, we use the approximations for χ_V in a perfect crystal given by Lindhard [130] and Barrett [131]. The normalized minimum yields are proportional to the product of the dechanneling factor, σ_D, and defect density, n_D. In Figure 9.12c this product $\sigma_D n_D$ is plotted versus the measured half-angle $\Psi_{1/2}$ for different channeling directions (⟨110⟩, ⟨100⟩, ⟨111⟩) and channeling planes ({011}, {010}) and for two different GaN and InGaN samples. In all samples, $\sigma_D n_D$, and therefore σ_D, is approximately inversely proportional to $\Psi_{1/2}$. This dependence of σ_D on $\Psi_{1/2}$ indicates that scattering on dislocations predominantly contributes to the dechanneling in our samples [132]. From the knowledge of the predominant defect type it is possible to calculate the absolute defect concentration [132]. In all cases the dislocation densities are in the order of 10^{10} to 10^{11} cm^{-2}. The layer thicknesses estimated by RUMP simulation, the half-width at half minimum (HWHM) of the anglular scan in ⟨100⟩ channeling direction and the estimated dislocation densities are summarized for two different thick *c*-GaN/GaAs(001) samples in Table 9.3.

The calculated dislocation densities are within experimental uncertainty of the same order of magnitude as that estimated from HRXRD and TEM measurements reported earlier. This confirms the observation that with increasing layer thickness, the dislocation density decreases in the cubic group III-nitrides.

9.4.3 Optical Properties

9.4.3.1 Refractive index and extinction coefficient

There are only a few studies concerning the fundamental optical properties of *c*-GaN, probably because the metastability of the cubic phase gives rise to difficulties in growing thick enough *c*-GaN layers with a high-phase purity. Petalas and co-authors [133] reported only pseudodielectric functions for the layered structures close to the bandgap as determined by ellipsometry, however, no analysis concerning the refractive index (n) of cubic GaN was performed. Data for n below the bandgap have been published by Lin and coworkers [134] for *c*-GaN grown on GaAs and by Vidal and

colleagues [135] for c-GaN/MgO. At low energies (1.5 eV) they differ by about 7 percent, and the difference increases toward the bandgap.

The discrepancy can be related to methods applied in analyzing the transmission/reflection spectra. First, the data obtained are principally determined by the accuracy of the measured film thickness which was estimated to be of ± 30 nm [134] and ± 100 nm [135]. Second, surface roughness and/or a possible interface layer between the film and the substrate, which are known to have a strong effect on the magnitude and energetic position of reflection and transmission interference extrema [136–138], are not taken into account in both References 134 and 135. These effects can lead to an essential inaccuracy of the determined refractive index, because it was obtained either as an adjustable parameter from a fit to reflectivity spectra [134] or by measuring the envelopes of the maxima and minima of transmission interference fringes [136] with subsequent analysis using a procedure that is valid only within a one-layer model.

Recently, the refractive index and extinction coefficient of c-GaN in the energy range of 1.5 to 3.7 eV has been determined at room temperature with high accuracy using combined reflectivity and spectroscopic ellipsometry measurements [139]. A multisample fit has been used to obtain averaged values for the refractive index and the extinction coefficient. The corresponding results are shown by the solid lines in Figure 9.13a and 9.13b, respectively. For comparison, previously published data are also presented by triangles [134] and squares [135], where surface and interface properties were not taken into account in determining the refractive index from optical studies of epitaxial films. The roughness of the c-GaN film surface has been studied independently by atomic force microscopy (AFM) and increases with increasing film thickness. For a 1.16-μm-thick c-GaN sample, a typical root mean square (rms) value of the surface roughness, δ_{AFM}, of 12.2 nm is measured by AFM, which is in excellent agreement with that estimated from the fit of the reflectivity data, δ_R, of 11.7 nm. In addition, for a quantitative analysis of the data, a nonabrupt substrate-film interface layer, which is assumed to be a mixture of both materials (GaN and GaAs), must be assumed. Details of the analysis are given by Köhler and colleagues [139].

The consistency of the developed method is demonstrated if the obtained optical parameters are used to fit the reflectivity spectra. Corresponding results for the 1.16-μm-thick c-GaN sample are shown in Figure 9.14. An excellent agreement over the whole measured spectral range between experimental data (open circles) and the fit is found.

9.4.3.2 PL data

Figure 9.15 shows the PL spectrum at 2 K in a semilogarithmic plot for a 0.8-μm-thick stoichiometrically grown c-GaN epilayer deposited on a (001) GaAs substrate. The near band-edge spectral range is dominated by

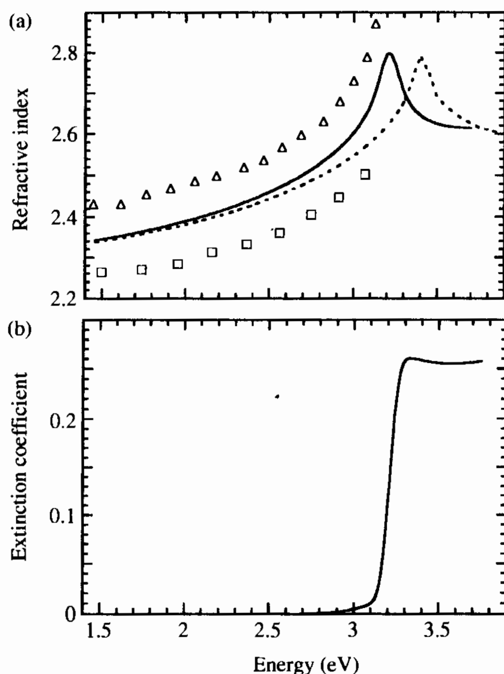

Figure 9.13 (a) Refractive index of cubic GaN as obtained from a multisample fit (solid line). Triangles and squares are data of References 134 and 135, respectively. The dotted line shows for comparison data for hexagonal GaN [138]. (b) corresponding results for the extinction coefficient of *c*-GaN.

two well-resolved peaks at about 3.26 eV and 3.15 eV with an FWHM of 24 meV and 43 meV, respectively. As shown below, temperature-dependent measurements of these two lines allow one to assign the 3.26 eV emission to radiative recombination of an acceptor-bound exciton (A^0, X) and the 3.15 eV line to a donor–acceptor recombination (D^0, A^0) [10]. Above 3.3 eV, which is the value of the low temperature gap energy of the cubic GaN measured by photoreflection [45], the PL-intensity drops by more than three orders of magnitude. In this spectral region we find no trace of near–band-edge or defect-related [140] emission lines from inclusions of hexagonal crystal structure. In the energy range below 3.1 eV, at least six further optical transitions (indicated by arrows in Figure 9.15) can be observed in the PL-spectrum. With decreasing energy, the transitions occur at 3.07 eV, 3.03 eV, 2.97 eV, 2.85 eV, 2.65 eV, and 2.4 eV. The intensity of these peaks are by more than one order lower than that of the dominating (D^0, A^0) transition and vary significantly between different samples. Temperature-dependent measurement of these lines shows no characteristic 25 meV shift as has been observed for the 3.15 eV (D^0, A^0) transition.

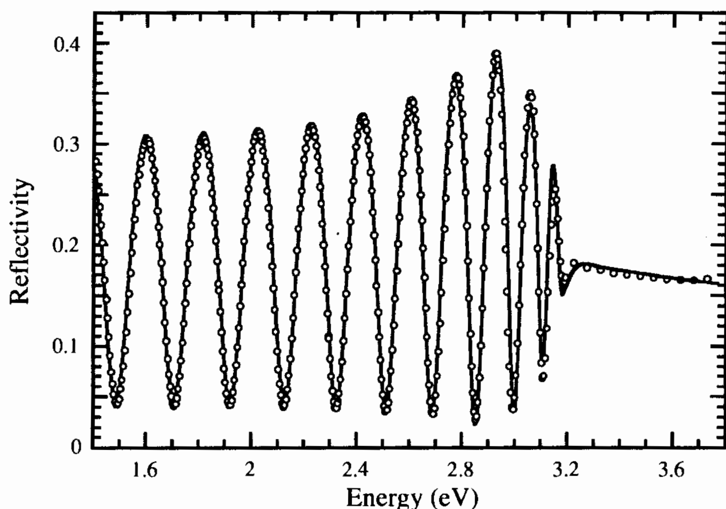

Figure 9.14 Reflectivity versus energy of a 1.16-μm-thick cubic GaN epilayer with an rms surface roughness of $\delta_{AFM} = 12.2$ nm measured by AFM. The open circles are the experimental data and the solid line is a fit, taking into account both surface roughness and a nonabrupt substrate-film interface.

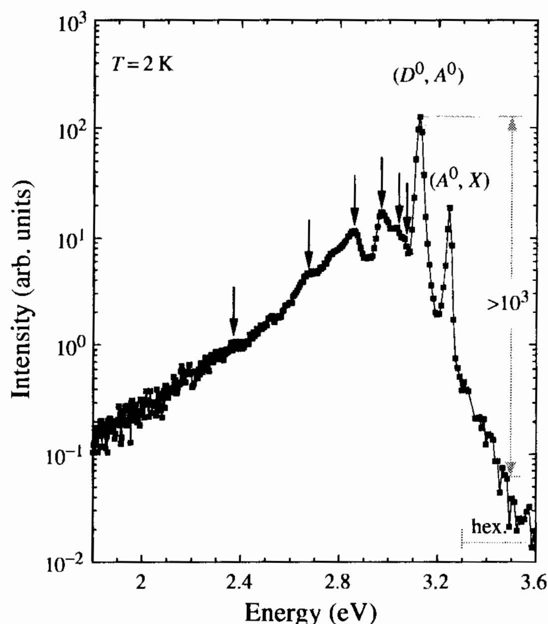

Figure 9.15 2 K PL spectrum of a 0.8-μm-thick cubic GaN epilayer.

For that reason, these lines are either band-acceptor (e, A^0) or donor-hole (D^0, h) transitions. Due to the larger binding energies of the involved defects, the corresponding wavefunctions may be strongly localized. This reduces the recombination probability for donor–acceptor transitions and favors the band-impurity transition. Using a band-gap energy of 3.302 eV [45], the energy levels of the defects are estimated to be 0.232 eV, 0.272 eV, 0.332 eV, 0.452 eV, 0.652 eV, and 0.902 eV above the valence band or below the conduction band of c-GaN, respectively. Similar defects in c-GaN have also be seen by Zinov'ev and coworkers [141].

Additional valuable information about the electronic band structure of cubic GaN epilayers can be provided by studying the temperature and pressure dependence of the optical transitions in semiconductors [10,142]. In Figure 9.16 the temperature dependence of the 3.26 eV (full triangles), the (e, A^0) transition (full squares), and the (D^0, A^0) transition (full circles) are plotted versus temperature. At temperatures above 100 K the peak position of the exciton line follows the energy gap (full curve in Figure 9.16) measured by photoreflectance [45]. Assuming an exciton binding energy $E_{exc} = 26$ meV, the dotted line represents the temperature dependence of the exciton emission energy. Above 100 K there is excellent agreement

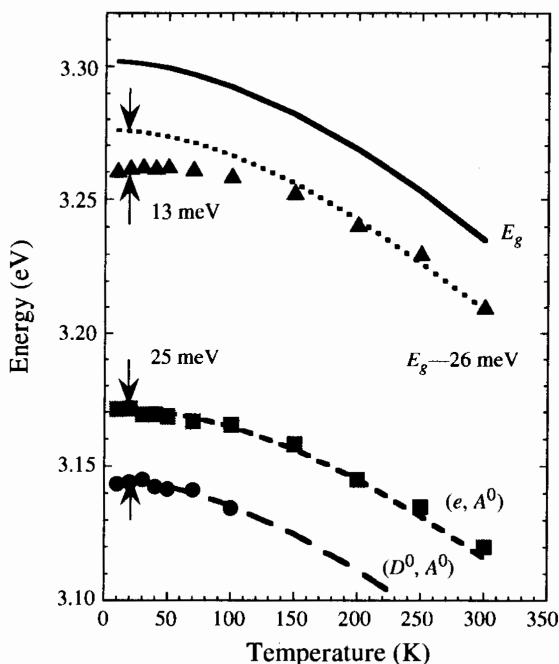

Figure 9.16 Temperature dependence of the near–band-edge emission.

between the experimental data and this curve. The 13 meV deviation at low temperatures is attributed to an increasingly stronger contribution of bound exciton transitions. Using Haynes rule [143], which has been confirmed in hexagonal GaN [144], and assuming that the excitons are bound to acceptors, we obtain an acceptor ionization energy of about 130 meV. This agrees well with the acceptor binding energy evaluated from the (D^0, A^0) transition.

With a donor and acceptor energy of 25 meV and 130 meV, respectively, and the temperature dependence of the energy gap [45], a temperature-dependent emission energy of the (e, A^0) and the (D^0, A^0) transition as indicated by the dashed and dashed-dotted curves in Figure 9.16 are obtained. The good agreement between the experimental data and the calculated curves supports the interpretation that in the cubic epilayers, a shallow donor with $E_D = 25$ meV and an acceptor with $E_A = 130$ meV are involved in the observed near-band PL.

Figure 9.17 shows representative near band-edge PL spectra of a cubic GaN sample measured at 10 K for different hydrostatic pressures. At low temperatures and for photon energies above 2.8 eV, the PL emission is dominated by the no-phonon bound-exciton recombination (A^0, X), the (D^0, A^0) transition and a line labeled L_2, respectively. The energy position of the lines labeled L_1 and L_3 is inferred from the analysis of PL spectra taken at different

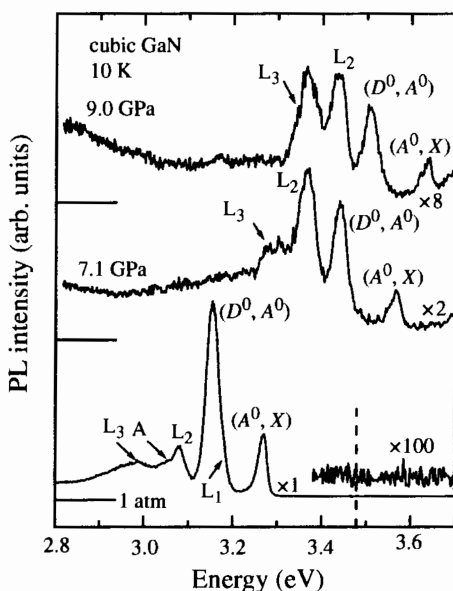

Figure 9.17 PL spectra of cubic GaN measured at 10 K for different pressures.

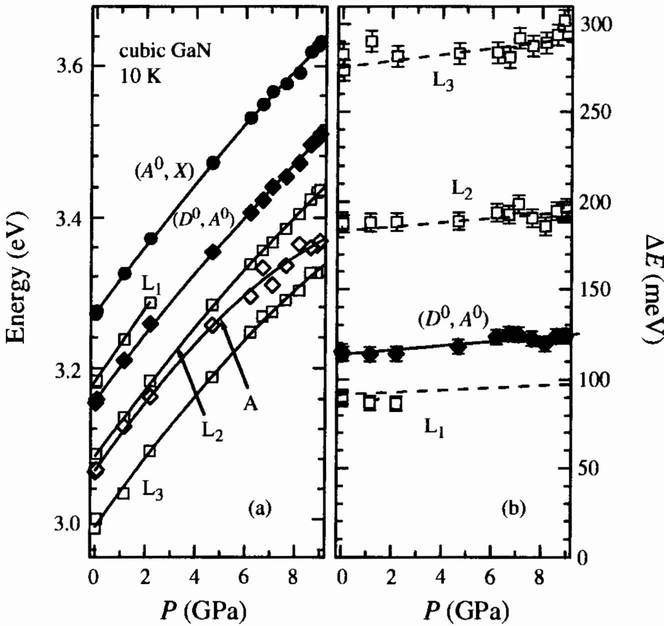

Figure 9.18 Energy shifts as a function of pressure.

pressures and power densities, where these emissions are resolved as a high-energy shoulder of the (D^0, A^0) line and a peak on top of the broadband at about 3 eV, respectively. With increasing pressure, all PL features above 2.8 eV shift to higher energies while decreasing in intensity. The latter effect is primarily due to the lower throughput of the optical setup and the poorer detector response in the ultraviolet (UV) range above ~3.3 eV. For each pressure, the PL spectra are analyzed by fitting Gaussian-line profiles in order to obtain the corresponding PL-peak energy, intensity, and linewidth. In Figure 9.18 the results for the pressure dependence of the PL-energies measured at 10 K are summarized. The solid lines represent least-square fits to the experimental data using second-order polynomials. The pressure coefficients obtained here for the (A^0, X) and L_n lines as well as for the (D^0, A^0) transition differ by less than 10 percent from that of the hexagonal modification of GaN [145]. We can expect the pressure dependence of the direct-gap energy, E_{Gap}, of the cubic phase to be essentially that exhibited by the bound exciton transition, except for a rigid shift of E_{Gap} to higher energy as given by the total exciton binding energy. This implies that the other observed emission peaks arise from optical recombination processes involving electronic states which are closely related to the band-edge of c-GaN. This holds with the exception of an additional feature (labled A) which is apparent

from the PL spectra between the L_2 and L_3 emissions and shows a marked sublinear pressure shift (open diamonds in Figure 9.18a). The emission at 3.06 eV is probably related to a deeper impurity level. Using a quadratic relation, the pressure dependence of the *c*-GaN energy gap can be expressed by $E_{Gap} = 3.302\,\mathrm{eV} + 0.046\,\mathrm{eV/GPa} \times P - 0.00067\,\mathrm{eV/GPa}^2 \times P^2$, with the pressure P.

The energy difference, ΔE, between the exciton line and the (D^0, A^0) and L_1, L_2, and L_3 lines is plotted in Figure 9.18b and is nearly constant over the whole pressure range investigated. In highly polar materials like GaN, a stronge electron–phonon interaction is expected, leading to the observation of multiorder LO-phonon assisted emission. At ambient pressure, the energy separation between the exciton and the L_1, L_2, and L_3 peaks is nearly an integer times the LO-phonon energy (92 meV) of *c*-GaN. This also holds under pressure as indicated by the dashed lines in Figure 9.18b, which represent the Raman scattering results for the pressure dependence of the LO-phonon and its overtone energies in *c*-GaN [146]. Within experimental uncertainty, this agreement between PL and Raman data implies that the L_n-lines are LO-phonon replicas of the exciton transition.

The dominating near-band transitions [(D^0, A^0), (A^0, X) lines] are observed in all cubic GaN epilayers independent of the growth technique used and also independent of the substrates used. Therefore, the ratio of the PL-intensities of the (D^0, A^0) and bound-exciton (A^0, X) lines is often taken as a measure for the quality of the epilayers [91]. However, because the nature of these two transitions is different, the intensity ratio depends on the excitation intensity conditions. Recently, Daudin and colleagues [64] also showed that the ratio of these lines depends strongly on the Ga/N flux ratio and increases for Ga-rich conditions. Therefore, it is not possible to use this ratio to compare different samples grown by different growth techniques if they are grown at different laboratories.

Figure 9.19 shows the FWHM of the (D^0, A^0) and bound exciton (A^0, X) lines and the FWHM of the ω-scans of the GaN (002) Bragg reflex as a function of layer thickness. Both the FWHM of the (D^0, A^0) and the FWHM of the ω-scans show a significant and very similar variation with layer thickness. As already mentioned, the FWHM of the ω-scan is correlated to the density of extended defects in the layers. The full line in Figure 9.19 shows the trend of the density of dislocation lines calculated by the model given by Ayers [125]. Both the (D^0, A^0) linewidth and the rocking curve linewidth follow this trend, indicating that the (D^0, A^0) linewidth also correlates with dislocation density. Therefore, the FWHM of the (D^0, A^0) transition can be used to compare the dislocation density of different samples measured by different groups at different times. In contrast, the linewidth of the (A^0, X) is nearly independent of the layer thickness (dashed line), which is probably due to the small excitonic radius in GaN.

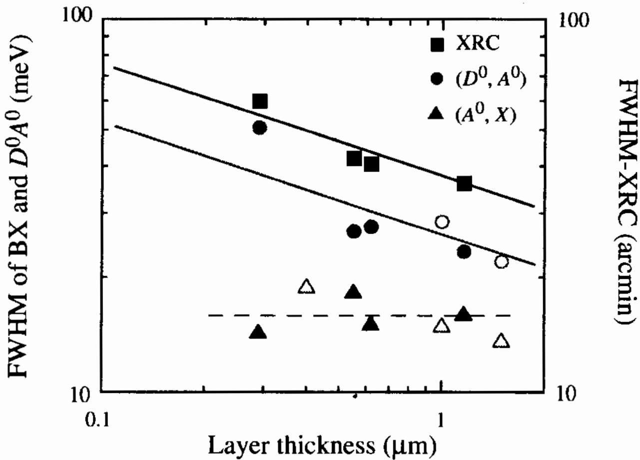

Figure 9.19 FWHM of the PL-linewidths of the bound exciton transition (A^0, X), and donor–acceptor pair transition (D^0, A^0), x-ray rocking curve (full squares) versus thickness of the cubic GaN epilayers. The full line shows the trend proposed by the "dislocation glide model" of Ayres [125]. The open symbols are PL-data from References 54, 64, and 91.

9.4.3.3 Cathodoluminescence (CL) data

At room temperature and under high e-beam excitation conditions (acceleration voltage $V_b = 12\,\text{kV}$, e-beam current $I_b = 15\,\text{nA}$), the cathodoluminescenc (CL) spectrum of the stoichiometrically grown sample is dominated by the near-band emission at 3.2 eV with an FWHM of 55 meV. This is within the narrowest room temperature linewidth reported thus far for cubic GaN. The CL-spectrum is seen in the inset of Figure 9.20 (lower curve). Detailed lineshape analysis of this spectrum reveals that the emission consists of an excitonic and a band-accceptor (e, A^0) transition [147]. Similar observations have been made by Yang and colleagues [124], however the FWHM of their luminescence lines was at least twice as large. Using the free-exciton energy of 26 meV [10], a bandgap energy of 3.230 eV is calculated for c-GaN at room temperature. This value is in excellent agreement with other published values [45]. The approach of the (e, A^0) transition to the bandgap is due to the ionization of the donors and to an additional correction term of $k_BT/2$ resulting from the thermal distribution of the free carriers in the conduction band. No deep-level emission can be seen under this excitation condition.

By reducing the excitation intensity of the e-beam, a broad CL-emission band at 2.4 eV is measured at room temperature. This is depicted in the upper curve of the inset of Figure 9.20 (upper curve). For better comparison both spectra have been normalized to the near–band-edge emission. The strong variation of the intensity ratio between the deep luminescence at 2.4 eV and the near–band-edge luminescence with increasing excitation

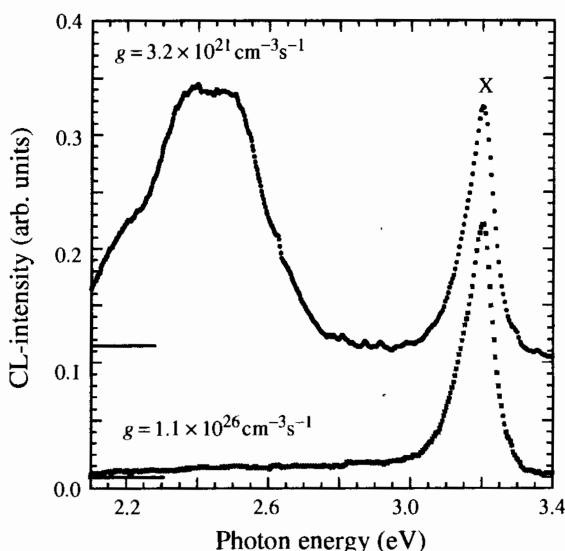

Figure 9.20 Room-temperature CL spectra of *c*-GaN excited with 10 keV electrons: (a) high excitation, (b) low excitation.

intensity is shown in Figure 9.21. In this diagram, the peak intensities of both emission bands are plotted versus the electron–hole generation rate, which is calculated using a standard model for the generation of the CL signal [148]. Changing the e-beam current and its focus allow us to vary the generation rate by seven orders of magnitude [147]. The full lines in Figure 9.21 are calculated curves using a simple model developed by Grieshaber and co-authors [149]. It has successfully been applied to hexagonal GaN for the near–band-edge emission and the so-called yellow-emission band. The model describes the intensity of two radiative transitions as a function of the excitation intensity and is based on rate equations which take into account transitions between shallow impurities, deep levels, and continuum states. If the different transition times are known, the deep-level concentration can be estimated. For *c*-GaN, a reasonable transition time is about 0.1 ns [150]. Using this value for the different recombination paths, a defect concentration in the order of 10^{16} to 10^{17} cm^{-3} is estimated. With these parameters, an excellent agreement between experimental data and model calulation is found (full curves in Figure 9.21). Due to the observed strong excitation intensity dependence, the deep level at 2.4 eV is excluded to be relevant for optical devices like LEDs or LDs, which operate at much higher excitation conditions.

Depth-resolved measurements by varying the acceleration voltage of the e-beam show a homogeneous distribution of the 2.4 eV emission line, whereas the near–band-edge luminescence strongly already decreases

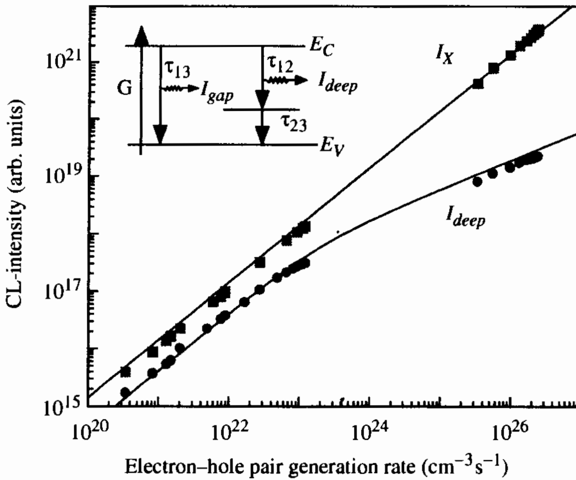

Figure 9.21 CL-intensity of the near–band-edge luminescence, I_{gap}, and the 2.4 eV emission, I_{deep}, versus the electron–hole pair generation rate, G. Symbols are experimental data. Curves are calculated for $\tau_{12} = 1$ ns and a concentration of deep recombination centers $N_0 = 10^{17}\,\text{cm}^{-3}$ (dashed), and $\tau_{12} = 100$ ps and $N_0 = 10^{16}\,\text{cm}^{-3}$ (full), respectively. The inset shows the proposed recombination model.

at 0.3 μm. No evidence for an increase of the density close to the GaN/GaAs interface is found. However, the density of nonradiative recombination centers increases toward the GaN/GaAs interface.

9.4.4 Stimulated Emission and Optical Gain

For laser applications, the optical gain is the most important parameter to be known. The optical pumping technique is the method capable of providing the very high excitation densities necessary for the occurrance of stimulated emission and lasing. Usually a pulsed laser is used for optical pumping in order to generate sufficient numbers of carriers in the conduction band. To obtain the high excitation density necessary for gain investigations, a dye laser pumped by an excimer laser is used, providing pulses with a duration of 15 ns at a rate of 30 Hz and a total energy of up to 20 μJ at 340 nm. A schematic drawing of the experimental set-up is shown in Figure 9.22. The sample is mounted in a bath cryostat at 1.8 K. Gain measurements are performed using the variable-stripe-length method [151] both at 1.8 K [4] and at room temperature [152]. The excitation spot is focused onto a $L \times 50\,\mu\text{m}^2$ stripe, where L denotes the excitation length.

At 1.8 K the gain spectra for various excitation densities up to $10\,\text{MWcm}^{-2}$ are displayed in Figure 9.23 of a 3-mm-long cubic GaN sample. The spectra are smoothed to enhance the visibility of the observed

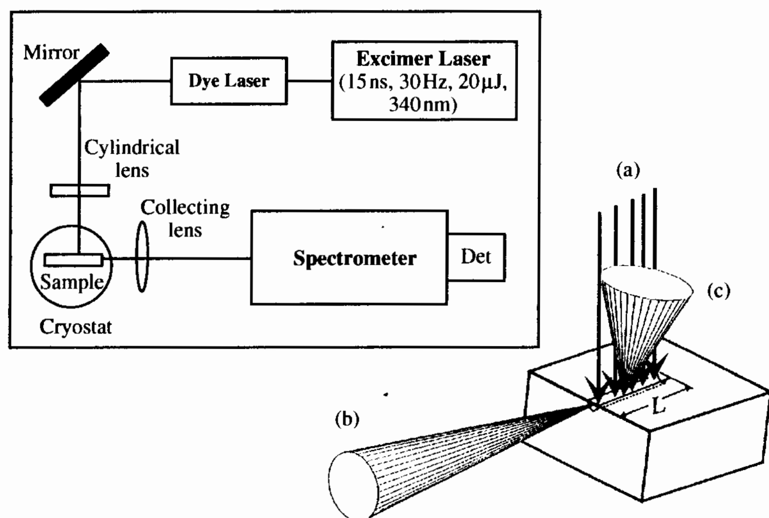

Figure 9.22 Schematic drawing of the experimental set-up for gain measurements using the variable strip length method. On the right side, the schemes of optical pumping is depicted: (a) excitation beam with variable length of excitation stripe (L), (b) emission collected from the sample edge (gain measurement configuration), and (c) emission collected from the top of the sample (PL configuration).

spectral features. The threshold to obtain optical gain is 150 kWcm^{-2}, resulting in a small structure at 3.265 eV with a gain value of 10 cm^{-1}. From the spectral position only a biexciton decay—denoted as M in Figure 9.23—is likely to be responsible for this gain structure. Therefore, the biexciton binding energy in cubic GaN can be roughly estimated as 3 meV. In *h*-GaN a value for the biexciton binding energy of 3.7 meV was observed [153]. No gain due to exciton–exciton-scattering—expected at around 3.24 eV—is found. For increasing excitation densities of 500 kW/cm^2 and more, the gain peak shifts above the bandgap of *c*-GaN. The peak position is 3.274 eV at 500 kWcm^{-2} and 3.280 eV at 1.5 MWcm^{-2}. The gain above the GaN band-edge originates from band-filling processes, where the blue shift of the cross-over gain-absorption is caused by a shift of the respective quasi-Fermi levels of holes and electrons into the valence and conduction bands [154]. At an energy of 3.219 eV another gain peak is observed, labeled EHP. With increasing excitation density, this gain peak dominates the spectrum. Its peak position shifts to lower energies with increasing excitation density (3.210 eV at 5 MWcm^{-2}). From the energy position and the intensity dependent behavior, we attribute this gain structure to an electron–hole-plasma. This process provides the highest gain values up to 210 cm^{-1}. In comparison, the hexagonal and cubic GaN epilayers exhibit similar gain mechanisms at comparable excitation densities [155].

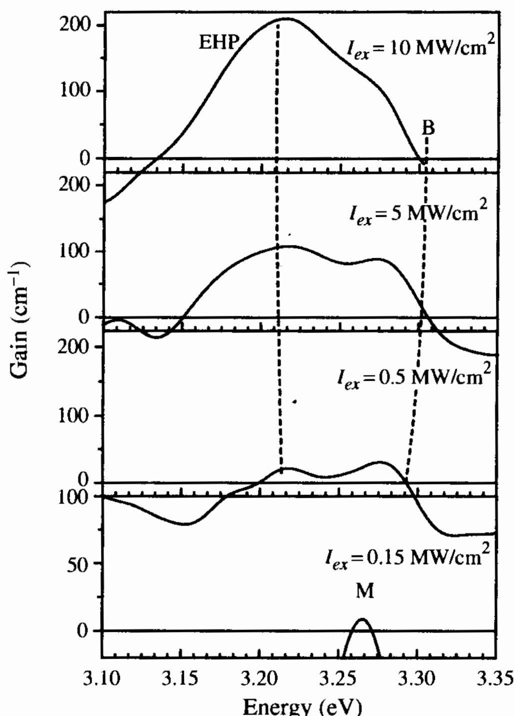

Figure 9.23 Gain spectra of cubic GaN for various excitation densities up to 10 MWcm^{-2} at 1.8 K. The intensity scale of the lowest gain spectrum has been expanded for visibility. The dotted lines indicate the energy shift of the peak position and the crossover gain absorption, respectively.

Figure 9.24 (left side) shows the 2 K spectra of the edge emission from a cleaved sample with a cavity length of 250 μm at different excitation densities on a linear scale. Above the threshold excitation of 1 MW/cm^2 a peak at 3.26 eV appears, exhibiting a strong increase of the edge emission with excitation intensity and a strong polarization dependence. The emitted light is strongly TE polarized, as expected for an edge-emitting cleaved facet. For higher densities up to 5 MW/cm^2, a slight shift to lower energies of the peak position is observed, indicating the increased carrier density in the sample. In Figure 9.24 (right side) the results of intensity-dependent edge emission measurements for 250, 450, and 550 μm *c*-GaN samples are summarized. For all the samples the same optical features are observed—a strongly polarization-dependent stimulated emission peak occurs above a certain threshold, exhibiting a superlinear increase with increased excitation density. The threshold for the onset of stimulated emission increases with reduced cavity length, L, which is in accordance with the well-known formula $I_{thres} \approx L^{-1}$ [156].

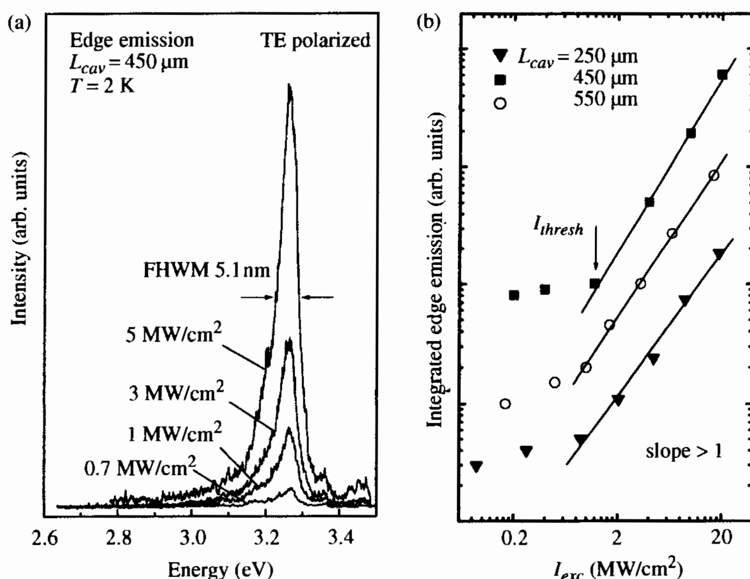

Figure 9.24 (a) TE-polarized edge emission from a cleaved *c*-GaN/GaAs sample with a 450 µm cavity at different excitation densities at 1.8 K; (b) integrated intensity of edge emission spectra versus excitation density from cleaved cavity samples with cavity lengths of 250 µm, 450 µm, and 550 µm, respectively.

The room temperature spectrum of the edge emission of the cleaved sample is shown in Figure 9.25 and exhibits similar optical features as strong TE polarization and superlinear increase of edge emission. From these features the peak can be attributed to the stimulated emission of *c*-GaN. However, no Fabry-Perot modes are observed which are expected to be separated by about 0.4 meV. Imperfections of the cavity facets, excitation pulse variations, and mode hopping are possible reasons for the unstructured stimulated emission spectra. The lateral confinement is believed to be caused by the interface sample-air on one side and the illuminated and nonilluminated parts of the sample on the other. The magnitude of the pump power locally changes the refractive index and, therefore, a lateral confinement necessary for the feedback is provided [157]. This is confirmed by micro-PL measurements, where it was found that the most of the light is emitted from the cleaved facets of the samples.

Similar to observations in hexagonal GaN [158], the threshold value of 1.6 $MWcm^{-2}$ at room temperature also indicates that in *c*-GaN the onset of stimulated emission is less sensitive to changes in temperature. This may be a consequence of the high stability of GaN toward temperature. With a cleaved sample of 450 µm cavity, room-temperature–stimulated emission is observed at 1.6 $MWcm^{-2}$. These are significantly lower threshold values

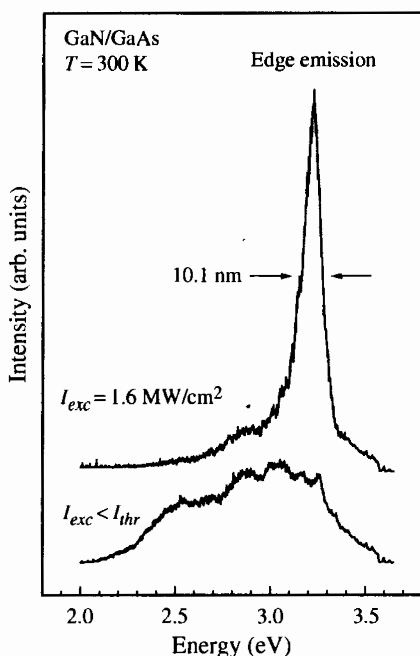

Figure 9.25 Edge emission at room temperature from a c-GaN sample with a cavity length of 450 μm. The upper spectrum shows the stimulated emission above 1.6 MW/cm^2; the lower spectrum is the broad, unstructured emission below threshold.

for cleaved cubic GaN than those reported by Nakadaira and Tanaka [159]. Due to the simple procedure of cleaving laser facets, the high potential for LED applications of cubic III-nitrides is evident.

9.4.5 Electrical Properties

To investigate the electrical properties of cubic GaN, three different types of samples have been grown by plasma-assisted MBE. The first series of samples is grown under N-rich condition (2 × 2 surface reconstruction), the second under stoichiometric conditions (at the phase transition between (2 × 2) and c(2 × 2)), and the third series is grown under Ga-rich conditons (c(2 × 2) RHEED pattern). To determine the electrical properties of these epilayers, Hall effect measurements are performed with square-shaped samples (Van der Pauw geometry) between 240 K and 380 K. Gold wires soldered by In show Ohmic characteristics for this temperature range. The experimental apparatus is equipped with a high impedance current source and a Keithley 7065 Hall effect card. This enables measurements of high resistivity samples up to an input resistance of 100 TΩ.

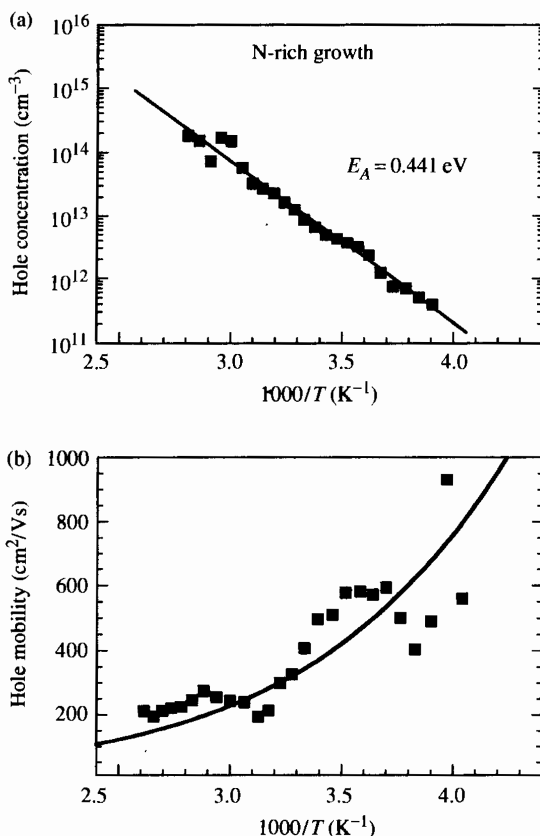

Figure 9.26 The concentration of holes in cubic GaN epilayer (a) and their mobility (b) as a function of $1000/T$. Layers are grown under N-rich conditions ((2 × 2) RHEED pattern, full symbols) conditions.

All measurements are done with the sample in the dark and at a magnetic field of 0.3 T.

Figure 9.26a shows the carrier concentration as a function of the inverse temperature for *c*-GaN layers grown under N-rich conditions (full squares). The hole concentration, p, is obtained from the experimental Hall constant R_H by $p = r_H/qR_H$ (q = electronic charge); the Hall scattering factor, r_H, is assumed to be 1. In the whole temperature range investigated, the samples are p-type. For N-rich *c*-GaN layers, a hole carrier concentration between $2.2 \times 10^{11}\,cm^{-3}$ and $2.8 \times 10^{14}\,cm^{-3}$ is measured. Due to the high resistivity of these samples, reliable measurements are possible only down to temperatures of about 240 K. The temperature dependence of p yields an acceptor activiation energy of $E_A = 0.441 \pm 0.015$ eV. Due to the high

acceptor activation energy, an acceptor concentration of about 2×10^{20} cm^{-3} can be estimated.

The hole mobility μ_h versus $1000/T$ is shown in Figure 9.26b. For samples grown under N-rich conditions, a mobility of 350 cm^2/Vs is measured at room temperature, which is comparable to the best value reported for h-GaN by Rubin and co-authors [160] and is in agreement with recent theoretical calculations [161]. The temperature dependence of μ_h is clearly dominated by polar optical phonon scattering. Using $\varepsilon_\infty = 5.35$, $\varepsilon_0 = 9.5$, $m_0^* = 0.75$ [2], $T_{LO} = 1065$ K [110] for c-GaN, and an expression given by Look [162] for the mobility due to polar optical phonon scattering, μ_{po}, the solid curve in Figure 9.26b is calculated, which is in excellent agreement with the experimental data (full symbols).

The Hall carrier concentration measured as a function of temperature for the nominally undoped c-GaN sample grown under stoichiometric growth conditions is shown in Figure 9.27a. Due to the presence of a residual intrinsic acceptor level, a background hole concentration is measured. This hole concentration increases from $p = 3.7 \times 10^{13}$ cm^{-3} at 100 K to $p = 2.0 \times 10^{16}$ cm^{-3} for $T = 350$ K. The carrier concentration behavior in the low temperature region allows us to determine an activation energy of $E_A = 166$ meV for the acceptor. Therefore, an acceptor concentration of $N_A \approx 4 \times 10^{18}$ cm^{-3} can be estimated for the nominally undoped sample. At temperatures above 300 K, the measured data deviate from the expected values, indicating the contribution of an additional, deeper acceptor level—perhaps the one observed under N-rich conditions. The measured hole mobility is presented in Figure 9.27b as a function of the inverse temperature. The mobility initially increases with temperature, reaching a maximum value of 1250 cm^2/Vs at $T = 120$ K, and then decreases to a value of 283 cm^2/Vs at room temperature. As can be seen in Figure 9.27b, the $T^{3/2}$ behavior, shown at low temperature, suggests that in this region the mobility is limited by ionized impurity scattering. Above 120 K the decrease of mobility is again probably due to phonon scattering.

To study the influence of compensation, the hole mobility is plotted versus hole concentration at room temperature in Figure 9.28 (full triangles). In addition, room temperature values for c-GaN (full symbols) and for h-GaN (open symbols) already published by other authors [20,23,97,160,163,164] are also included in the figure. The full curves represent calculated room temperature mobility values as a function of hole concentration for varying compensation ratios $\Theta = N_D^0/N_A^0$ (N_D^0, N_A^0 concentration of neutral donors and acceptors, respectively) assumes an effective hole mass of $0.75 * m_o$. In this calculation, contributions of polar optical phonon scattering, acoustic phonon scattering, and ionized impurity scattering have been taken into account. At low hole concentration, the mobility is limited to a maximum value of about 300 cm^2/Vs by LO-phonon scattering.

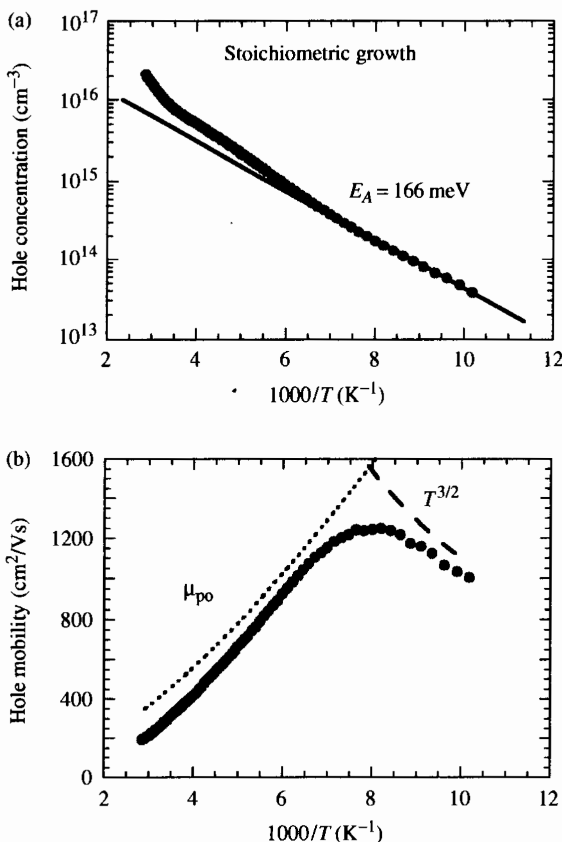

Figure 9.27 Hole concentration (a) and the mobility (b) of a cubic GaN epilayer as a function of $1000/T$. Layer is grown under stoichiometric growth conditions just at the surface phase transition between (2 × 2) and c(2 × 2).

Above $10^{16}\,\mathrm{cm}^{-3}$ ionized impurity scattering and compensation effects reduce the mobility. The experimental data (full triangles) are in agreement with the calculation and follow the upmost curve. This supports the interpretation that polar optical phonon scattering is the dominating scattering mechanism at room temperature. However, the measured hole concentration is to low for an unambiguous determination of the low compensation ratio. Recently published mobility values of c-GaN samples codoped with Be and O [23] are also included in Figure 9.28 and are in agreement with the calculation. The hole mobilities measured for h-GaN (open symbols) are all below the best values reported for cubic samples. Two reasons may be responsible for this effect. First, the effective hole mass may be larger in hexagonal material than in cubic and,

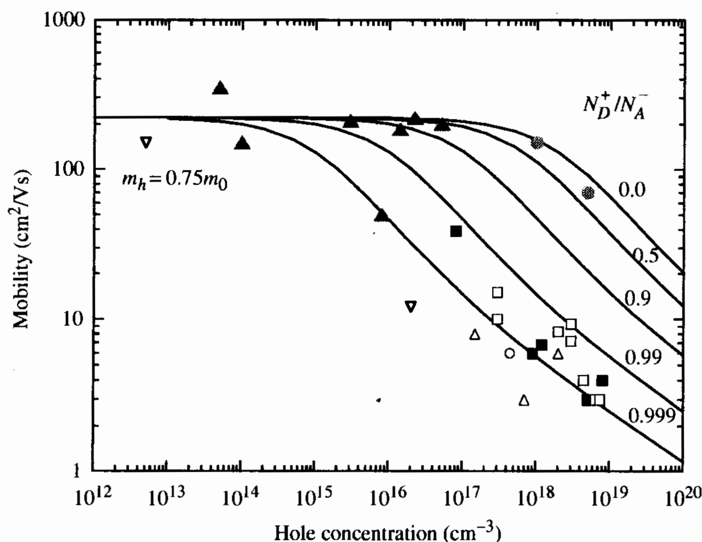

Figure 9.28 Room temperature mobility versus hole concentration for cubic GaN (full symbols) and hexagonal GaN (open symbols). The full lines are calculated values for different compensation ratios $\Theta = N_D^0/N_A^0$.

most likely due to the different growth method, h-GaN may be more compensated.

In contrast to samples grown under N-rich conditions, samples grown under Ga-rich growth conditions ((2 × 2) RHEED-pattern) are n-type [107]. The full squares in Figure 9.28a shows $1/(q|R_H|)$ versus $1000/T$ measured with a c-GaN epilayer grown under Ga-rich conditions on a semi-insulating GaAs substrate. The triangles are the corresponding values of the 450-μm-thick semi-insulating GaAs alone, which is dominated by the thermal activation of the EL2 defect (0.75 eV) [165]. At high temperatures, $1/(q|R_H|)$ of the GaN exceeds that of the GaAs substrate by only one order of magnitude. In addition, the measured mobility (see Figure 9.28b) increases with increasing temperature and is much higher than expected for GaN layers [166]. Therefore, the influence of the underlying GaAs substrate cannot be neglected and a two-layer model [165] for the evaluation of the epilayer doping level is used. The temperature dependent electron concentration in the GaN epilayer shows two different slopes at low and high temperatures, yielding two donor levels at $E_D = 0.16 \pm 0.07\,\text{eV}$ and $E_{DD} = 0.60 \pm 0.10\,\text{eV}$. Similar donor levels have been observed in n-type h-GaN layers by Götz and colleagues [167,168]. The temperature dependence of the electron mobility in the GaN layer is assumed to be dominated by polar optical phonon scattering at high temperatures and by

scattering at dislocations [169] at low temperature. From the half-width of x-ray rocking curves and RBS measurements, the number of dislocation in the samples is estimated to be about 10^{10} to 10^{11} cm^{-2}. The mobility μ_{GaN} in the GaN epilayer is than calculated via Matthiessen's rule [162]. The calculated curves for $1/(q|R_H|)$, μ_H (full curves), n_{GaN}, μ_{GaN} (dashed curves), the shallow and deep donors, and μ_{po} and μ_{disl} (dotted lines) are also shown in Figures 9.29a and b, respectively. The general trend that μ_H increases with increasing temperature is reproduced, supporting the interpretation that a two-layer model is necessary for the explanation of the experimental data.

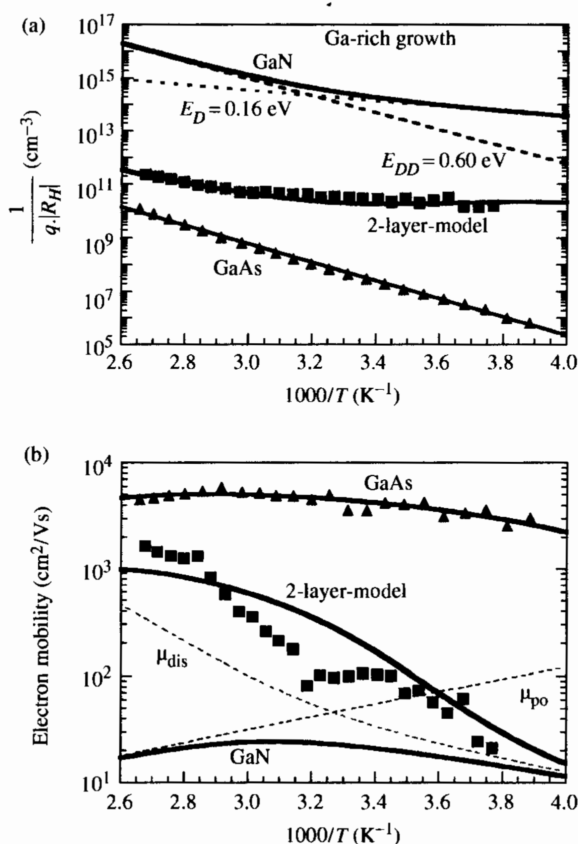

Figure 9.29 Full squares are experimental data of (a) $1/q \cdot |R_H|$ and (b) mobility as a function of $1000/T$ for a c-GaN epilayer grown under Ga-rich conditions ($c(2 \times 2)$—RHEED pattern) on a semi-insulating GaAs substrate. Full triangles are experimental data of the GaAs-substrate alone. Dashed and dotted curves are the assumed input data for the two-layer model calculations (full curve).

The effect that the conductivity of the underlaying GaAs is seen only for n-type layers may be due to the alignment of the band-edges in GaN and GaAs. Recent measurements of the conduction band discontinuity between GaAs and GaN by angle-resolved photoelectron spectroscopy report a very small conduction band offset of only 0.03 eV [170]. Therefore, for electrons nearly no barrier exists to drift into the highly mobile GaAs substrate and two-layer conductivity occurs. However, for holes the large valence-band discontinuity prohibits this effect.

For materials grown by MBE, the nature of the impurities is usually better known than by other vapor phase epitaxy techniques. Only very few foreign impurities are expected to residually contaminate the grown epilayers. Apart from native defects such as vacancies of Ga (V_{Ga}), vacancies of N (V_N), or antisite defects such as Ga_N and N_{Ga}, foreign impurities may diffuse from the substrate or will be built in via the vapor from insufficient pure source materials. This forms a residual background of dopants. In the case of GaAs substrates, As as well as C could probably contaminate the GaN epilayers.

A theoretical consideration of the positions of defect energies [171–173] shows very close proximity to our experimental results. In Figure 9.30, the theoretically proposed energy levels of intrinsic defects calculated by tight binding [171] and ab-initio method [172,173] are depicted. Due to the lack of data for cubic GaN, data for hexagonal GaN are used. Within the accuracy of calculations and experimental errors, only the energy levels of the V_{Ga} and N_{Ga} are deep hole traps. Their ionization energy is in agreement with the measured activation energy $E_A = 0.445$ eV for the p-type c-GaN layers, which are grown under N-rich conditions. Due to the high activation energy of these defects, only a very small fraction ($<10^{-7}$) is thermally ionized and contributes to the p-type conductivity measured. From the measured hole concentration and the activation energy, a quite large defect concentration of about 10^{20} cm^{-3} is estimated.

With increasing Ga-pressure, the number of V_{Ga} or N_{Ga} defects will be reduced. For layers grown under stoichiometric conditions, diffusion of As or C from the substrate may lead to the residual p-type doping of

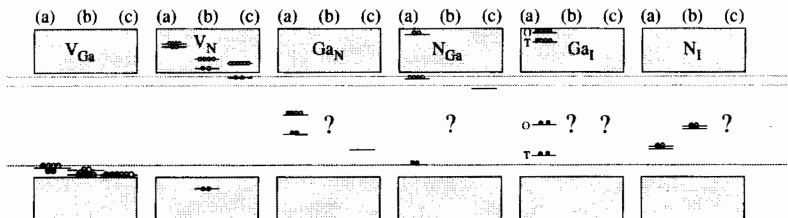

Figure 9.30 Energy levels of intrinsic defects calculated for hexagonal GaN after (a) Boguslawski et al. [172], (b) Neugebauer et al. [173] and (c) Jenkins et al. [171].

about 10^{16} cm^{-3}. Both the group IV impurity C_N as well as the isoelectronic impurity As_N on the N site are expected to form defect states just above the valence band of GaN [171,172]. Another posible explanation for the residual p-type doping of cubic GaN epilayers may be electrically active dislocations. X-ray measurements and RBS experiments showed that the dislocation density, N_{disl}, is in the order of 3×10^{11} cm^{-2} for 0.7-μm-thick cubic GaN layers. Dividing N_{disl} by the lattice constant of c-GaN ($a_{cub} = 0.452$ nm) a residual acceptor concentration of about 6×10^{18} cm^{-3} is estimated. This value agrees within experimental error with the acceptor concentration estimated from the temperature-dependent Hall measurements for the stoichiometric case.

A further increase of the Ga-vapor pressure results in the formation of a sufficient amount of V_N or in the introduction of shallow donor impurities such as Si or O which compensate the residual acceptor impurities and converts the conductivity to n-type.

9.4.6 As: An Isoelectronic Impurity or An Ideal Surfactant

The interaction between As and GaN has long been recognized to be important for material properties on nitride semiconductors. There exists significant interest in the formation of the nitride alloys $GaAs_yN_{1-y}$ and $In_xGa_{1-x}As_yN_{1-y}$ [174]. These alloys have been found to exhibit very limited solubility. However, because of the large bandgap bowing [175,176], even the addition of a few percent of N to GaAs or $In_xGa_{1-x}As$ results in a sizeable modification (reduction) of the bandgap. This allows the realization of long-wavelength semiconductor lasers with high temperature stability for optical fiber communication [177,178]. A large red shift in the PL was also observed on the GaN-rich side of $GaN_{1-y}As_y$ [179]. The experimentally estimated bowing factor was 19.6 eV and the maximum As content y of $GaN_{1-y}As_y$ was 0.94 percent, respectively. At growth conditions with higher As fluxes, phase separation was observed. Nevertheless, the addition of small amounts of As to GaN and $In_xGa_{1-x}N$ offers a further way to extend the spectral range of nitride semiconductors into the red.

In this section, the effect of the presence of an As background pressure on growth as well as the effect of incorporation of As in GaN in the diluted limit is discussed. This is particularly an issue in MBE, where previous growth of arsenides in the same chamber results in a high As background. For the growth of cubic GaN the presence of As has the following impacts. First, investigations by Ruvimov and colleagues [180] and Chen and colleagues [181] have shown that the exposure of the layer surface to an As flux during the growth of the first few monolayers at temperatures of about 580 °C to 600 °C (low-temperature buffer layer) results in remarkably flat

GaN-GaAs interface. Detailed studies on the nitridation of the GaAs (001) surface have also been performed by Jung and coworkers [182] and Lu and coworkers [183]. These researchers found that extensive nitridation results in rough surfaces, which favors the growth of hexagonal GaN inclusions. However, a controlled supply of As can suppress the surface roughening during the nitridation process on the GaAs surface, facilitating the growth of high-quality cubic GaN.

The presence of As has been found to completely modify the surface reconstructions observed by MBE-grown samples at temperatures between 600 °C and 800 °C. By exposing cubic GaN (001) grown on (001) SiC substrates to an As background pressure (beam equivalent pressure: 10^{-8} Torr), the originally observed (4×1) (N-rich condition) or (1×1) (Ga-rich condition) surfaces rapidly transform irreversibly to a (2×2) or $c(2 \times 2)$ surface, respectively [184]. Upon increasing or decreasing the Ga flux, the reversible $(2 \times 2)/c(2 \times 2)$ transition is observed, as is usually the case when growing GaN on GaAs. Therefore, it is believed that As is responsible for these latter reconstructions when growth is carried out on GaAs (001) substrates. This behavior is also supported by theoretical calculations which showed that, indeed As-covered reconstructed GaN surfaces have the lowest surface energies [185]. When growing on GaAs substrates common growth temperatures are between 600 °C and 800 °C. At this growth temperature, As desorption from the underlaying GaAs substrate is most probably occuring. Furthermore, to improve the initial surface, an As-stabilized GaAs buffer layer is usually deposited before growth of GaN and a residual As pressure in the order of 10^{-8} to 10^{-9} mbar remains in the MBE chamber.

Besides the reconstruction modification effect, As ambient pressure turned out to affect GaN growing surfaces in two additional ways. First, the reconstructed flat surfaces are stabilized up to temperatures of 800 °C. This allows the growth at higher temperatures, which is preferable for epitaxy to improve crystalline quality. Second, the amount of hexagonal inclusions within the metastable cubic phase is suppressed [186]. In the presence of As during growth, GaN is forced to adopt the crystal structure of the underlying zincblende structure. This is accomplished by an interchange between the mobile active nitrogen species and the As atoms occupying the group V lattice of the zincblende structure. Considering the bond strength of Ga-As (47.7 kcal/mol) and Ga-N (96.8 kcal/mol), N is expected to replace As and bond to Ga more readily. The displaced As atom will recombine with another As atom to form a dimmer, then desorb from the growth surface. These As–As-dimers are proposed to give rise to the observed (2×2) surface reconstruction. Because the Ga–As bonds will initially be formed in a transient state on the surface, the more stable cubic GaAs surface structure will act as a template for subsequent growth of cubic GaN. Therefore, by increasing the As flux, the overall proportion of the cubic GaN phase can

effectively be raised and, at the same time, the hexagonal GaN phase can be reduced. In this way, As acts as an efficient surfactant and improves the phase purity.

The incorporation of As in epitaxial layers of hexagonal GaN on GaAs substrates obtained by MBE has been investigated by means of SIMS, Auger electron spectroscopy (AES), x-ray spectral microprobe analysis, scanning electron microscopy (SEM), and x-ray diffraction [187,188]. Hexagonal GaN layers grown at a substrate temperature of 700 °C and under As flows up to magnitudes of the order of 1 to 2×10^{-5} Torr showed a maximum amount of As in the epilayers of about 1 to 2×10^{19} cm^{-3}, with a homogeneous As distribution over the thickness of the GaN layer. However, SIMS measurements on *h*-GaN epilayers grown under identical conditions on GaP substrates measured similar As concentrations of the order of 10^{19} cm^{-3}. In this way, diffusion of As from the GaAs substrates can be excluded as the source of the incorporated As. Cheng and co-authors [187] further observed that the GaN crystal structure can readily be switched from the hexagonal phase to the zincblende phase by varying the As overpressure. To explain a background doping level of 10^{19} cm^{-3} in the *h*-GaN without external As, a partial pressure of 10^{-9} Torr is needed, assuming that the As_4 attachment probability is equal to 0.5. This value is completely realistic for an MBE set-up in which GaAs is grown regularly. Whereas Ber and colleagues [188] observed that the incorporated As concentration in *h*-GaN is nearly independent on the substrate temperature in the temperature range below 700 °C, Okumura and coworkers [189] also measured by SIMS that, in cubic GaN the amount of As is two orders of magnitude higher for samples grown at 600 °C, compared with samples grown at 800 °C.

To date, the influence of As doping on the optical and electrical properties of cubic GaN has not been studied in detail. Only Okumura and co-authors [189] reported an additional line at about 3.07 eV in the low-temperature PL spectra in samples grown at low substrate temperatures with As exposure. However, because this layer showed severe degradation in layer quality, contrary to their interpretation, the exact origin of this line has yet to be clarified. Theoretically, the behavior of the isolated As isoelectronic impurity and As–As pairs was investigated by Mattila and Zunger [190,191]. In agreement with experimental studies performed on MOCVD-grown *h*-GaN samples, in which isoelectronic As ions were implanted [192], theoretical calculations showed that isolated GaN:As induces a deep, threefold degenerated *p*-like (t_2) defect level about 0.75 eV above the valence band maximum, which acts as the origin of the observed luminescence transitions. As-related luminescence centered around 2.59 eV (480 nm) at room temperature was also reported by Li and colleagues [193] and Tsatsul'nikov and coworkers [194]. In the first case, AsH_3 was used as the As precursor during MOCVD growth, and in the second case a 30-nm-thick GaAs layer was embedded in

a GaN host. During high-temperature overgrowth, diffusion of As resulted in the formation of a thick As-doped *h*-GaN epilayer. The PL-spectrum of this structure resulted in a new line with a maximum at about 2.5 eV.

For the AsH_3 doped epilayers, the As related peak showed a small blue shift with decreasing temperature, from 2.59 eV (480 nm) at room temperature to 2.63 eV (470 nm) at liquid helium temperature. From temperature-dependent CL measurements, a rapid decrease in the As-related peak occured above 100 K and a thermal binding energy of ~50 meV was found. It is well-established that isoelectronic impurities can form hole (electron) traps in semiconductors if their electronegativities are sufficiently smaller (larger) than the atom of the host lattice for which they substitute. If indeed the As-related peak is due to isoelectronic bound excitons, then the electrically neutral As atom, which is less electronegative than the host N atom, should trap a hole first and then bind to an electron through a Coulomb field. The thermal activation energy found is probably the energy it takes to release the electron. Time-resolved PL measurements show a lifetime of about 100 ns for the As-related emission. All these observations are consistent with the assumption that the emission at 2.59 eV (480 nm) is related to isoelectronic-bound excitons.

Using radioactive isotopes an unequivocal proves that the optical transition at 2.59 eV found in PL spectra of *h*-GaN is caused by a recombination center involving one As atom located on an N site was given by Stötzler and colleagues [195]. For that purpose, *h*-GaN epilayers were ion-implanted with the radioactive isotopes ^{71}As and ^{72}Se. The isotope ^{71}As (half-life 64.28 hr) decays first into ^{71}Ge (11.43 d), which finally transmutes into stable ^{71}Ga. The isotope ^{72}Se decays via ^{72}As (26 hr) into stable ^{72}Ge. These chemical transmutations were monitored by PL spectroscopy. As, Se, and Ge were found to produce luminescence bands at 2.58 eV, 1.49 eV, and 3.398 eV, respectively. The half-lives resulting from exponential fits of the PL data were in excellent agreement with the half-lives of the isotopes. Therefore, in *h*-GaN the 2.59 eV emission can unambiguously related to As_N.

Assuming that the same As-related defect level exists in cubic phase GaN and taking into account that the bandgap of cubic GaN is lower by about 200 meV, an As-related transition at about 2.4 eV is expected. Indeed, a broad dominant luminescence band has been observed in cubic GaN epilayers by CL at room temperature at low excitation conditions [147]. In analogy, this band may be attributed to As. Depth-resolved measurements further revealed that the distribution of the deep recombination centers involved in the 2.4 band was homogeneous in almost the whole epilayer. By using a simple recombination model, it was also possible to estimate a concentration of the deep recombination centers of about 10^{16} to 10^{17} cm^{-3} from the CL-intensity dependence versus electron–hole generation rate. As discussed above, both the homogeneous distribution as well as the amount of defect centers are

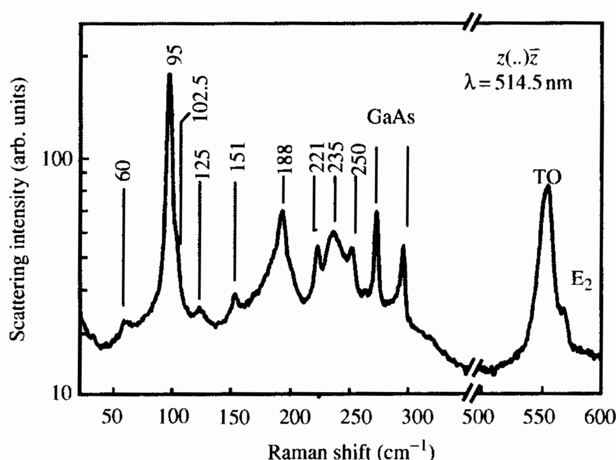

Figure 9.31 Low-temperature Raman spectrum of the defect modes in cubic GaN grown on GaAs. The spectrum was taken in the $z(..)\bar{z}$ configuration at 2 K with excitation at 514.5 nm (2.41 eV).

in agreement with that expection from As-background doping and further confirms the assignment.

The influence of As on the vibrational properties was studied by Siegle and colleagues [196,197]. It was shown that in low-temperature Raman spectra of *c*-GaN films grown epitaxially on GaAs, in addition to the host phonons (TO-phonon 555 cm^{-1}, LO-phonon 741 cm^{-1} [110,116]), a series of sharp lines in the energy range from 95 to 250 cm^{-1} exists. Over 10 lines, the most intense ones located at 95, 125, 150, 190, 220, 235, and 250 cm^{-1}, are shown in Figure 9.31. The intensity of this line decreases nearly exponentially with increasing temperature. The thermal activation energies of the different line were found to range between 10 to 60 meV. Because a vibrational Raman-scattering process should exhibit the opposite temperature behavior, Ramsteiner and co-authors [198] interpreted these excitations as electronic Raman transitions in a shallow donor. However, magnetic-field– and high-pressure–dependent Raman measurements contradict this interpretation and definitely showed that they are of vibrational origin [197]. Low-temperature Raman measurements taken with different excitation wavelengths between 459 nm (2.71 eV) and 647 nm (1.92 eV) further demonstrated a strong resonance behavior of the defect lines. The most intense lines were observed at an excitation energy of 514.5 nm (2.41 eV). This resonance behavior coincides exactly with the broad dominate luminescence band at 2.4 eV observed in CL measurements [147], which therefore is attributed to be As-related. To prove the assumption that the incorporation of As is responsible for these lines, *h*-GaN samples grown on sapphire were intentionally doped with As.

SIMS measurements revealed an As concentration of around $10^{18}\,cm^{-3}$ in this *h*-GaN layer. Indeed, in the low-temperature Raman spectra of these *h*-GaN:As samples, strong lines located at 96, 178, and 235 cm^{-1} appeared, demonstrating that the responsible defects are related to As impurities in the GaN material. Recently, theoretical cluster-model calculation of local vibrational modes using a modified valence-force model of Keating and Kane [199] suggests that the origin of the modes observed at 95, 125, 150, and 250 cm^{-1} are indeed due to *isolated* As impurities in cubic GaN. The broad modes at 190 and 235 cm^{-1} result from other more complicated forms of As incorporation or an As impurity incorporated in the hexagonal modification.

9.5 *p*-TYPE DOPING OF CUBIC GaN

9.5.1 Theoretical Aspects of Different Acceptors

Acceptor doping has been the most serious problem in the fabrication of group III-nitride devices. The decisive breakthrough for *p*-type doping was achieved when Amano and colleagues [96] realized that a LEEBI treatment of Mg-doped hexagonal GaN epilayers convert the previously semi-insulation sample to a *p*-type conducting epilayer. Subsequently, it was realized that both MOCVD and HVPE hydrogen, which acts as a donor, passivates the incorporated acceptor, resulting in the necessity of a postgrowth annealing by LEEBI or by thermal treatments in nitrogen atmosphere [200] to activate the acceptors. This approach, with Mg as the dopant, results in *p*-type epilayers and the achieved hole concentrations were sufficient to realize the first optoelectronic devices emitting in the blue-UV spectral range. However, at room temperature the free hole concentration was limited to a low $10^{17}\,cm^{-3}$. To obtain good Ohmic contacts to the *p*-layer and to decrease the series resistance of the optoelectronic devices, higher hole concentrations are necessary. This requirement initiated an intensive search for alternative acceptors in both hexagonal as well as cubic group III-nitrides. However, to date only Mg has reached the maturity to be used in device production.

The acceptors can be divided into two groups: one that replaces the group III atoms and one that replaces the N atoms. As noted by Neugebauer and Van de Walle [201,202], one of the most important factors is that a dopant is incorporated as a substitional acceptor is its atomic size to fit into the Ga or N site. In Table 9.4, the covalent radius of several column II, column I, and column IV elements, which characterize the atomic size of the substituent, are listed beside Al, Ga, In, N, and As. On N-site, only C is a good candidate, otherwise the atomic radii of the dopants are to large to be substituted. On Ga-site, both column II elements (single acceptor) and column I elements (double acceptor) may be suitable as *p*-type dopants.

Table 9.4 Covalent radii of various elements used for *p*-type and *n*-type doping of GaN as well as the values for the group III elements Al, Ga, In, and of N. Activation energies semi-empirical explanations given by Orton and Pödör [203,204] and theoretical calculations of Neugebauer et al. [201,202], Boguslawski et al. [205,206], Mireles et al. [207], and Bosin et al. [208].

Element	r_{cov} (Å)	*Orton*	*Pödör*	*Neugebauer*	*Boguslawski*	*Mireles*	*Bosin*
Be	0.89	200	~85	96	—	125–133	~100
Mg	1.36	250	250	161	—	130–140	~200
Ca	1.74	—	—	645	—	151–164	—
Zn	1.25	345	340	225	—	162–184	—
Cd	1.41	550	540	—	—	—	—
Hg	1.44	—	680	—	—	—	—
Li	1.23	—	—	387	—	—	—
Na	1.57	—	—	580	—	—	—
K	2.03	—	—	—	—	—	—
C	0.77	—	—	s. acceptor	200	138–148	~400
Si	1.17	—	—	s. donor	s. donor	125–132	s. donor
Ge	1.22	—	—	—	s. donor	—	—
O	0.66	—	—	donor	—	—	—
Al	1.25						
Ga	1.26						
In	1.50						
N	0.70						
As	1.20						

The performance of an acceptor for device applications is determined by three basic criteria: (1) solubility of the dopant, (2) stability against self-compensation, and (3) acceptor level activation energy.

The solubility of a dopant corresponds to the maximum incorporated amount of the impurity in the lattice, which is determined by the formation energy. However, if the formation energy of the element to be incorporated at an lattice site other than the substitution is lower or, if it is advantageous to form complexes, self-compensation may occur, resulting in reduced free hole concentration. Finally, the activation energy of an acceptor determines the number of free holes available for the transport properties of a device. For column II elements, Orton [203] and Pödör [204] were able to estimate values for the activation energies by semi-empirical arguments, which are also listed in Table 9.4. Considering the differences of the electronegativity between the acceptor atom and the host atom which they substitute, a correlation between the acceptor ionization energies and the chemical nature of the acceptor atom was found similar to that in the well-known case of GaAs and GaP [204]. Based on this correlation, an effective mass acceptor ionization

energy in GaN is estimated to be 85 ± 8 meV and Be is proposed to be the most shallow group II acceptor. The thermal binding energies in the effective mass limit has also been predicted by McGill and colleagues [47] to be ~100 to 125 meV using a modified bound polaron model. For column I elements, however, rather high activation energies are calculated. For the amphoteric column IV elements, lengthy theoretical calculations are necessary to estimate their energy levels, and these values are often plagued by large errors. As can be seen from Table 9.4, the energy levels calculated for C vary from shallow acceptor values to deep levels by using different theoretical methods [205–209].

Because the nearest neighbors are the same for cubic and hexagonal crystals, only minor changes will be expected for solubility and incorporation in both polytypes. However, due to the higher symmetry of the cubic crystals, the activation energies of the "shallow" acceptors shall be lower than in the case of hexagonal group III-nitrides.

9.5.2 Doping of Cubic GaN by Mg

Mg-doped cubic GaN films are grown on semi-insulating GaAs (001) substrates by RF-plasma-assisted MBE at a substrate temperature of 720 °C. For Mg doping, a commercially available effusion cell with an orifice of 3 mm is used. It contains solid Mg and the cell temperature is varied between 300 °C and 450 °C. The beam equivalent pressures (BEP) of the incident Ga-flux and of the Mg-flux at the higher cell temperatures are measured by a moveable ion gauge. The pressures are corrected for different ionization efficient factors of the elements using $\eta = (0.4Z/14) + 0.6$, where Z is the atomic number of the considered atom or molecule [210]. For low cell temperatures of the Mg source, the BEP is too low for direct measurement. In this case, the BEP is estimated by extrapolation according to the vapor pressure curve of Mg [211]. The thickness of the GaN layers is determined by SEM and optical reflectivity measurements and varied between 0.7 μm and 1.3 μm.

9.5.2.1 Incorporation of the Mg acceptor

The concentration and depth distribution of Mg is determined by SIMS using a RIBER/CAMECA MIQ56A equipment. A primary beam of 6 keV O_2^+ ions with a spot diameter of 6 μm and a current of 2×10^{-8} A is rastered over an area of $250 \times 250\,\mu m^2$. Positive secondary ions from a central region of $180 \times 180\,\mu m^2$ are analyzed by means of quadruple mass spectrometry (QMS). For quantification, the ratio of the SIMS intensities Mg^+/Ga^+ and the relative sensitivity factor known from a Mg-implanted GaN reference sample are used.

The depth profile of Mg into c-GaN is depicted in Figure 9.32, where the SIMS intensities of Mg, Ga, N, and GaAs are plotted versus depth for a

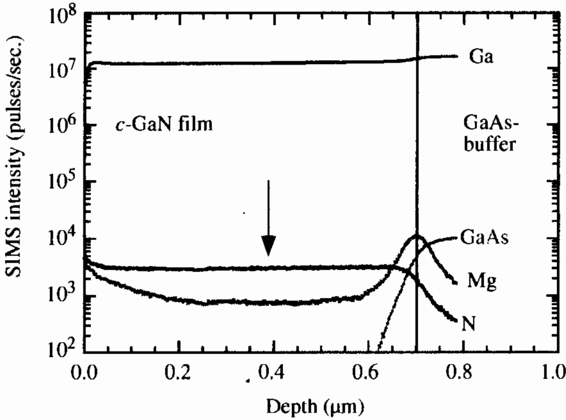

Figure 9.32 SIMS depth profiles of Mg, N, Ga, and GaAs in a 0.7-μm-thick Mg-doped cubic GaN epilayer grown on GaAs substrate by RF-plasma-assisted MBE (Mg-flux $4.4 \times 10^{14}\,\text{cm}^{-2}\,\text{s}^{-1}$, $T_{Mg} = 400\,°\text{C}$).

0.7-μm-thick GaN sample. Similar depth profiles are observed for all other Mg-doped samples. Whereas the N and Ga concentrations are uniformly distributed over the epilayer, the Mg signal shows two characteristic features at the surface and at the *c*-GaN/GaAs interface. At the surface a slight increase of the Mg signal occurs, which may be a hint for segregation of Mg. In the depth from 0.2 μm to 0.6 μm, a homogeneous Mg-distribution is measured. Within this uniformly doped region, the SIMS calibration is performed, resulting in an Mg concentration of $5 \times 10^{18}\,\text{cm}^{-3}$. At the *c*-GaN/GaAs heterojunction, a characteristic accumulation of the Mg atoms by more than one order of magnitude is observed. This effect is attributed to an increased diffusion of Mg to the GaAs substrate, similar to the observations made by Ya Ber and colleagues [212] for *h*-GaN on sapphire substrates. Due to the low operating temperature of the Mg cell, it is not very likely that transient effects of the Mg flux just after opening of the shutter will result in this increased incorporation. However, the high density of structural defects near the interface due to the large mismatch between substrate and epilayer may cause such an accumulation. A significant amount of Mg $\sim 5 \times 10^{17}\,\text{cm}^{-3}$ is also found in a nominally undoped GaN sample grown after Mg-doping experiments. This is due to the memory effect of the growth chamber.

Figure 9.33 shows the incorporated Mg measured by SIMS as a function of the beam equivalent pressure of Mg (squares) for cubic GaN grown at 720 °C. The dashed line (with slope $k = 1$) corresponds to an Mg sticking coefficient of about 1. The full line shows that the built-in Mg concentration remains below about $5 \times 10^{18}\,\text{cm}^{-3}$and is nearly independent on the arrival rate of supplied Mg, which varied by four orders of magnitude. This behavior

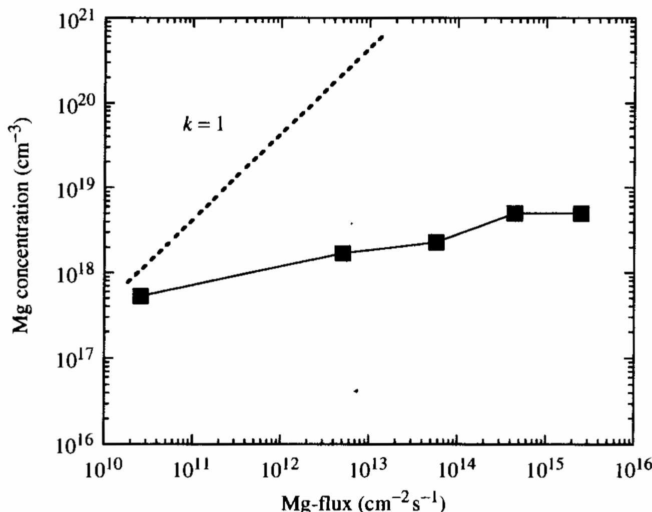

Figure 9.33 Mg concentration measured by SIMS (squares) versus Mg-flux of the arriving Mg atoms for cubic GaN epilayers. The dashed line with slope $k = 1$ corresponds to an incorporation of Mg that is directly proportional to the Mg arriving rate.

is similar to that observed for MBE growth of hexagonal GaN [213] and GaAs [214] and is expected due to the high vapor pressure of Mg. Therefore, the Mg incorporation occurs either via the presence of a saturated surface layer of Mg or via the presence of specific configurational sites for Mg incorporation, so that the incorporation is nearly independent of the Mg arrival rate [213].

9.5.2.2 Optical properties of the Mg acceptor

The 2 K photoluminescence spectra of cubic GaN epilayers grown at a substrate temperature of 720 °C, which are doped by Mg with different Mg fluxes are shown in Figure 9.34. The lowest spectrum is that of an undoped reference sample grown before introducing Mg into the chamber. Mg-doping at fluxes below 10^{13} cm^{-2} s^{-1}(Mg-source temperatures T_{Mg} below 300 °C) results in the appearence of a donor acceptor transition (D^0, A^0_{Mg}) at 3.04 eV. The donor participating in this line has the same ionization energy as the one observed in the undoped sample. From the emission line energy an acceptor activation energy of $E_{\mathrm{Mg}} = 0.229$ eV is estimated. This energy level is in excellent agreement with recent theoretical calculations of $\mathrm{Mg_{Ga}}$ for *c*-GaN [215] and is somewhat lower than that for the corresponding value of 0.265 eV for *h*-GaN [216]. At Mg-fluxes exceeding 10^{14} cm^{-2} s^{-1} (T_{Mg} higher than 350 °C), the low energy side of the spectrum is dominated by a broad blue-emission band centered at about 2.85 eV, which is modulated due to interference of the PL light (upper curves in Figure 9.34). The nature of this

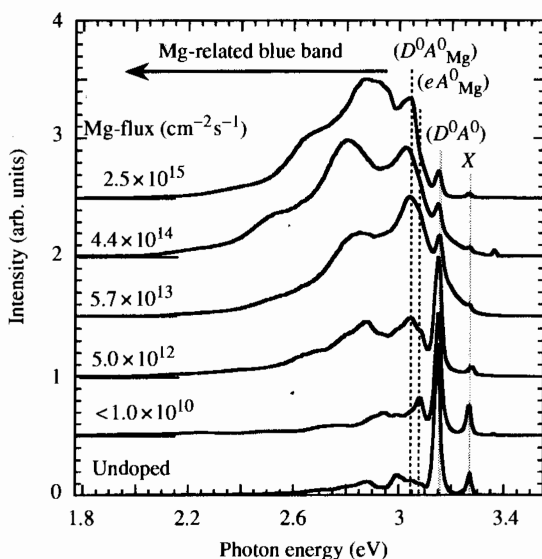

Figure 9.34 Low-temperature (2 K) PL-spectra of Mg-doped cubic GaN epilayers grown with different Mg-fluxes. The lowest spectrum corresponds to an undoped cubic GaN sample grown before introducing Mg into the MBE growth chamber (excitonic transition X at 3.26 eV and omnipresent donor–acceptor pair transition (D^0A^0)). The dashed lines indicate the shallow Mg-related transitions (eA^0_{Mg}), $(D^0A^0_{Mg})$. Below 2.95 eV the dashed arrow indicates the deep Mg-related blue transition band, which is modulated due to interference fringes of the PL light.

transition is currently unknown, however, it indicates that also in c-GaN, Mg is incorporated at different lattice sites or forms complexes at high Mg-fluxes. In h-GaN this blue band is attribute to Mg–V_N complexes [217].

PL-spectra at temperatures between 2 K and 300 K are plotted in Figure 9.35 for the c-GaN sample doped by an Mg-flux of $5\times10^{12}\,cm^{-2}\,s^{-1}$. Besides the excitonic transition X and the omnipresent (D^0A^0) transition at least four additional lines labled $(e, A^0)_{Mg}$, $(D^0A^0)_{Mg}$, $(D^0A^0)^*_{Mg}$ and $(D^0A^0)^{**}_{Mg}$ can be observed. One clearly sees the thermalization of both the (D^0A^0) as well as the shallow $(D^0A^0)_{Mg}$ transitions, involving the same residual donor. The photon energy as a function of temperature is shown in Figure 9.36 for the different emission lines. The temperature dependence of all Mg-related lines ($(e, A^0)_{Mg}$, $(D^0A^0)_{Mg}$, $(D^0A^0)^*_{Mg}$, and $(D^0A^0)^{**}_{Mg}$) clearly follow the temperature dependence of the energy gap of c-GaN, which is plotted as a full curve. Besides the omnipresent shallow donor ($E_D = 0.028\,eV$) and shallow acceptor ($E_A = 0.129\,eV$) two additional Mg-related defect levels—one acting as an acceptor and the other acting as a deep donors—are necessary to explain all additionaly observed transitions. Due to the two different donors and two different acceptors four different

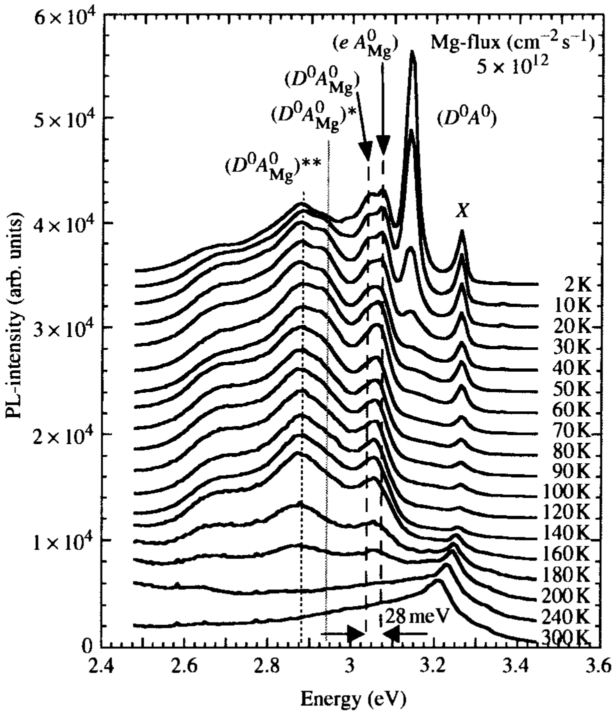

Figure 9.35 Temperature dependence of the PL-spectra of a cubic GaN:Mg epilayer (Mg-flux: $5 \times 10^{12}\,\mathrm{cm}^{-2}\,\mathrm{s}^{-1}$). Besides the omnipresent excitonic transition X and (D^0A^0), four additional Mg-related transitions labeled as (e, A^0_{Mg}), $(D^0A^0_{\mathrm{Mg}})$, $(D^0A^0_{\mathrm{Mg}})^*$, and $(D^0A^0_{\mathrm{Mg}})^{**}$ can be clearly seen. The dashed lines correspond to the shallow Mg-acceptor-related emission lines.

recombination paths are possible and observed in the low-temperature PL-spectrum ((D^0A^0), $(D^0A^0)_{\mathrm{Mg}}$, $(D^0A^0)^*_{\mathrm{Mg}}$, and $(D^0A^0)^{**}_{\mathrm{Mg}}$). The binding energies of the shallow Mg-related acceptor and the deep Mg-related are 0.229 eV and 0.239 eV, respectively. A scematic energy diagram of various recombination paths is shown in the inset of Figure 9.36.

9.5.2.3 Electrical properties of the Mg acceptor

Hall effect measurements of Mg-doped cubic GaN epilayers reveal that the layers are *p*-type without postgrowth treatments. For the sample doped with a Mg-flux of $10^{13}\,\mathrm{cm}^{-2}\,\mathrm{s}^{-1}$($[\mathrm{Mg}]_{SIMS} = 1.7 \times 10^{18}\,\mathrm{cm}^{-3}$) the measured free hole concentration p_{Hall} and hole mobility at room temperature are about $3 \times 10^{16}\,\mathrm{cm}^{-3}$ and $215\,\mathrm{cm}^2/\mathrm{Vs}$, respectively. The low activity of the acceptor is due to the high ionization energy of Mg. Figure 9.37 shows the temperature dependence of the hole concentration and of the hole mobility (inset). Under the assumption of compensation, for the shallow Mg acceptor

Figure 9.36 Temperature shift of the c-GaN near-band-edge (X, (eA^0), (D^0A^0)) and Mg-related ($(e, A^0)_{Mg}$, $(D^0A^0)_{Mg}$, $(D^0A^0)^*_{Mg}$, $(D^0A^0)^{**}_{Mg}$) PL-lines (full squares). The solid curve is the variation of the gap energy after Ramirez-Flores [45]. The dashed curves are calculated for free to bound $(e, A^0)_{Mg}$, $(D^0A^0)_{Mg}$ using a donor and Mg-acceptor energy of 28 and 229 meV, respectively. For the deep Mg-related donor, an energy of $E_D{}^{Mg} = 239$ meV is estimated. A schematic energy level diagram with all observed transitions is shown in the inset.

the temperature dependence yields an activation energy of $E_{Mg} = 0.110 \pm 0.020$ eV [22]. The corresponding value for hexagonal GaN is 160 ± 5 meV [100]. In both cases, the thermal activation energies are much lower than the optical activation energies, which may be due to a strong relaxation effect of the negatively charged Mg, as has been shown in recent theoretical calculations [218].

With increasing Mg flux, no increase of the free hole concentration p_{Hall} is observed at room temperature (see Figure 9.38). On the contrary, the free hole concentration is even slightly decreasing with increasing Mg flux. SIMS measurements, however, show that the amount of incorporated Mg has increased, indicating that an additional Mg-related compensating donor may be incorporated during Mg doping. This assumption is corroborated by PL-measurements. The integral intensities of the shallow transitions (D^0, A^0_{Mg}) and (e, A^0_{Mg}) as well as the deep "blue" band show a clear

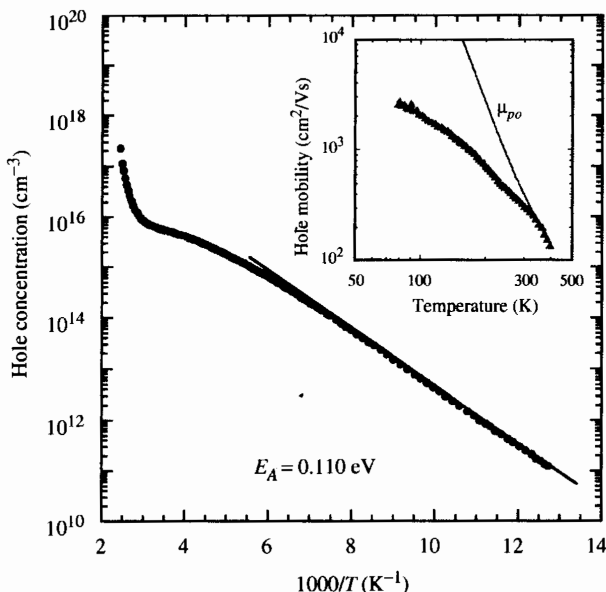

Figure 9.37 Hole concentration of an Mg-doped cubic GaN epilayer (Mg-flux $5.7 \times 10^{13}\,\text{cm}^{-2}\,\text{s}^{-1}$, $T_{Mg} = 350\,°\text{C}$) as a fuction of the inverse temperature $1000/T$. The estimated shallow acceptor level is $E_{Mg} = 0.110 \pm 0.020\,\text{eV}$. The inset shows the temperature dependence of the hole mobility, which is dominated by polar optical phonon scattering at temperatures above 300 K (full line).

increase with increasing Mg-flux. Therefore, all three transitions are related to the incorporation of Mg in *c*-GaN. However, whereas the shallow transitions seem to saturate at higher Mg-flux, such is not the case for the blue emission. Because the free hole concentration is nearly independent of the Mg amount, it is concluded that the impurity involved in the blue band may act as a compensating deep donor center. This observation is in agreement with the previously presented PL-measurements, where the presence of a deep Mg-related donor level to explain the different emission lines is assumed, and is also in agreement with similar observations made in *h*-GaN [219]. Theoretical calculations showed that Mg_i, Mg_N, or Mg–V_N acts as a compensating deep donor in GaN. Because the formation energies of all these Mg-related defects are low, they are possible candidates for the impurity involved in blue band in GaN [215].

In conclusion, *p*-type doping of *c*-GaN by Mg suffers on self-compensation, segregation, and solubility, effects which limit the room temperature hole concentration to the low $10^{17}\,\text{cm}^{-3}$ range. *p*-type doping by Mg under N-rich growth conditons, which has been shown to be benefitable in Mg-doping of hexagonal GaN, results in increased hexagonal

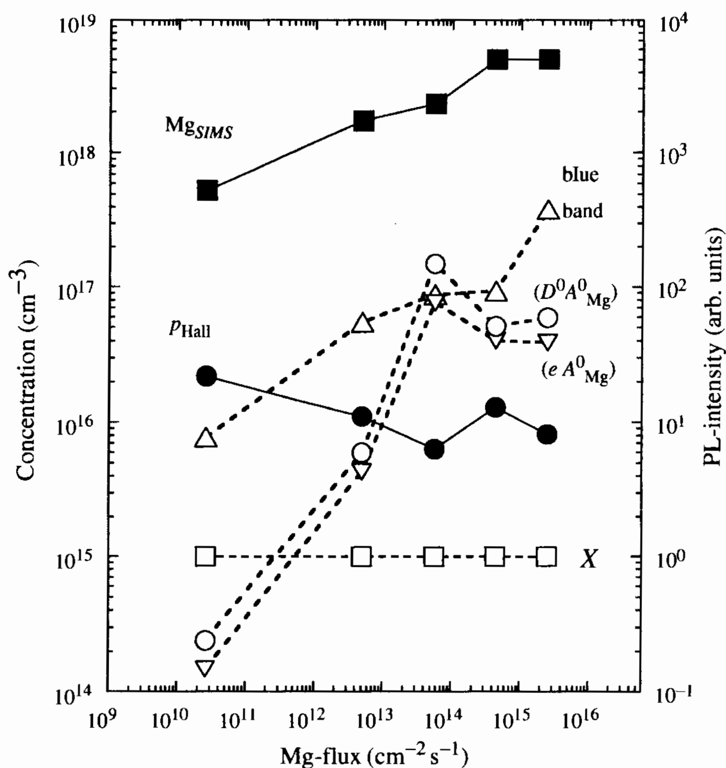

Figure 9.38 Integral PL intensities of various observed transitions, Mg concentration measured by SIMS, and free hole concentration p_{Hall} at room temperature versus Mg-flux.

inclusions. At a growth temperature of 720 °C, the amount of incorporated Mg is limited to about 5×10^{18} cm^{-3} due to the high volatility of Mg. SIMS measurements further show an accumulation of Mg at the GaN/GaAs interface and suggest the effect of Mg diffusion toward the GaAs substrate. In PL-measurements, an Mg-related shallow acceptor with an activation energy of 0.230 eV is observed at low Mg concentrations. Doping of *c*-GaN with Mg concentrations higher than 10^{18} cm^{-3} results in the appearance of an additional deeper transition band. This indicates that Mg is also built in at off-Ga sites or as complexes.

9.5.3 Alternative Acceptors

Due to the lack of doping experiments in cubic III-nitrides, only a few words can be said for alternative acceptors. There is still the question of whether acceptors with smaller binding energies exist, and whether they are suitable

dopants, which can be incorporated in high concentrations. As already mentioned in the theoretical aspects (Section 9.5.1), alternative acceptors are Be, Zn, and C.

In all other III-V semiconductors, Be is a more shallow acceptor than Mg, has less surface segregation, and generally is easier to handle in MBE systems than Mg. Despite these precautions, the results reported by Brandt [220] were quite disappointing. *p*-type doping was not observed for any of the cubic GaN epilayers, but rather *n*-type conductivity (even higher than the background of the undoped samples) or high resistivity. At Be concentrations above 10^{20} cm^{-3}, a transition to polycrystalline dentritic growth finally took place. This phenomenon is expected, because theoretical calculations [209] have shown that the solubility of Be in GaN is fairly low and exceeding it triggers the formation of Be_3N_2 precipitates. However, by using the method of codoping, where the acceptor Be and the donor O were simultaneously incorporated in the same amount into *c*-GaN, the formation of Be–O ion pairs should be energetically favorable and prevent the formation of Be_3N_2 precipitates [221]. O supplied from residual H_2O partial pressure in the MBE system immediately after having opened the system resulted in unintentional codoping of Be and O. In such codoped epilayers, free hole concentrations of about 1×10^{18} cm^{-3} and hole mobilities of about 150 cm^2/Vs are measured, without degradation of the structural properties and surface morphology of their films [220]. SIMS profile measurements showed that both Be and O were incorporated in almost equal amounts, namely about 5×10^{20} cm^{-3}. Therefore, this technique of codoping opens one way to reach high hole concentrations. However, it requires that the Be_{Ga}–O_N ion pairs occupy nearest-neighbors sites, which is true only if large amounts of both dopants are available and the surplus of Be determines the hole concentration. It is questionable if this allows controlled *p*-type doping over some orders of magnitude, as is necessary for many electrical devices, because no further reports on codoping of *c*-GaN exist.

Attempts to dope *h*-GaN *p*-type with Zn result in, at best, compensated high-resistivity material. In moderately Zn-doped material, a rather broad PL band appears at about 2.85 eV, the characteristic Zn-related emission [222–224]. This emission is assumed to be related to the substitutional Zn_{Ga} acceptor. A binding energy of about 0.34 eV is estimated from the position of the zero-phonon line [223]. Due to this large activation energy, thermal activation of the Zn acceptors results in a very low hole concentration at room temperature and makes Zn less useful for *p*-type doping. Nevertheless, in 1994, Nakamura and colleagues [225,226] used the deep level provided by Zn doping to minimize the amount of In required in the InGaN active region of an LED. Only a few percent In resulted in emission at the desired wavelength of 450 nm. For cubic group III-nitrides, no attempts to dope by Zn have been reported.

One of the potential replacements for Mg is C. At present, little information about the incorporation and behavior of C in the nitrides is known. In the hexagonal group III-nitrides AlN [227] and GaN [228] *p*-type doping have been obtained, although the carrier concentrations have been limited to 3×10^{18} cm^{-3} and 3×10^{17} cm^{-3}, respectively, even though the C concentrations in these films are reported to be significantly higher. C-doping from CCl_4 during metalorganic ECR-MBE at 700 °C has, in fact, been shown to produce *p*-type *h*-GaN at hole concentrations up to 3×10^{17} cm^{-3}. The hole mobility was determined to be 100 cm^2/Vs. Unfortunately, introduction of C via CCl_4 also introduces an unwanted parasitic etching problem due to the release of Cl at the growth surface. As a result, a rather severe tradeoff of *p*-type doping level at the expense of growth rate is observed.

By analogy with results obtained in GaAs, it is expected that CBr_4 should produce higher acceptor concentrations with less etching due to its higher deposition efficiency and the reduced volatility of the Br-containing etch byproducts [229]. As yet, however, *p*-type GaN has not been obtained using CBr_4.

Using a resistively heated graphite filament as a C source in RF-plasma-assisted MBE [230], *h*-GaN was doped with C of nominal concentrations ranging from 10^{16} cm^{-3} to 10^{20} cm^{-3}. The incorporation of C led to a reduction of the background electron concentration by one order of magnitude, but the material remained *n*-type. For high C concentrations, a re-increase of the carrier concentration was observed, which was related to self-compensation. Therefore, the role of C is controversal. Due to the amphoteric nature of C, it can be incorporated on a Ga site as a donor and on an N site as an acceptor. Although the formation energy of C_{Ga} is much larger than that of C_N, indicating a preference of C to be an acceptor, at higher C concentration the formation of nearest neighbor donor–acceptor pairs C_{Ga}^{+}–C_{N}^{-} is favored energetically [206], resulting in self-compensation. Therefore, it is unlikely that the maximum hole concentrations seen in GaAs ($p \cong 10^{20}$ cm^{-3}) [231] can be achieved in GaN. In addition, due to the weak In–C bond, it is expected that C acts as a donor in InN [102]. Therefore, the role of C as an acceptor needs further investigation, especially for the cubic phase, where to date no data are available.

9.6 *n*-TYPE DOPING OF CUBIC GaN

9.6.1 Theoretical Aspects of Different Donors

For *n*-type doping of GaN (or the other group III-nitrides), elements of the group IV on group III-site and the group VI on the N-site can be incorporated as donors. The group-IV impurities include C, Si, Ge, Sn, and Pb. The latter element has a large atomic radius and is therefore not expected to incorporate

easily in III-nitride semiconductors. The remaining group IV impurities, that is, C, Si, Ge, and Sn, share different charcteristics. First, all column IV impurities are amphoteric, that is, they can occupy either the group III or the N site of the zincblende crystal. As a result, group IV impurities are donors or acceptors for the cation site or anion site, respectively. Second, due to their amphoteric nature, column IV impurities may autocompensate and the electrical activity may saturate at a high impurity concentration. As discussed previously, however, only C has a comparable small size to the N-atom and is therefore expected to be incorporated as an acceptor. Si, Ge, and Sn are expected to replace a Ga-atom and therefore act as donors. The group IV impurities include O, S, Se, and Te. Considering the atomic radius, only O fits to the N-atom and is believed to be incorporated easily. Due to the high vapor pressure of S and the agressivity of S to copper, the introduction S is unwanted in the MBE growth chamber and is therefore avoided as much as possible. From these considerations, Si, Ge, O, and Se are the most appropriate elements for *n*-type doping experiments in GaN.

9.6.2 Doping of Cubic GaN by Si

Silicon is the prefered *n*-type dopant in the growth of GaN. In hexagonal GaN, controllable Si-doping has been demonstrated for concentrations form 10^{17} cm^{-3} to 10^{19} cm^{-3} [232]. At 300 K, the luminescence intensity and the linewidth of the band-to-band transition increases monotonically with doping concentration [233,234]. Photoreflectance measurements further showed for heavily doped *h*-GaN a shrinkage of the energy gap due to bandgap renormalization (BGR) effects [235]. Detailed analysis of the electrical properties of Si-doped *h*-GaN further showed a significant influence of crystal defects [236] and of dislocations on the electron mobility [237,238].

In the following, recent doping experiments of cubic GaN epilayers by Si are summarized. The Si-doped cubic GaN epilayers are grown by RF-plasma-assisted MBE on semi-insulation GaAs (001) substrates at a substrate temperature of 720 °C [9]. The growth rate is about 0.07 μm/hr and the thickness of the layers is about 0.8 μm. Elemental Si is evaporated from a commercial effusion cell at source temperatures between 750 °C and 1100 °C, which corresponds to a variation of the Si-flux between 8.5×10^5 cm^{-2} s^{-1} and 5.2×10^{11} cm^{-2} s^{-1}, respectively.

9.6.2.1 Incorporation of the Si donor

The incorporation of Si into *c*-GaN has been studied by SIMS. The concentration and depth distribution of Si is measured using Si-implanted calibrated standards for quantification, and an O^{2+} primary beam of 6 keV. In Figure 9.39 the depth profiles of Si, GaN, and As are depicted for a cubic GaN epilayer doped with elemental Si at an Si source temperature

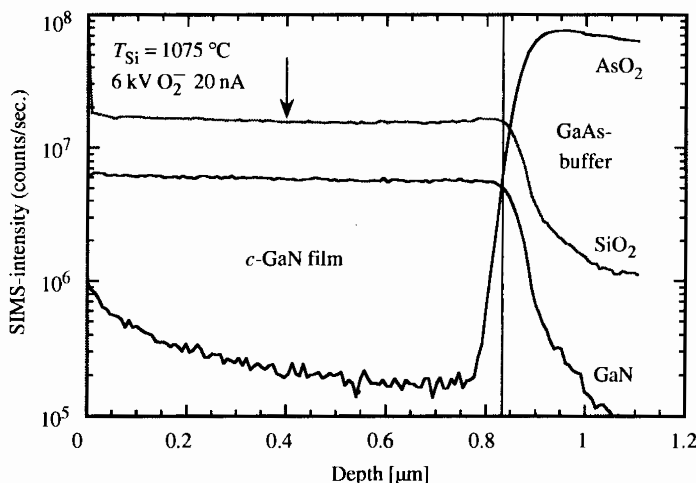

Figure 9.39 SIMS depth profiles of an Si-doped cubic GaN epilayer.

of $T_{Si} = 1075\,°C$. An homogeneous Si distribution is measured throughout the whole *c*-GaN epilayer and no accumulation either at the interface or at the surface is observed. The Si-concentration measured at a depth of about 0.4 μm (indicated by the arrow in Figure 9.39) is $2 \times 10^{19}\,cm^{-3}$. In Figure 9.40 the Si-concentration measured by SIMS (full squares) and the free electron concentration measured by Hall effect at room temperature (full triangles) are plotted versus the Si source temperature. As can be clearly seen, both the free electron concentration and the amount of incorporated Si exactly follow the Si-vapor pressure curve (full line in Figure 9.40) at $T_{Si} > 1000\,°C$ [239]. This indicates that nearly all Si atoms are incorporated at Ga sites and act as shallow donors. At room temperature the maximum free electron concentration reached thus far is about $5 \times 10^{19}\,cm^{-3}$. This clearly demonstrates the ability of controlled *n*-type doping of cubic GaN by Si up to concentrations which are necessary for the fabrications of LDs.

9.6.2.2 Optical properties of Si-doped cubic GaN

PL measurements are performed at 300 K and in an He bath cryostate at 2 K. The luminescence was excited by a cw HeCd UV laser with a power of 3 mW and measured in a standard PL system. At room temperature the total intensity of the luminescence (full dots in Figure 9.40) also follows the Si-vapor pressure curve, indicating that at 300 K the optical properties are also determined by the Si-doping and that even at the highest free carrier concentration of $5 \times 10^{19}\,cm^{-3}$, no quenching of the

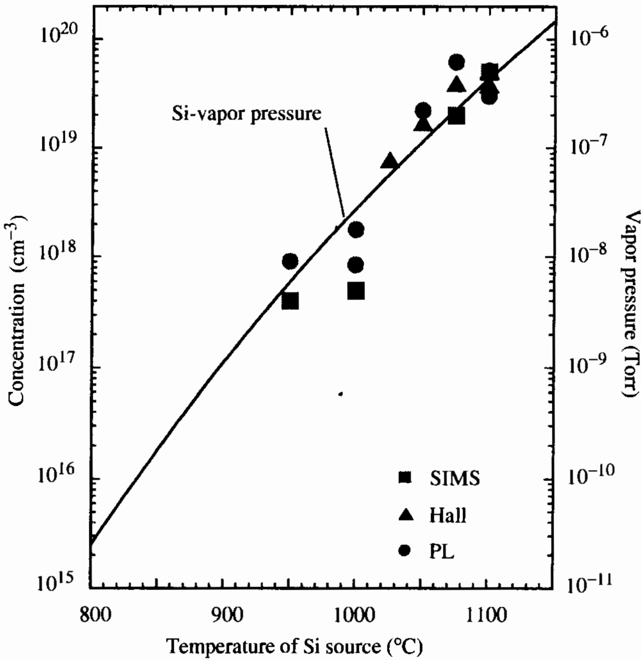

Figure 9.40 Si concentration measured by SIMS (full squares), free electron concentration measured by Hall effect (full triangles), and integrated PL intensity (full circles) at 300 K versus Si source temperature. The full line represents the vapor pressure curve of Si [239].

luminescence is observed. The optical properties of Si-doped cubic GaN at low temperature are shown in Figure 9.41. At 2 K the spectrum of the sample grown with the lowest Si-flux ($8.5 \times 10^5\,\mathrm{cm}^{-2}\,\mathrm{s}^{-1}$, $T_{\mathrm{Si}} = 750\,°\mathrm{C}$) is dominated by the excitonic transition X at 3.26 eV and the donor–acceptor pair transition (D^0A^0) at 3.15 eV [10]. With increasing Si-flux, a clear shift to higher energies of the (D^0A^0) is observed. In contrast, the transition X remains in position as expected for an excitonic line. The peak position of the (D^0A^0) as a function of the Si-concentration is plotted in Figure 9.42, where the Si concentration, N_{Si}, is calculated by dividing the measured Si-fluxes by the measured growth rates. Using a simple Coulomb-term model [240], the peak position of the (D^0A^0) transition can be calculated by:

$$E_{(D^0,A^0)} = E_{gap} - (E_D + E_A) + \frac{e^2}{4\pi\varepsilon_0\varepsilon R} \quad \text{with } R = \frac{1}{2}\cdot\frac{1}{\sqrt[3]{N_{\mathrm{Si}}}}$$

The full line in Figure 9.42 represents the model prediction and shows an excellent agreement with the experimental data (full dots).

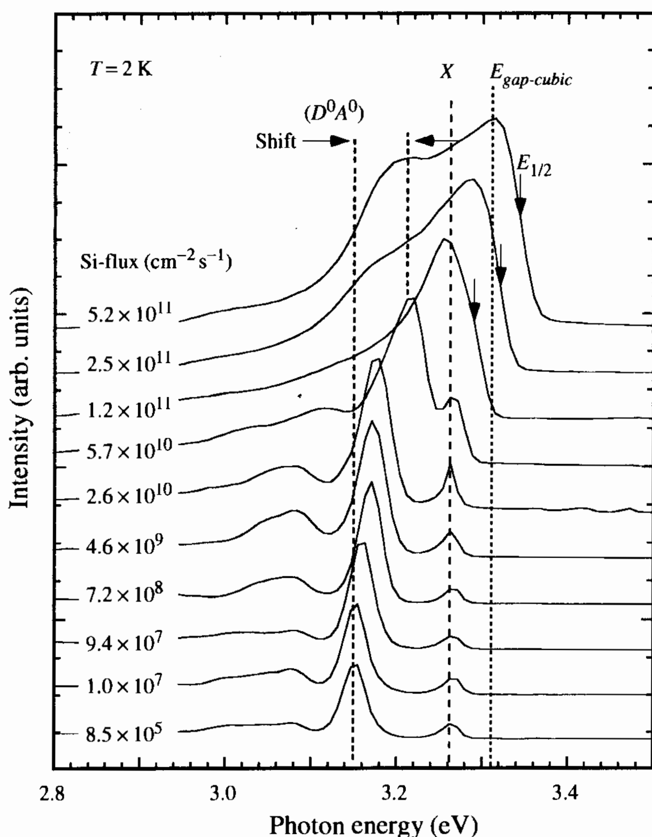

Figure 9.41 Low-temperature PL spectra of Si-doped cubic GaN at different Si-fluxes.

Beyond an Si-flux $>1.2 \times 10^{11}$ cm^{-2} s^{-1} ($T_{Si} > 1025$ °C), both luminescence lines merge to one broad band and the peak maximum shifts monotonically toward higher energies with increasing Si-doping. Simultaneously, the spectral shape of the main emission line becomes strongly asymmetric having a steep slope on the high-energy side and a smooth slope on the low energy side of the spectra. Such behavior is characteristic for momentum nonconserving (nonvertical) band-to-band transitions or to recombination of free electrons to local hole states [241] and has been observed in the spectra of GaAs heavily doped with Te [241] or Si [242]. The position at the steep high-energy edge of the luminescence band is determined by the electron Fermi-level and it should shift to higher energies (Burstein-Moss shift [243]) as the conduction band fills with free electrons. In Figure 9.41 the position of half maximum, $E_{1/2}$, is indicated by arrows. In the highest doped sample, $E_{1/2}$, has a value of 3.342 eV. For a corresponding carrier concentration of

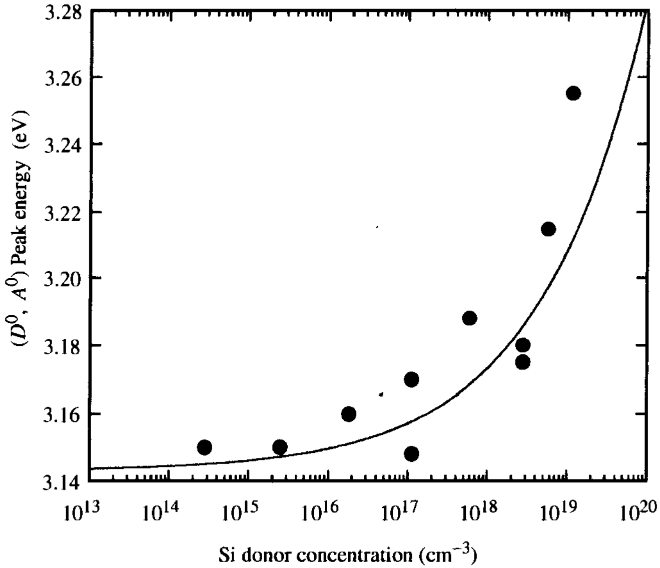

Figure 9.42 Peak energy of the (D^0, A^0) band versus Si donor concentration at 2 K. The full line was calculated by using a simple Coulomb-term model.

about $5 \times 10^{19}\,cm^{-3}$, however, band-filling of 240 meV is calculated using an electron effective mass of 0.2 in GaN [244]. This indicates that, due to exchange interaction between free carriers, the energy gap of cubic GaN has been shrunk from 3.305 eV without doping to 3.095 eV at an electron concentration of $5 \times 10^{19}\,cm^{-3}$. As it is known for GaAs, the reduction in band-gap energy due to the so-called BGR can be described by a $n^{1/3}$ power law [245]. From this we obtain a BGR coefficient of -5.7×10^{-8} eV cm for cubic GaN, which is comparable to that observed in hexagonal GaN (-4.7×10^{-8} eV cm) [246].

9.6.2.3 Electrical properties of the Si donor

Hall effect measurements are performed using square-shaped samples at 300 K and a magnetic field of 0.3 T with the samples in the dark. In is used for Ohmic contacts.

In Figure 9.43 the value $1/q \cdot |R_H|$ is plotted as a function of the Si source temperature between 700 °C and 1150 °C; R_H is the Hall constant and q is the electronic charge. One clearly sees that for $T_{Si} \leq 1025$ °C, all samples are p-type with a hole concentration of about $2 \times 10^{16}\,cm^{-3}$, which is nearly independent of the Si source temperature (open squares). Above $T_{Si} \geq 1025$ °C, the samples are n-type (full triangles) and, as already discussed in Figure 9.40, the measured free electron concentration

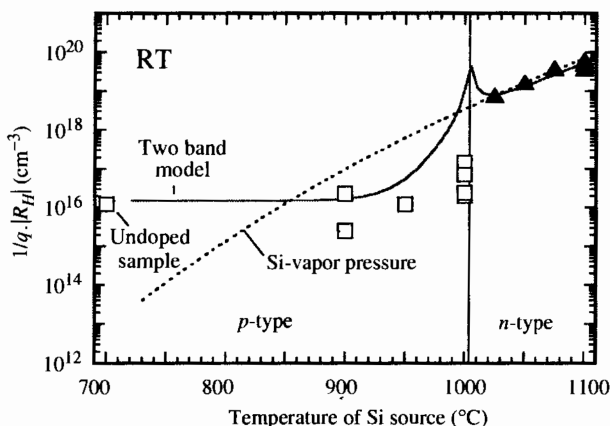

Figure 9.43 $1/q \cdot |R_H|$ versus Si source temperature measured at room temperature. The c-GaN layers were n-type above 1000 °C and p-type below 1000 °C.

exactly follows the Si-vapor pressure curve (dotted line). Temperature-dependent Hall effect measurements further show that these cubic GaN samples are totally degenerated. From this p-type to n-type transition at about 1025 °C, it is concluded that a residual acceptor concentration of about $N_A = 4 \times 10^{18}\,\text{cm}^{-3}$ exists in the cubic GaN epilayers, and that the Si-donor has to compensate these residual acceptors. This value can be extrapolated from the dotted line (Si-vapor pressure curve) at 1025 °C.

For a nominally undoped c-GaN sample, a hole concentration of about $p = 1 \times 10^{16}\,\text{cm}^{-3}$ and a hole mobility of $\mu_p = 283\,\text{cm}^2/\text{Vs}$ are measured at room temperature. This value is also included in Figure 9.43 (open square at the outmost left side). Temperature-dependent Hall effect measurements of this sample further show that the involved acceptor has an activation energy of about $E_A \cong 0.166\,\text{eV}$ [247]. Due to the depth of this acceptor level, only a few percent of the acceptors are thermally activated at room temperature and contribute to the measured hole concentration. The estimated acceptor concentration of the nominally undoped sample is therefore $4 \times 10^{18}\,\text{cm}^{-3}$. This is exactly the same value that we obtain from the Si-doping previous experiments. Assuming a constant residual acceptor concentration and taking the room temperature values of the undoped samples for p and μ_p, a simple two-band conduction model [248] can be applied to calculate $1/q \cdot |R_H|$ as a function T_{Si}. For the free electron concentrations, n, we use the Si-concentrations estimated from the Si-vapor curve (dotted curve in Figure 9.43) and for the electron mobilities, μ_n, we extrapolate the μ_n values measured at high T_{Si}, taking into account the increase of mobility with increasing free carrier

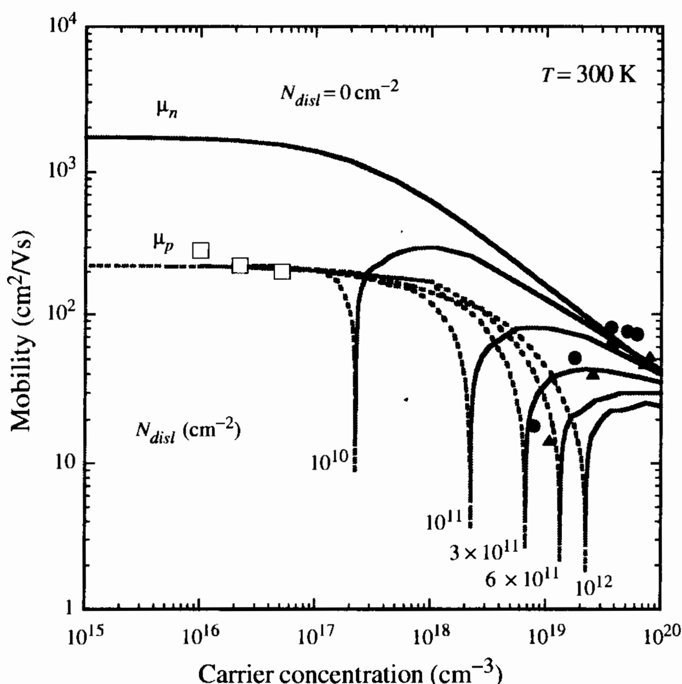

Figure 9.44 300 K mobility versus free carrier concentrations of Si-doped *c*-GaN.

concentration due to dislocation scattering. The two-band model results are shown in Figure 9.43 by the full curve and explain in a reasonable way the experimental observation.

Figure 9.44 shows the mobilities (μ_n, μ_p) of the Si-doped *c*-GaN epilayers versus the measured free carrier concentration (n, p) at room temperature. The full dots and the full triangles are samples of different series showing *n*-type conductivity ($T_{\text{Si}} \geq 1025\,°\text{C}$). The open square is the nominally undoped *p*-type reference sample. The influence of the high dislocation density ($\approx 10^{11}$ cm^{-2}) on the electrical properties of *c*-GaN is reflected in the dependence of the electron mobility on the free carrier concentration. Similar to *h*-GaN [237], the mobility first increases with carrier concentration, reaches a maximum value of about 82 cm^2/Vs at an electron concentration of 3×10^{19} cm^{-3}, and decreases again. This behavior is characteristic for dislocation scattering and shows that in cubic GaN, threading-edge dislocations are electrically active. Recently, a theory of charged-dislocation line scattering has been developed and applied to *h*-GaN [238]. Look and Sizelove [238] showed that dislocations may well be charged and should have acceptor nature.

X-ray measurements and RBS experiments on cubic GaN layers showed that the dislocation density N_{disl} is in the order of 3×10^{11} cm^{-2} for 0.7-μm-thick epilayers and that N_{disl} decreases with increasing epilayer thickness [127,249]. Following Weimann and colleagues [237] and multiplying N_{disl} with the lattice constant of c-GaN ($a_{cub} = 0.452$ nm), a residual acceptor concentration of about 6×10^{18} cm^{-3} is estimated. This value agrees within experimental error with the acceptor concentration that is necessary to explain the p-type to n-type transition.

The curves in Figure 9.44 represent calculations of the room temperature mobility versus carrier concentration for different electrically active dislocation densities. In this calculation, contributions of polar optical phonon scattering, acoustic phonon scattering, ionized impurity scattering, and dislocation scattering have been taken into account. In addition, changes of the compensation ratio $\Theta = N_D^0/N_A^0$ in n-type samples ($\Theta = N_A^0/N_D^0$ in p-type) if the incorporated donor concentration varies and that dislocation scattering is active only in n-type epilayers (in p-type GaN less than 1 percent of the acceptors are ionized at 300 K) have been included. The full lines are for n-type and the doted lines for p-type conduction. One can clearly see that the best agreement with experimental results is given for a dislocation density of about 3×10^{11} cm^{-2}. Thus, it is believed that in cubic GaN, threading-edge dislocations are charged and act as compensating acceptors. This residual acceptor concentration has to be surplused by the incorporated Si-donors to obtain n-type conductivity in c-GaN. For advanced electrical and optical devices based on cubic group III-nitrides, it will therefore be necessary to significantly reduce the dislocation density. Si, however, is also a suitable dopant for controlled n-type doping in the cubic GaN epilayers.

9.6.3 Alternative Donors

For h-GaN Nakamura and co-authors [250] and Zhang and colleagues [251] reported properties of Ge-doped GaN grown by MOVPE. A linear increase of the electron concentration as a function of the GeH_4 flow rate has been observed, with carrier concentrations in the range of 7×10^{16} to 10^{19} cm^{-3}. However, Ge incorporation is roughly an order of magnitude less efficient than Si, as judged by the larger GeH_4 flow rate required to obtain similar electron concentrations. To date, no reports have been published using Ge in an MBE system. Likewise, in cubic III-nitrides no such doping studies have been performed.

As previously mentioned, C is expected to be preferentially incorporated as an acceptor. The amphoteric nature of C, however, may also enable C to be incorporated as a donor, especially at high doping concentrations. In a recent MBE study of hexagonal GaN using a resistively heated graphite filament as a C source, it was shown that C could be incorporated up to concentrations

of 10^{20} cm^{-3} [230]. Investigations of the donor–acceptor pair luminescence further showed that at high C concentrations, a new donor exhibiting a thermal activation energy of about 55 meV was introduced. Whether this new donor is due to an incorporation of C on a Ga-site or to the formation of nearest neighbor C_{Ga}^{+}–C_{N}^{-} pair formation is currently unclear. However, due to the high *n*-type background concentration of $\geq 2 \times 10^{17}$ cm^{-3} and this newly introduced donor, no *p*-type conductivity was observed.

O is the only impurity which has been found present in a sufficient quantity to account for the carriers observed in unintentionally doped *h*-GaN and *c*-GaN. Therefore, the residual background doping, which was widely thought to be due to N vacancies, has also been attributed to O. Recent observations by Brandt [220] in *c*-GaN support that O may be one source for high *n*-type background doping. When growing *c*-GaN layers immediately after having opened the MBE system, electron concentrations up to 10^{21} cm^{-3} have been measured. These electron concentrations correlated well with the O concentration detected by SIMS (within 2 percent). Successively grown samples showed a monotonic decrease of the electron concentration, with the standard background (mid-10^{17} cm^{-3} range) being reached after about ten growth runs. This decrease was correlated with the decrease of the H_2O vapor in the MBE growth chamber as measured by QMS and implied that O, supplied from the residual H_2O vapor in the MBE system, was responsible for the high residual *n*-type doping. This method used to incorporate O via H_2O as a precurser is obviously impractical, however, it demonstrates that O is a good candidate for a shallow donor in III-nitrides. An suitable alternative for use in an MBE system was proposed by introducing O_2 into the system via a precision leak valve and dissociated by a plasma discharge.

Electron concentrations up to 6×10^{19} cm^{-3} have been achieved in Se-doped *h*-GaN MOCVD films [252–255], which were proportional to the H_2Se flow rate. However, the relatively low room temperature mobilities from 10 to 150 cm^2/Vs indicated a nearly constant compensation ratio of ≈ 0.4. The compensating acceptor was attributed to the Ga vacancy.

9.7 *p-n* HOMOJUNCTION OF CUBIC GaN

For the fabrication of any LEDs and LDs operating in the visible and UV with cubic III-nitrides, it is necessary to fabricate a *p-n* junction in this material. Blue-emitting GaN-based LDs are key components for laser printing, high-density optical memory, and next generation digital versatile disk (DVD) [1,8] and will enable the production of full-color displays and several further anticipated applications [2]. Currently, all commercial available GaN-based LEDs have hexagonal III-nitrides. A GaN device grown on conducting GaAs substrates, however, will enable easy device processing, which is compatible with the GaAs-based LED technology currently used

in industry, and therefore will significantly reduce production costs. In addition, cubic GaN can be grown on (001) substrates, eliminating the influence of PZ fields on the optical and electrical properties, which may have a stringent influence in hexagonal phase GaN-based LEDs. Recently, Yang and co-authors [5] reported the first electroluminescence of a cubic-phase GaN-LED grown on GaAs (001) substrates by MOCVD. However, the electrical data reported of their device showed values of the ideality factor larger than 20 and turn-on voltages larger than 6 V, which were neither compatible to a *p-n* junction nor to a Schottky diode. In addition, the emission of the device originated from an Mg-related deep recombination.

A cubic GaN *p-n* diode fabricated by Mg and Si doping of MBE-grown GaN on *n*-type GaAs (001) substrate has been reported by As and colleagues [6]. Current-voltage (I-V), capacitance-voltage (C-V), PL, and electroluminescence (EL) measurements were used to characterize the *c*-GaN *p-n* homojunction at room temperature. The cubic GaN *p-n* homojunction structure consists of a 760-nm-thick *p*-type GaN:Mg on top of a 500-nm-thick *n*-type GaN:Si. The *c*-GaN epilayers were grown by RF-plasma-assisted MBE at a substrate temperature of 720 °C. Te-doped *n*-type GaAs (001) with a free electron concentration of about 2×10^{18} cm^{-3} at room temperature was used as a substrate. Prior to the *c*-GaN epilayers, a nominally undoped low-temperature (600 °C) *c*-GaN buffer layer of 20 nm thickness was deposited. The nucleation process and the layer growth were carefully controlled using RHEED [9,113], as explained earlier. All our GaN layers were grown within the stoichiometric growth regime with a growth rate of about 0.07 μm/hr. Elemental Mg and Si were evaporated from commercial effusion cells at source temperatures of 350 °C, and 1100 °C, respectively. No annealing of the device for activation of the Mg acceptor was necessary for our MBE-grown samples.

The vertically structured diode was completed after evaporating electrodes on both the *n*-type GaAs substrate and the *p*-type top layer. Sn-contacts annealed at 400 °C for 15 min. in forming gas was used for the Ohmic contact to the *n*-GaAs-side. To form semitransparent contacts to the *p*-type *c*-GaN, a two-layer Au contact was thermally deposited. The first Au layer was about 100 Å thick with a lateral size of 0.8×0.5 mm^2. At one corner of this rectangular Au contact, a second circular-shaped Au layer with a diameter of 0.3 mm and a thickness of about 2000 Å was evaporated for easy bonding.

PL measurements were performed in an He bath cryostat at 2 K and at 300 K prior to contact formation. Luminescence was excited by the 325 nm line of a cw HeCd UV laser with a power of 3 mW and measured in a standard PL-system using photon counting. Figure 9.45 shows PL-spectra of the cubic GaN *p-n* structure prior to contact formation at room temperature and at 2 K. Due to the penetration depth of the HeCd laser ($\approx$200 nm), only the Mg-doped *p*-type *c*-GaN was investigated. At room temperature a

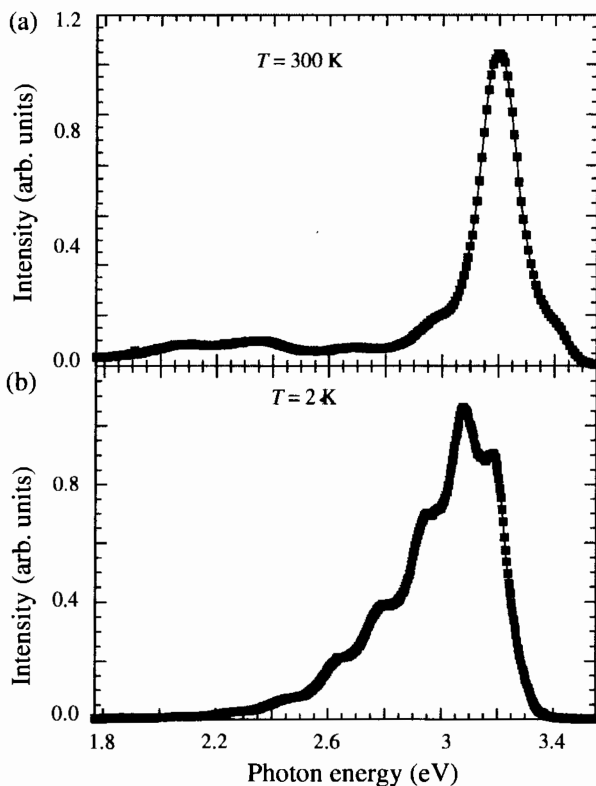

Figure 9.45 (a) Room-temperature PL-spectrum of a cubic GaN *p-n* junction grown by plasma-assisted MBE on GaAs (001) substrates. The spectrum was measured from the top surface (*p*-type layer) and was excited by a HeCd laser. (b) PL-spectrum of the cubic GaN *p-n* junction measured at 2 K.

dominant near-band emission with a peak energy at 3.2 eV was measured. The relative broad FWHM of 160 meV, compared with that of undoped *c*-GaN (FWHM ≅ 56 meV) [147] was due to the high Mg-doping. SIMS measurements of a *c*-GaN reference sample doped with the same Mg-flux of $5.7 \times 10^{13}\,\mathrm{cm^{-2}\,s^{-1}}$ ($T_{Mg} = 350\,°C$) had an incorporated Mg concentration of $2.3 \times 10^{18}\,\mathrm{cm^{-3}}$ [21]. At such high acceptor concentration, a superposition of the band-acceptor (eA^0) and band-to-band transitions and an interaction of the acceptors may occur, which broadens the PL lines. The shoulder in the PL-spectrum at 3.4 eV may result from transitions in a minor content of hexagonal phase GaN. As seen in the low-temperature spectrum in Figure 9.45b this "hexagonal" emission is totally suppressed at 2 K because all carriers are captured by the *c*-GaN, which has the lower bandgap. The low temperature spectrum was dominated by two transitions at 3.17 eV

and 3.07 eV, respectively. As reported earlier, temperature- and intensity-dependent measurements on nominally undoped [10] and Mg-doped samples [22] allowed the identification of both of these lines as (eA^0) transitions. The first involved an omnipresent yet unidentified shallow acceptor with a binding energy of 130 meV; the second involved the shallow Mg-related acceptor with a binding energy of 230 meV. At the low energy side of the (eA^0_{Mg}) band, the PL intensity decayed nearly exponentially with energy and was modulated due to interference fringes of the PL light. However, no dominant blue emission at 2.85 eV was observed. The blue band occurred if the Mg content was too high and recent investigations have shown that the defect involved in this transition acted as a compensating Mg-related donor [22,256,257]. Therefore, the low-temperature spectrum clearly demonstrated the high structural quality of the epilayer and successful suppression of the blue band-related defects.

In contrast to p-type doping of c-GaN with Mg, n-type doping of c-GaN with Si is straightforward. In a previous section we showed that the incorporation of Si follows exactly the vapor pressure curve of Si [257]. This allows in a very reproducable way, controlled n-type doping of c-GaN by Si up to a maximum free electron concentration of $5 \times 10^{19}\,\mathrm{cm}^{-3}$. By comparing the incorporated Si concentration measured by SIMS and the free electron concentration measured by Hall effect, it was demonstrated that all Si atoms act as shallow donors. Therefore, by doping at $T_{\mathrm{Si}} = 1100\,°\mathrm{C}$, the free electron concentration in the investigated cubic p-n structure was about $(4 \pm 1) \times 10^{19}\,\mathrm{cm}^{-3}$, forming an n^+-p step junction.

Due to the small conduction band offset between GaN and GaAs of 0.030 eV, a value that was measured by synchrotron-radiation photoemission spectroscopy of c-GaN/GaAs heterostructures [170]—and because both the n^+-GaN epilayer and the n-type GaAs:Te substrate ($n = 2 \times 10^{18}\,\mathrm{cm}^{-3}$) were degenerated—it was expected that this heterojunction behaves Ohmic-like. However, I-V measurements of the n-GaAs/n^+-GaN heterojunction (not presented here) showed a rectifying behavior with a small turn-on voltage of about 0.4 V, similar to that observed by Tanaka and colleagues [98] and Kribes and coworkers [258]. The latter group proposed that a thin, semi-insulating layer at the highly dislocated interface exists at the interface, which may be responsible for the nonlinear I-V curve [258]. This explanation is also plausible for the p-n devices grown on GaAs, where a thin ($\approx$20 nm), nominally undoped low-temperature GaN-buffer was inserted between the n-GaAs and the cubic n^+-GaN layer.

I-V and C-V characteristics were measured at 300 K. Electroluminescence (EL) under dc-biased conditions was collected through the semitransparent part of the p-type contact from the surface side of the device using the same equipment as for PL. Figure 9.46 shows the I-V characteristics of the whole structure measured at room temperature. The GaN

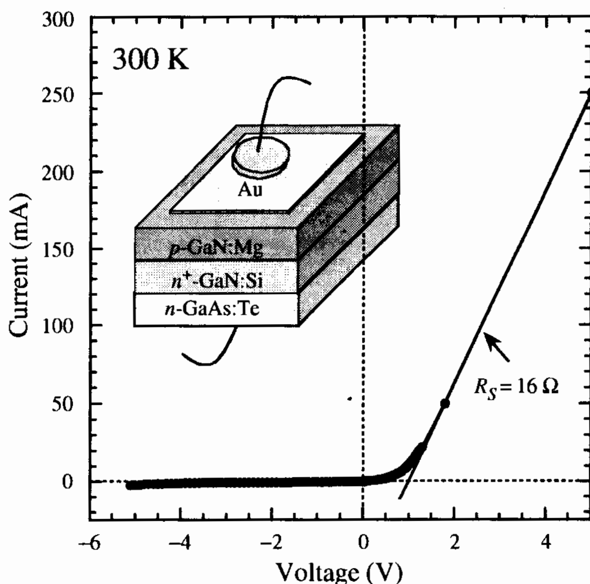

Figure 9.46 Current-voltage curve of the cubic GaN *p-n* junction. The inset shows a schematic drawing of the vertical structure of the device.

n^+-*p* diode forward turn-on voltage were approximately 1.2 V, which was about the same as that measured in hexagonal GaN *p-n* junctions (1.2 V) [259,260] and was much lower than that observed by Yang and colleagues [5]. For forward biases larger than 1.2 V, the current grew linearly with the applied voltage. A fit to the *I-V* curve yielded a series resistance of 16 Ω, which is comparable to that reported for commercial III-V nitride LEDs [226]. Because of its large bandgap (3.2 eV), the reverse bias saturation current due to minority carrier diffusion would be immeasureably small in an ideal GaN *p-n* diode. However, significant reverse bias leakage was observed in *c*-GaN diodes, indicating the presence of trap levels within the bandgap, which may act as a shunt or parallel conductance. At −5 V a dark current density of 0.25 A/cm^2 was measured. The large lattice-mismatch between the GaAs substrate and *c*-GaN, which leads to a dislocation density in the order of 10^{11} cm^{-2} [249], may also be responsible for the high dark current. Recently, a comparison of *p-n* diodes fabricated on lateral epitaxial overgrown (LEO) GaN demonstrated the influence of dislocations in hexagonal GaN and revealed a reduction of the reverse-bias leakage current by three orders of magnitude [260]. As shown by Werner [261], shunt and series resistances severely influence the measured current at reverse bias and in the region of small forward currents. In addition, the voltage-dependent *I-V* characteristic of the *n*-GaAs/n^+-GaN heterojunction, which was in series to

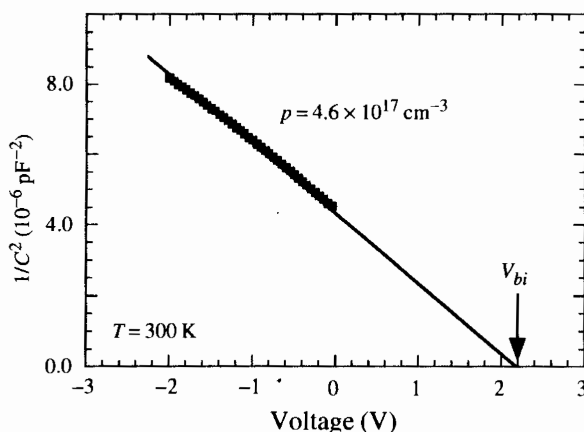

Figure 9.47 Capacitance-voltage characteristic of a *c*-GaN/GaAs (001) *p*-*n* junction plot in a $1/C^2$ versus V diagram.

the GaN *p*-*n* diode, further deformed the I-V curve of the whole structure. For these reasons, fitting the measured I-V curve to the standard diode equation $I = I_0 \times [\exp(qV/nkT) - 1]$ resulted in very large ideality factors n (>4), as they were also reported in the literature [5].

The C-V characteristics of the structure was linear when plotted in a $1/C^2$ versus V diagram, as shown in Figure 9.47, indicating that the cubic GaN n^+-p junction was abrupt. The built-in voltage, V_{bi}, and the acceptor concentration, N_A, were determined from the x intercept and the slope of the linear curve fit, respectively. For V_{bi}, a value of 2.2 eV was estimated, which is in good agreement with the value measured by Tanaka and co-authors [98] for MOCVD-grown cubic *p*-*n* junctions ($V_{bi} = 2.2$ V) and with values determined by Dmitriev [262] on hexagonal GaN *p*-*n* junctions grown on conducting SiC substrates ($V_{bi} = 2.7$ to 3.5 V). Using an permittivity $\varepsilon_s = 8.9 \times \varepsilon_0$ for cubic GaN [47], the carrier concentration, as determined from the slope of the linear curve fit, was $4.6 \times 10^{17}\ \text{cm}^{-3}$. Hall effect measurements of an Mg-doped *c*-GaN reference sample grown at identical growth conditions ($T_{sub} = 720\,°\text{C}$, $T_{\text{Mg}} = 350\,°\text{C}$) on semi-insulating GaAs substrates showed comparable free hole concentrations [22].

Figure 9.48 shows the EL of the cubic GaN n^+-p junction through the semitransparent part of the *p*-type contact. The EL-spectrum is peaked at 3.2 eV (387 nm) with an FWHM of 150 meV (20 nm). The EL-spectrum is nearly identical to the RT PL-spectrum (Figure 9.45a), even the smaller features of the PL spectra—for example, the small hexagonal peaks at 3.4 eV—are clearly reproduced in the EL-spectrum. This supports the interpretation that in MBE-grown cubic GaN LEDs the dominating recombination

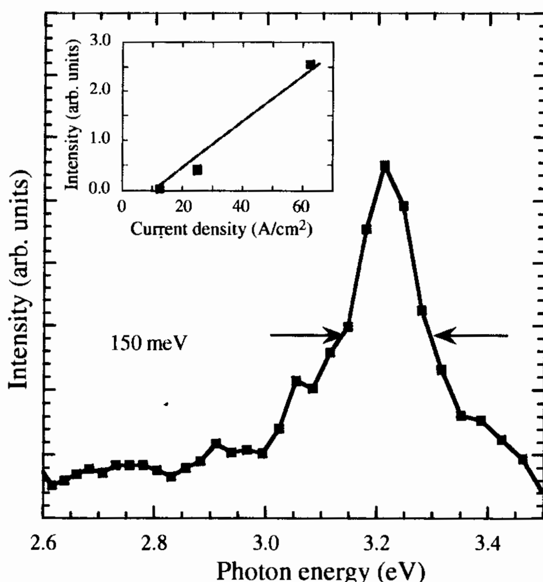

Figure 9.48 Electroluminescence spectrum emitted through a semitransparent Au contact of a *c*-GaN p-n^+ junction at a current of 150 mA and at room temperature. The inset shows the intensity of the electroluminescence as a function of the current density.

processes are near–band-edge transitions. This is in contrast to MOCVD-grown cubic LEDs, where the emission originated from the blue Mg-related impurity mediated recombination [5]. Similar differences in the LED emission of MBE- and MOCVD-grown samples also have been reported for hexagonal GaN samples [263]. Due to the dominating near-band transition, the observed FWHM is also within the narrowest values ever reported for UV LEDs. In the inset of Figure 9.48, the EL-intensity versus current density is plotted. A linear increase of the intensity with increasing current density is measured, and no shift of the EL-spectrum to lower energies is observed.

These results clearly demonstrate the applicability of *c*-GaN on GaAs device structures for low-cost production of blue LEDs and LDs. However, much work has to be done to optimize the device structures. In addition, for device applications of cubic III-nitrides, it will be necessary to significantly reduce the dislocation density.

9.8 GROWTH AND CHARACTERIZATION OF MBE-GROWN CUBIC $In_xGa_{1-x}N$

Modern optoelectronic devices such as LEDs or LDs utilize both electron and optical confinement effects to increase device performances. To realize

such advanced devices with c-III-nitrides, cubic $In_xGa_{1-x}N$ is used as an active layer (QW). The growth of c-$In_xGa_{1-x}N$ layers is difficult for several reasons: first, because of the metastability of the cubic phase itself, and second due to strong spatial fluctuations of the In-content caused by spinodal decomposition of the material. In additon, a strong variation of the sticking coefficient of In with temperature further complicates the epitaxial growth. The inhomogeneities and alloy fluctuations may strongly influence the optical properties of the optoelectronic devices. The growth of cubic $In_xGa_{1-x}N$ layers may therefore be considered as a major issue on the way toward a cubic group III-nitride–based laser.

In hexagonal $In_xGa_{1-x}N$, spontaneous and strain-induced PZ fields complicate the analysis of such QWs. In order to understand the precise mechanisms of the bandgap inhomogeneity and carrier localization and to obtain long-wavelength LDs expanding from pure blue to red wavelengths, fabrication and investigation of cubic zincblende $In_xGa_{1-x}N$ QWs are mandatory to eliminate the modulation due to spontaneous and strain-induced piezoelectricity [264].

Regarding cubic $In_xGa_{1-x}N$, there are a few reports about c-$In_xGa_{1-x}N$ alloy grown by MOMBE [12], MBE [13,14,16], and MOVCD [94,265]. Abernathy and colleagues [12] reported about electrical and structural properties of MOMBE-grown c-$In_xGa_{1-x}N$, but did not provide optical data. Attempts to grow c-$In_xGa_{1-x}N$ with a dc-plasma source [13] resulted in films showing no detectable luminescence signal above 70 K and, due to the low N-flux of the dc-source, the In mole fraction was limited to $x \leq 0.11$ as a result of massive In segregation. This limit could be overcome by the use of a water-cooled RF plasma source providing a considerably higher N-flux [14]. PL and measurements of optical gain of MBE-grown c-$In_xGa_{1-x}N$ were reported by Frey and co-authors [16]. Recently successful growth by MOCVD was reported by Nakadeira and Tanaka [94] ($In_{0.03}Ga_{0.97}N$) and by Sun and colleagues [265], who increased the In-mole fraction up to 24 percent. All these c-$In_xGa_{1-x}N$ epilayers were deposited on GaAs (001) substrates.

9.8.1 Growth of Cubic $In_xGa_{1-x}N$

Different samples are investigated: (1) an approximately 1-μm-thick c-GaN film; (2) c-$In_xGa_{1-x}N$ layers of various In content ($x < 0.4$) and thicknesses between 70 and 330 nm, each on top of a 180 nm c-GaN buffer layer; and (3) a cubic InN epilayer on an InAs-buffer layer. All samples are grown by RF-plasma-assisted MBE on semi-insulating GaAs (001) substrates. The c-GaN epilayer and the c-GaN buffer layers are grown at a substrate temperature of 720 °C under carefully controlled stoichiometric conditions, as previously described [9]. The $In_xGa_{1-x}N$ layers ($x < 0.4$) are deposited at

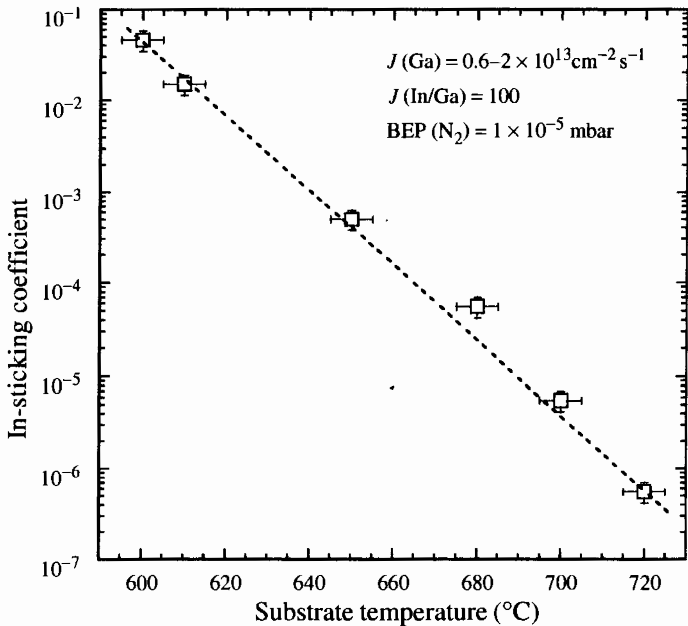

Figure 9.49 Sticking coefficience of In as a function of substrate temperature.

lower growth temperatures (610 °C to 680 °C) with a reduced Ga-flux (about 20 percent less) and the In-flux adjusted to establish a metal-rich surface composition. The growth has been continuously monitored by RHEED.

Due to the high vapor pressure of In at the growth temperatures used for the $In_xGa_{1-x}N$ epitaxy (610 °C to 680 °C), re-evaporation of In is a severe problem. Therefore, the estimation of the temperature dependence of the sticking coefficient of In is of basic importance for good reproducibility. In Figure 9.49 the sticking coefficient of In is measured versus substrate temperature. A dramatic decrease of over five orders of magnitude is observed in the temperature range between 600 °C to 720 °C. Therefore, variations in substrate temperature by only 5 K results in a variation of the In-content by a factor of 2. Consequently, strong variation of the In-content in the InGaN epilayers due to small changes of the substrate temperatures are expected.

The binary cubic InN layers are grown on top of an InAs buffer film on GaAs (001) substrates. The 300-nm-thick InAs buffer is deposited at 480 °C under (2 × 4) reconstruction to ensure As-stabilized conditions. The growth of the InN layer is preceeded by a nitridation of the InAs surface, which is performed at a reduced temperature of 450 °C, with both As as well as In sources closed. After formation of a few monolayers of *c*-InN during the nitridation process, based on the N-As surface anion exchange, the In

cell is reopened and the growth of c-InN is started at the same temperature (450 °C). From the RHEED pattern, the pure cubic phase growing on the surface is checked and a lattice constant for c-InN of about 5.04 ± 0.09 Å is measured [266]. The InN growth rate is 80 nm/hr and the thickness of the c-InN film is 300 nm.

9.8.2 Structural and Vibrational Properties

The crystalline structure of the binary c-InN sample has been identified by means of x-ray diffraction (XRD) measurements. Figure 9.50 shows the XRD pattern of the InN/InAs/GaAs sample. The different peaks associated to the (002) and (004) planes of the GaAs substrate as well as the InAs buffer layer are clearly seen at $2\Theta \simeq 31.1°$, 66.3°, and 29.6°, 61.1°, respectively. The cubic phase of the InN layer is identified by the presence of diffraction peaks at $2\Theta = 36.1°$ and 76.4° originating from the zincblende-type InN (002) and (004) planes, respectively. From these x-ray measurements, a lattice constant for the c-InN equal to 4.98 ± 0.01 Å is obtained in good agreement with experimental data from Strite and coworkers [44]. This value of the lattice constant is within the one determined by RHEED measurements, taking into account the larger error involved in this method. The difference between these two measurements (0.06 Å) is not due to the temperature difference of about 400 °C, which would increase the lattice constant by only 0.01 Å.

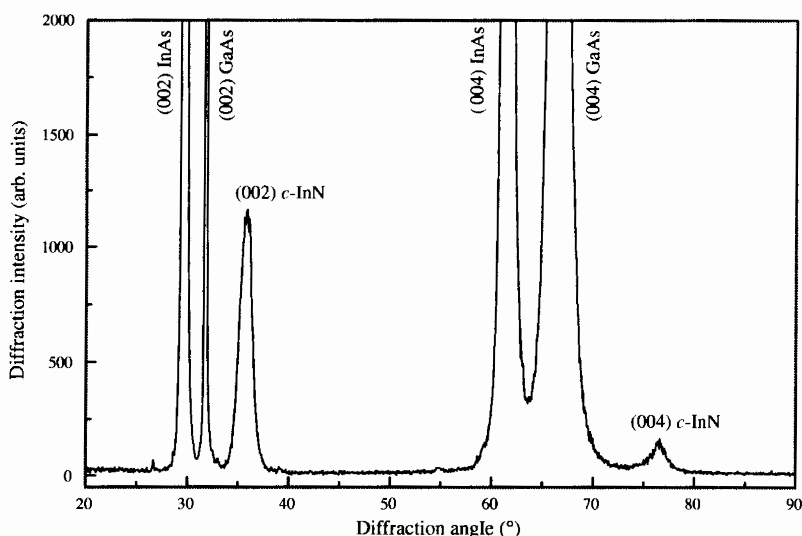

Figure 9.50 X-ray diffraction pattern of the cubic InN epilayer grown on InAs/GaAs (001).

TEM investigations on a 42-nm-thick c-InN sample showed that the interface InAs/InN is not flat and that the InN layer contains a high density of stacking faults parallel to the {111} InN planes.

For the $In_xGa_{1-x}N$ alloys, the In-composition x of the layers is determined by x-ray measurements ($\omega - 2\Theta$ scans), assuming the validity of Vegard's law [16]. For the linear interpolation, the lattice constants used are $a_{GaN} = 0.453$ nm and $a_{InN} = 0.497$ nm, respectively [266,267]. In Figure 9.51, $\omega - 2\Theta$ scans along the symmetric (002) and the asymmetric (113) reflexes of c-$In_xGa_{1-x}N$/GaN epilayers are shown for samples with

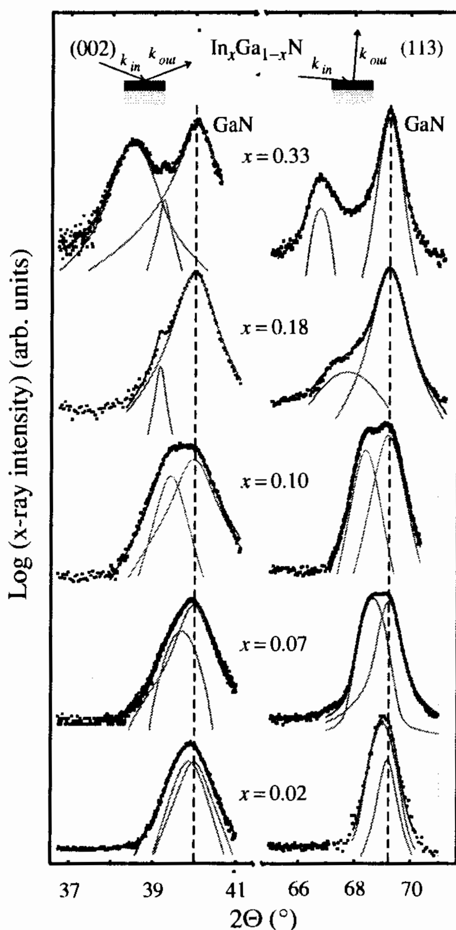

Figure 9.51 $\omega - 2\Theta$ scans of $In_xGa_{1-x}N$/GaN heterostructures with various In-content x. The left column shows $\omega - 2\Theta$ scans of the symmetric (002) reflex and the right column shows $\omega - 2\Theta$ scans of the asymmetric (113) reflex. On top of each column a schematic drawing of the x-ray beam geometry is shown.

different In-content. The In-content increases from $x = 0.02$ at the bottom to $x = 0.33$ at the top. For accurate estimation of the peak positions of the corresponding c-GaN and c-$In_xGa_{1-x}N$ reflexes, all spectra are well-fitted by two Pseudo-Voigt functions (dotted curves), one for the c-GaN and the other for the c-$In_xGa_{1-x}N$. The peaks at $2\Theta = 39.9°$ and $69.1°$ correspond to the c-GaN reflections (indicated by the dashed lines), and the peaks at lower Bragg angles are ascribed to the ternary c-$In_xGa_{1-x}N$.

From reciprocal space maps (RSM) of the symmetric (002) and the asymmetric (113) Bragg reflexes, we find that the 70- to 330-nm-thick $In_xGa_{1-x}N$ layers are fully relaxed. Figure 9.52 shows the distribution in reciprocal space of the scattered x-ray intensity of the symmetric (002)

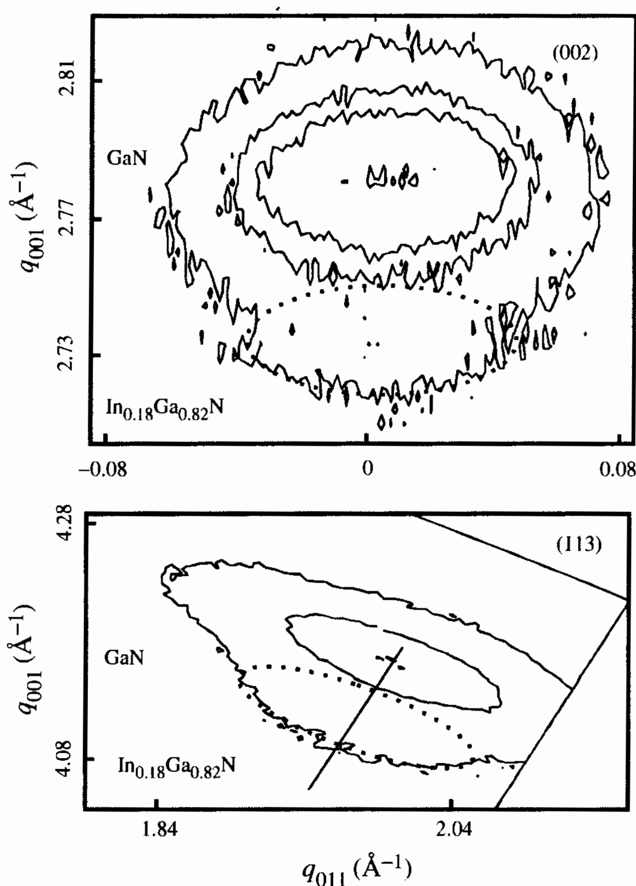

Figure 9.52 Reciprocal space map of the (002) and (113) Bragg reflex of a 70-nm-thick c-$In_{0.18}Ga_{0.82}N$/GaN heterostructure. The c-$In_{0.18}Ga_{0.82}N$ reflex is emphasized by dashed ellipses.

and the asymmetric (113) Bragg reflex from a 70-nm-thick $x = 0.18$ c-$In_xGa_{1-x}N$/GaN heterostructure. The intensity contours of the GaN and the $In_xGa_{1-x}N$ reflex for maximum and half-maximum intensity of the respective peaks are depicted. The maximum of the reflected intensity from the $In_{0.18}Ga_{0.82}N$ layers is located along a direction in reciprocal space, which points from the GaN Bragg reflex to the origin (000) of the reciprocal space, revealing that this $In_{0.18}Ga_{0.82}N$ layers, is fully relaxed. Similar RSMs were obtained with $x = 0.02$ and $x = 0.07$ layers. Unfortunately, due to the overlap of the GaN and the $In_xGa_{1-x}N$ layers, reflex the intensity contour did not allow an unambiguous identification of the degree of lattice relaxation in these layers. However, the distance of the RHEED reflexes measured in situ during growth clearly revealed an increase of the in-plane lattice constant in both samples due to lattice relaxation. Figure 9.53 shows the measured in-plane lattice constant of c-$In_{0.07}Ga_{0.93}N$ as a function of the epilayer thickness. Whereas at a layer thickness below 30 nm the lattice constant is estimated to be about 4.52 Å, which corresponds to the lattice constant of c-GaN, the in-plane lattice constant above 30 nm increased notably to a value of 4.556 Å. This lattice constant is in agreement with an In content of 7 percent and indisputable proof that this layer is relaxed. From these measurements also a critical layer thickness h_c of about 30 nm is estimated, below the thickness the c-$In_{0.07}Ga_{0.93}N$ grows pseudomorphically.

In some cases, the In content and the layer thickness are also measured by RBS [127]. Within the experimental error, the estimated In-values agree with those of the x-ray data. For some samples, however, an In segregation to the film surface is observed [268].

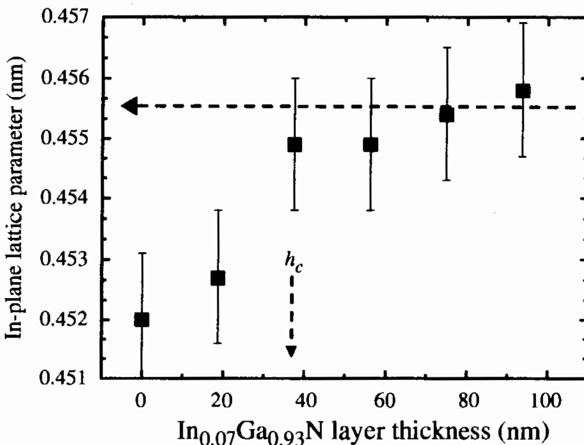

Figure 9.53 In-plane lattice constant measured by in situ RHEED of c-$In_{0.07}Ga_{0.93}N$ on cubic GaN as a function of the thickness of the epilayer.

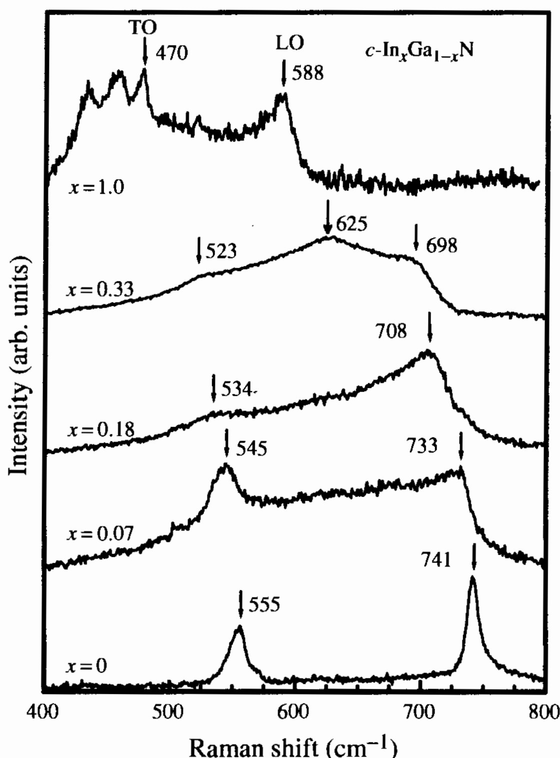

Figure 9.54 Room-temperature micro-Raman spectra of the c-$In_xGa_{1-x}N$ epilayers with $x = 0.0, 0.07, 0.18, 0.33$, and 1.0. The data for c-InN ($x = 1.0$) and c-GaN ($x = 0$) are taken from References 267 and 116, respectively.

Figure 9.54 shows the room-temperature Raman spectra of various cubic $In_xGa_{1-x}N$ samples with $x = 0, 0.07, 0.18, 0.33$, and 1.0 obtained in the backscattering configuration. The 488.0 nm line of the Ar-ion laser is employed as the excitation and the power is kept below 3 mW. The frequencies of the different phonon modes are indicated by arrows in the figure. The TO and LO phonon modes for the cubic GaN are observed at 555 cm^{-1} and 741 cm^{-1}, respectively, in agreement with previously published data [110,116]. With increasing In-content, a clear shift to lower frequencies is measured. The peak frequency at 625 cm^{-1} in the spectrum of the $In_{0.33}Ga_{0.67}N$ sample is tentatively ascribed to the LO phonon mode of the alloy with $x = 0.8$, which is generated by phase separation. This issue will be explained in more detail in Section 9.8.5. For the binary c-InN sample ($x = 1$), the TO and LO modes are found at 470 cm^{-1} and 586 cm^{-1}, respectively. The two peaks near the TO phonon mode correspond to the second-order phonon modes (2 LO and 2 TO) of the InAs buffer layer [269].

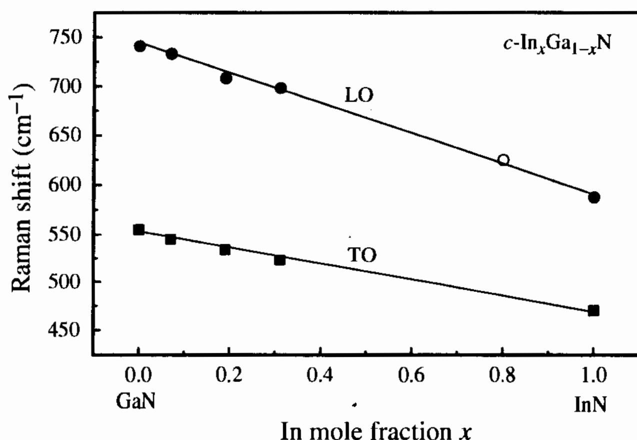

Figure 9.55 TO and LO Raman mode frequencies of the c-In$_x$Ga$_{1-x}$N epilayers versus alloy composition. The straight lines connect the frequencies of the binary compounds c-GaN and c-InN.

Recent measurements showed that these second-order InAs contributions could be strongly suppressed by using crossed polarization arrangement and resonant excitation [270], allowing unique identification of the c-InN TO mode.

The evolution of the TO and LO peak frequencies with the In-alloy composition is depicted in Figure 9.55. The plot shows that the TO and LO phonon frequencies lie on straight lines connecting the corresponding values obtained for the binary compounds c-GaN and c-InN. These data suggest a one-mode-type behavior for the In$_x$Ga$_{1-x}$N, in agreement with a phenomenological theory proposed by Chang and Mitra [271]. The lattice dynamics of random A$_x$B$_{1-x}$N alloys (A, B = Al, Ga, In) have also been calculated by Grille and coworkers [272] using a modified random-element isodisplacement model. The one-mode-type behavior and the linear dependence of the TO and LO frequencies on the alloy composition in c-In$_x$Ga$_{1-x}$N observed in our experiments are accurately reproduced by the latter group's theoretical calculation.

9.8.3 Optical Properties

One of the most important parameters in designing advanced optoelectronic devices is the dependence of the energy gap $E_G(x)$ on the In-composition, x. At room temperature, the gap energy of various In$_x$Ga$_{1-x}$N epilayers has been measured by spectroscopic ellisometry (SE) and for the c-GaN also by photoreflectance [273,274]. For determining the refractive index, n, of the In$_x$Ga$_{1-x}$N layers, the SE data are fitted with the adjustable

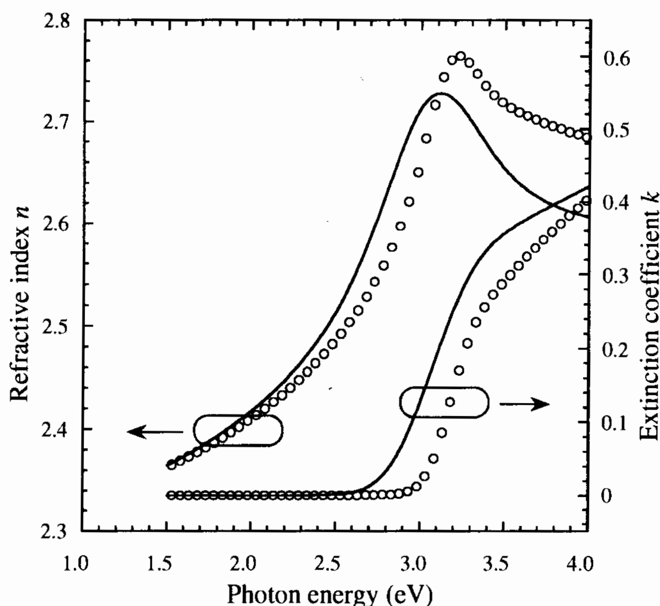

Figure 9.56 Refractive indices and extinction coefficients for c-$In_xGa_{1-x}N$ films with x = 0.02 (○) and x = 0.07 (—).

parameters: magnitude, broadening, and energetic position of the two critical points as well as the layer thicknesses. Details of the fitting procedure that has been used to evaluate the data are given by Goldhahn and Shokhovets [275]. Figure 9.56 shows the refractive indices and extinction coefficients of two c-$In_xGa_{1-x}N$ films with $x = 0.02$ (circles) and $x = 0.07$ (full line). The gap structure is still strongly pronounced, but appreciably shifted to lower energies, compared with GaN (see for comparison Figure 9.13). The larger broadening is probably caused by increased alloy scattering and small composition fluctuations. The energy gap at low temperature is calculated by adding 80 meV, which corresponds to the bandgap shift between room temperature and 2 K in c-GaN [10]. Figure 9.57 shows the energy gap at 2 K of $In_xGa_{1-x}N$ as a function of the In-content. The full squares are results from SE measurements and the full triangles have been reported in Müllhäuser and colleagues [276], where transmission measurements were analyzed. Assuming the bandgap of InN to be 1.9 eV, all data can be fitted by a parabolic expression (solid curve) from which a bowing factor of $b = 1.07$ eV is obtained. This value is in excellent agreement with recent calculations of Wright and Nelson [277]. The dashed lines in Figure 9.57 correspond to calculations using bowing parameters $b = 1.8$ eV and 3.8 eV, respectively. These values for the bowing

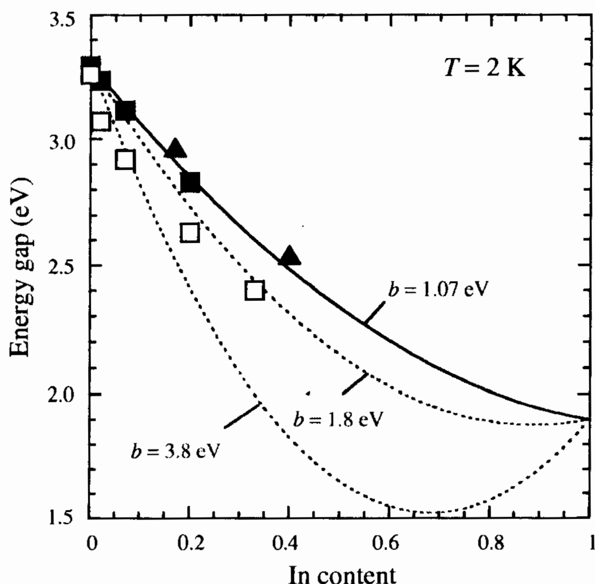

Figure 9.57 Energy gap of c-$In_xGa_{1-x}N$ versus In-content. Full squares represent data measured by spectroscopic ellipsometry [274], full triangles are results of Müllhäuser et al. [276]. The open squares are the peak position of the low-temperature PL under low excitation conditions. The upper full line is the best fit to the experimental data, from which a bowing factor of 1.07 eV is estimated. The dashed lines are calculated for different bowing factors of 1.8 and 3.8 eV, respectively.

factor have been discussed for the gap energy versus x in the hexagonal phase [278].

Low-temperature PL-spectra excited by the 325 nm radiation of a cw HeCd laser are shown as full lines in Figure 9.58. The PL spectra of the $In_xGa_{1-x}N$ layers with $x \leq 0.2$ consist of one emission band. The FWHM of this band is in the order of 200 to 450 meV and is slightly increasing with increasing In-content. The peak position of the dominant transition in the low-temperature PL-spectra versus In-content is also plotted in Figure 9.57 (open squares). A Stokes shift of about 200 meV for $x > 0$, compared with the E_g obtained by spectrally resolved ellipsometry [274] is seen. The corresponding E_g values are indicated by arrows in the PL-spectra (Figure 9.58). This Stokes shift indicates that the dominant transition may be due to either impurity related transitions or due to localized states. The dashed curves in Figure 9.58 are spectra taken from the edge of cleaved $In_xGa_{1-x}N$ layers. In this experiment, the epilayers are excited by the 340 nm light of a pulsed laser with an intensity of 1 MW cm^{-2}. As can be clearly seen, the peak energy of the edge emission is notably shifted to higher energies and is close to the gap energies measured by ellipsometry (arrows in Figure 9.58). At 1 MW cm^{-2}

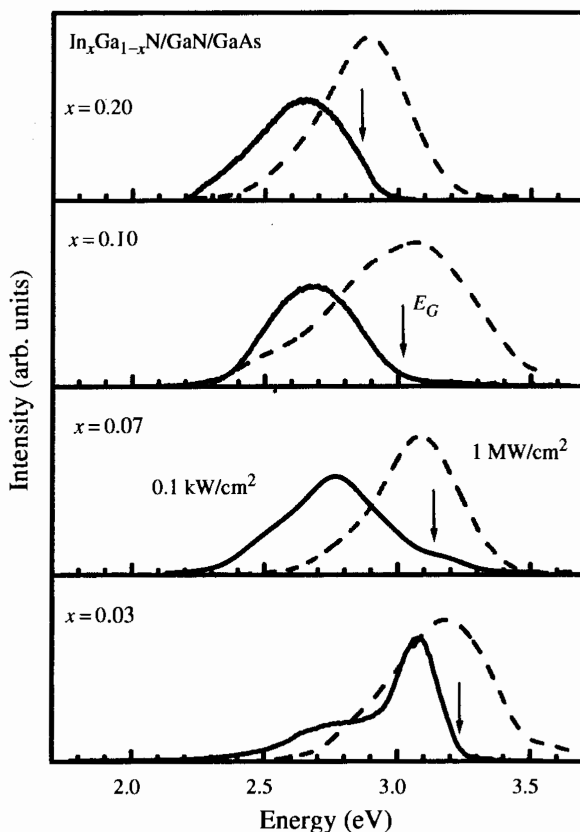

Figure 9.58 2 K PL-spectra of c-$In_xGa_{1-x}N$ films (—) and the high-excitation edge emission (- - -). The corresponding energy gap, estimated from ellipsometric measurements, are indicated by arrows.

all impurity-related or localized states-related transitions that contribute to PL at weak excitation are saturated and the observed emission is the near bandedge luminescence of the $In_xGa_{1-x}N$ layers.

Time-resolved PL measurements [279] and spatially resolved cathodoluminescence (CL) [280] measurements further corroborate the suggestion that the origin of the luminescence is due to localized carriers confined at varying In fluctuations. A nonexponential decay is observed in all $In_xGa_{1-x}N$ samples. The shape of the transients can be well described by the model of stretched exponentials, which has been introduced to describe the radiative decay of strongly disordered systems of localized recombination centers and has been successfully applied to hexagonal GaN [281]. To understand the correlation of structural and optical properties, CL spectroscopy has been performed and the CL mappings are presented in Figure 9.59 for the

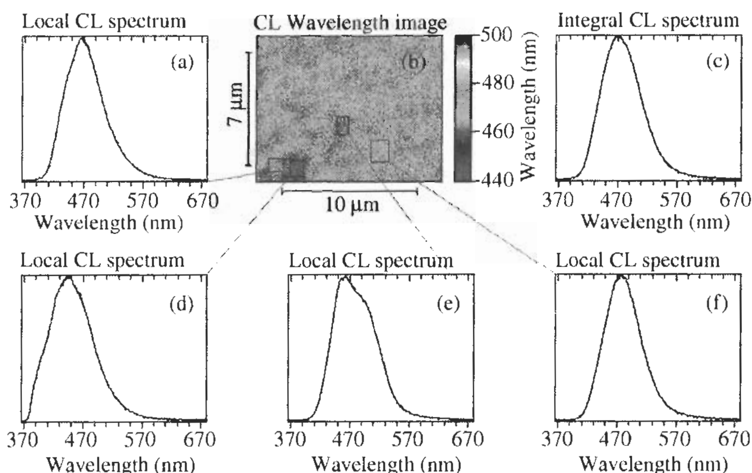

Figure 9.59 Low-temperature CL-spectra of c-$In_xGa_{1-x}N$. (a) CL-wavelength image, (b) integral CL spectrum, and (c)–(f) local CL spectra.

7 percent $In_xGa_{1-x}N$ sample. In Figure 9.59, a magnified CL wavelength image (CLWI) (a) is shown together with an integral spectrum (b) and a set of local CL spectra (c-i). The local CL spectra in this area (Figure 9.59c and d) exhibit broad emission bands, but the peak position changes according to local In-content. This is a typical feature for all samples investigated. The degree of compositional fluctuations is directly monitored by the CL mappings. For samples with higher In-contents (>10 percent), the degree of In-fluctuations is strongly enhanced. This can be seen in the histograms of the CL-wavelength mappings, where the frequency of occurrence of the emissions is collected. Figure 9.60 displays the histograms for samples with different In-contents. The half-width of the histogram monitors the degree of In-fluctuation in the samples and is found to be lowest in the 7 percent sample, whereas for the 20 percent sample a strongly inhomogeneous distribution of In over the sample is measured. Moreover, for the higher In concentration, the histograms are no longer given by a statistical Gaussian distribution but becomes multimodal with several relative maxima directly visualizing phase separation effects.

9.8.4 Optical Gain

The gain in our cubic $In_xGa_{1-x}N/GaN$ heterostructures has been measured by the variable stripe length method, as explained earlier. Low-temperature gain spectra of the $In_{0.07}Ga_{0.93}N$ sample obtained at different excitation intensities up to 5 MW/cm^2 are depicted in Figure 9.61. Gain is already

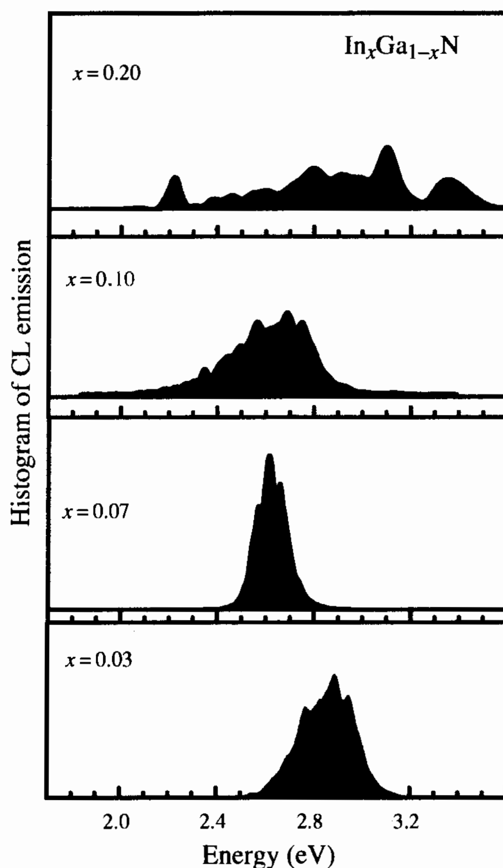

Figure 9.60 Histograms of the CL-wavelength images of c-$In_xGa_{1-x}N$ with different In content.

observed at an excitation intensity of about 0.5 MW/cm^2. Increasing the excitation intensity results in a shift of the gain-absorption crossover to higher energies, indicating band-filling of localized states. In addition, the gain structure broadens and the peak position shifts to higher energies. The gain of an electron–hole plasma, however, is expected to shift to lower energies with increasing density [4]. Therefore, this behavior is a further indication that the optical amplification is due to localized states. From these spectra one clear advantage of the cubic material system can be noticed. Optical gain is observed up to 500 nm due to the lack of detrimental pyroelectric and PZ fields [280].

For the $In_xGa_{1-x}N$ samples with x varying from 0.03 to 0.20, the gain spectra at a fixed excitation density of 5 MW/cm^2 are shown in Figure 9.62.

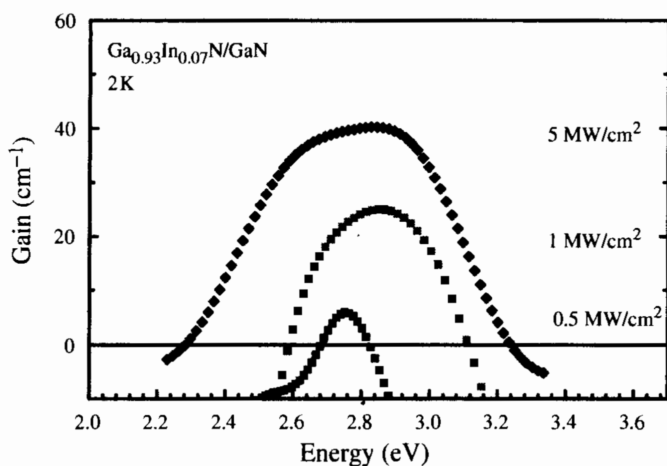

Figure 9.61 Gain spectra of the c-$In_{0.07}Ga_{0.93}N$ sample at various excitation densities.

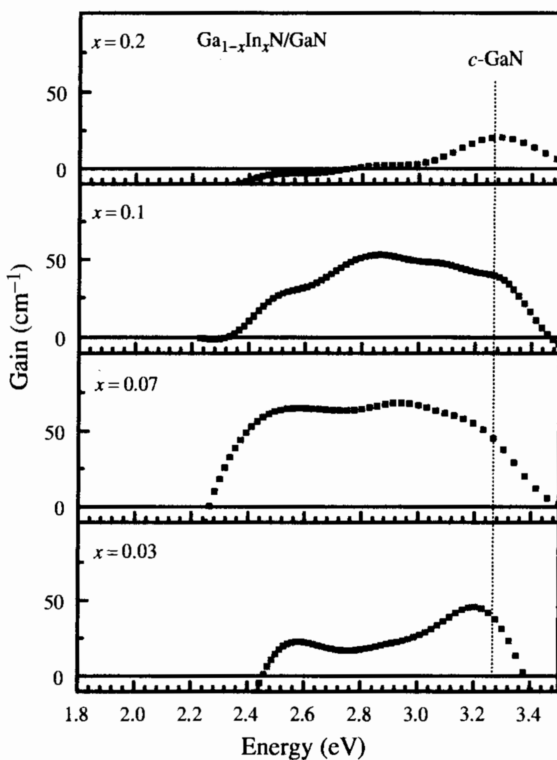

Figure 9.62 Gain spectra measured at a fixed excitation density of 5 MW/cm^2 for cubic $In_xGa_{1-x}N$ epilayers with varying In content.

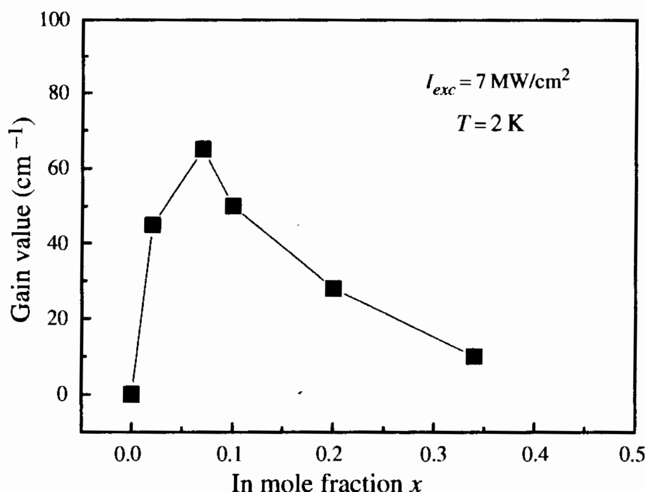

Figure 9.63 Peak gain value at 2 K versus In-content of the cubic $In_xGa_{1-x}N$ epilayers at a fixed excitation density of 7 MW/cm^2.

With increasing In content (up to 7 percent), the gain profiles are broadened. A maximum gain value of 60 cm^{-1} is obtained at this excitation condition. However, for higher In concentration, the optical gain decreases and is totally suppressed in the $In_{0.2}Ga_{0.8}N$ sample. This gain suppression may be due to the impact of phase separation on quantum efficiency.

To monitor the impact of the degree of In-fluctuations on the optical amplification, gain spectra at a fixed excitation density of 7 MW/cm^2 have been measured. The results are shown in Figure 9.63 where the peak gain value is plotted versus In-concentration. The sample with $x = 0.07$, which also has the narrowest distribution in CL-wavelength image histograms, exhibits the highest gain value, whereas for x above 0.2 the optical amplification is suppressed. This gain suppression in In-rich samples may be due to the InN-GaN miscibility gap [7] and the enhanced tendency for the formation of In clusters. The insufficient incorporation and solubility of In in the c-$In_xGa_{1-x}N$ layers seems to limit the optical gain in the green spectral range.

9.8.5 Electrical Properties

The electrical transport properties of InN and $In_xGa_{1-x}N$ are, in general, characterized by high carrier concentrations ($\sim 10^{20}$ cm^{-3}) and low mobilities (~ 100 cm^2/Vs). The room temperature values of the free electron concentration (full squares) and the electron mobility (open squares)

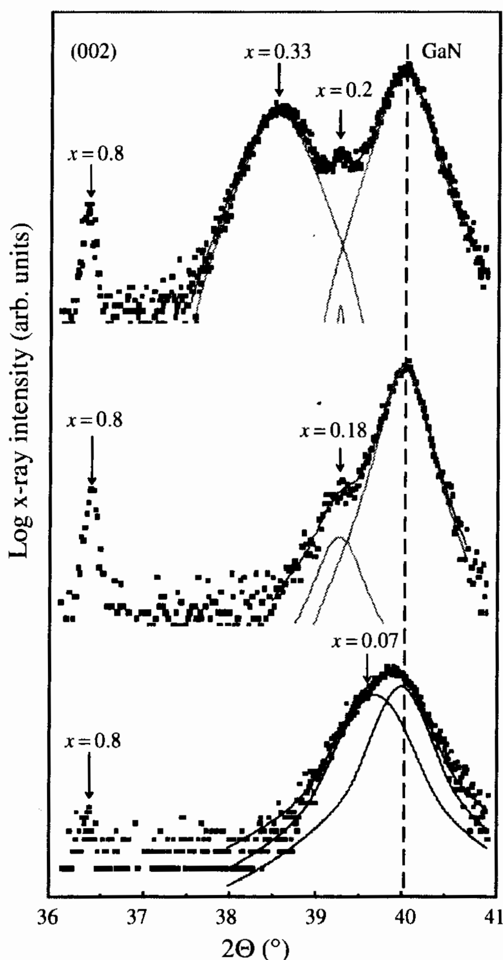

Figure 9.64 Extended $\omega - 2\Theta$ scans of the symmetric (002) Bragg reflex of c-$In_xGa_{1-x}N$/GaN epitaxial layers with an alloy composition of $x = 0.07, 0.18$, and 0.33. The squares are the experimental data and the solid curves are least square fits with pseudo-Voigt functions. The composition of the separated phases are indicated by arrows.

measured at room temperature are plotted versus In mole fraction in Figure 9.64 for the cubic $In_xGa_{1-x}N$ epilayers. Due to the incorporation of In into the epilayers, the samples are highly n-type doped with a carrier concentration of about $7 \times 10^{18}\,cm^{-3}$. The concentration even increases up to a value of $5 \times 10^{20}\,cm^{-3}$ for pure cubic InN. The mobility, however, decreases with increasing In-content. Similar electrical data have been reported by Abernathy and colleagues [228], who used metalorganic MBE with either He (circles) or H_2 (triangles) as carrier gas. Their data are also

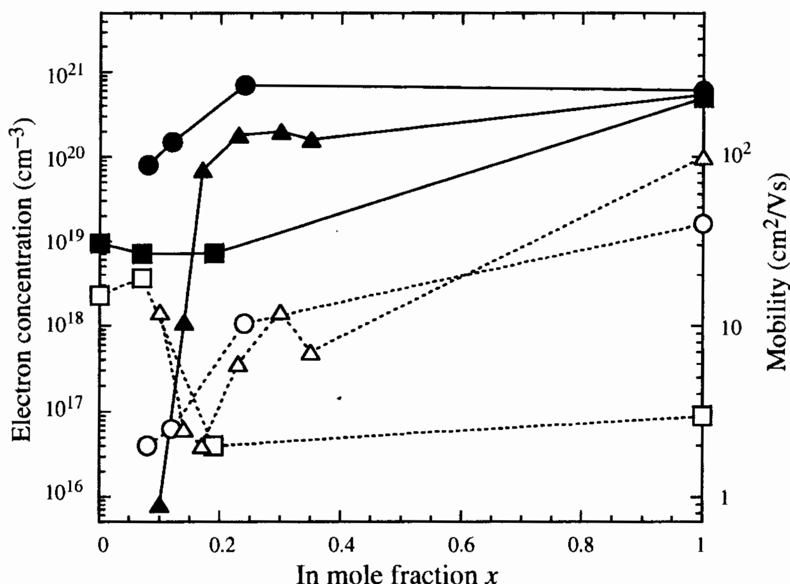

Figure 9.65 Free carrier concentration (full symbols) and mobility (open symbols) versus In content. The squares are my own measurements, circles and triangles are taken from Abernathy et al. [228].

included in Figure 9.65 as circles (He carrier gas) and triangles (H_2 carrier gas), respectively. They observed a sharp fall-off in the autodoping level for low ($x < 0.2$) $In_xGa_{1-x}N$ samples, which is more dramatic in materials with the H_2 carrier gas and this may be due to hydrogen passivation of the defects responsible for the n-type conductivity.

It is generally believed that the high carrier concentration is derived from a high density of N vacancies produced during growth, although this seems less likely in the light of the trends observed in InN grown using various V/III ratios [282] and recent results in mature hexagonal and cubic GaN epilayers. The same arguments have been used for the residual n-type background carrier concentrations in h-GaN, where currently it has become clear that O and Si, not V_N, are the main impurities responsible for the high n-type doping. Probably the same arguments are true for the $In_xGa_{1-x}N$ alloys; however, due to insuffìcent layer qualities an unambiguous proof is missing to date. Given the high carrier concentration, a low mobility is expected and even lower values are realized due to the intergrain scattering that is present even in the best samples.

An exception to the general behavior is found in the work of Tansley and Foley [283,284], where an RF sputtering technique was used to produce films with carrier concentrations near $10^{16}\,cm^{-3}$ and mobilities

near 4000 cm^2/Vs. Unfortunately, to date, all attempts to produce device-quality films with similar electrical transport properties (using techniques more amenable to standard semiconductor process) have been unsuccessful.

9.8.6 Phase-Separation in Cubic $In_xGa_{1-x}N$

Due to the large difference in the lattice constants between GaN and InN, the existence of a solid phase miscibility gap in $In_xGa_{1-x}N$ was predicted [285]. Advanced theoretical calculations, which also take into account the influence of biaxial strain, proposed that below a critical temperature of about 1295 K [286] spinodal decomposition should occur for unstrained $In_xGa_{1-x}N$. Therefore, at the growth temperature of the $In_xGa_{1-x}N$ epilayers (600 °C–700 °C) phase separation should take place and the formation of In-rich regions is expected for thick relaxed $In_xGa_{1-x}N$ films. However, in the presence of strain, phase separation may be suppressed. Therefore, for thin pseudomorphic $In_xGa_{1-x}N$/GaN QWs, spinodal decomposition is inhibited and the growth of $In_xGa_{1-x}N$/GaN QWs with high In content should be enabled without In-rich regions. A numerical study of $In_xGa_{1-x}N$ pattern formation caused by phase separation showed that over a wide In compositional range ($0 < x < 0.6$) dot-like structures should appear due to effects of strain and defects [287]. These self-assembled In-rich dots may severely influence the characteristic optical properties and are discussed in hexagonal $In_xGa_{1-x}N$ based semiconductor LEDs to be responsible for the success of these devices [288].

As previously mentioned for $In_xGa_{1-x}N$ epilayers with higher In content, x-ray data (Figure 9.51), Raman-measurements (Figure 9.54), spatially resolved CL-measurements (Figure 9.59), and gain measurements (Figure 9.62) gave clear evidence that phase separations and spinodal decomposition also occurs in cubic $In_xGa_{1-x}N$ epilayers. Figure 9.65 shows extended $\omega - 2\Theta$ scans of the symmetric (002) Bragg reflex of c-$In_xGa_{1-x}N$/GaN epitaxial layers with various In composition $x = 0.07$, 0.18, and 0.33, respectively. The spectra are fitted by pseudo-Voigt functions (full curves) revealing a peak at $2\Theta = 39.90°$, corresponding to the c-GaN reflection, and peaks at lower values of 2Θ, corresponding to the fully relaxed c-$In_xGa_{1-x}N$ layers. In all three samples, the presence of an In-rich phase ($x \cong 0.8$) is evident and emphasized in the spectra by arrows. For the c-$In_{0.33}Ga_{0.67}N$ epilayer, a second In-poor separated phase with $x = 0.2$ is also visible. Such an In-poor phase is expected and typical for the spinodal phase separation [285].

Room-temperature Raman spectra of the three c-$In_xGa_{1-x}N$ epilayers with x values between 0.07 and 0.33 recorded at an excitation energy $E_L =$ 2.6 eV are shown in Figure 9.66. With increasing nominal In-content an

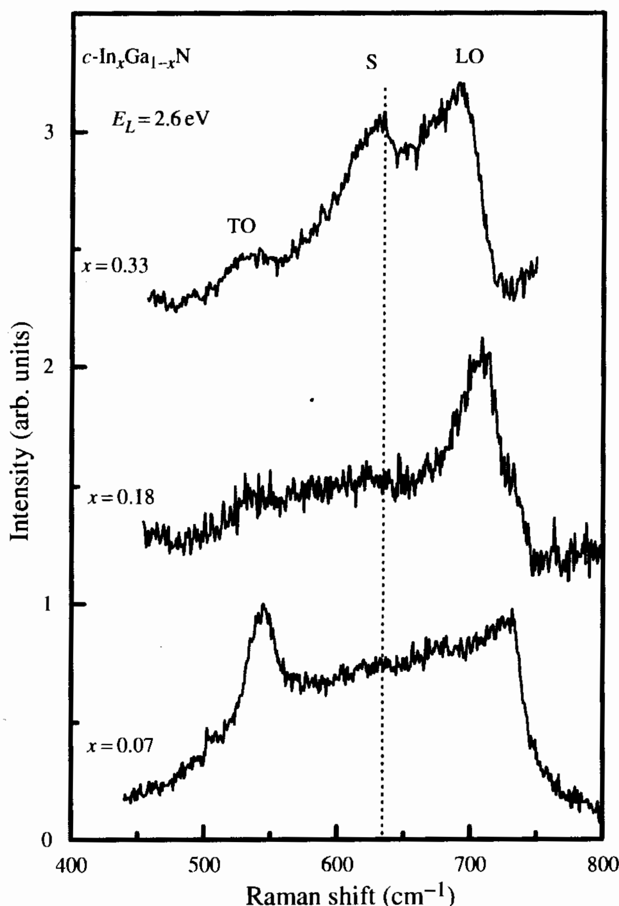

Figure 9.66 Raman spectra of different c-In$_x$Ga$_{1-x}$N samples with $x = 0.07, 0.18$, and 0.33 (excitation energy $E_L = 2.6\,\text{eV}$).

additional peak, labeled S, is emerging at about 630 cm^{-1}. Remarkably, no energetic shift in position is observed for the S-peak, indicating that this LO-Raman line is due to In$_x$Ga$_{1-x}$N with similar In-content. Because both the TO and the LO phonons in c-In$_x$Ga$_{1-x}$N exhibit a one-mode-type behavior and the frequencies display a linear dependence on alloy composition, the S-peak can be attributed to an LO mode of a separated phase of c-In$_x$Ga$_{1-x}$N with $x = 0.72 \pm 0.06$. This x value is in excellent agreement with that estimated for the In-rich phase ($x \cong 0.8$) by x-ray measurements. Therefore, the Raman measurements corroborate the x-ray results that phase separation in cubic In$_x$Ga$_{1-x}$N epilayers gives rise to a minority phase, with In concentration higher than the nominal one. The increase in intensity of the

S-peak further demonstrates that the volume of the In-rich phase in the layers increases dramatically when the In mole fraction of the layer exceeds about 20 percent.

Polarized resonant Raman spectroscopy (RRS) provides a suitable tool to identify QDs [289]. Taking into account the fact that QD radial modes are allowed (forbidden) in parallel (crossed) polarization, the QD nature of the In-rich separated phase inclusions in the epilayer can be checked. In Figure 9.67 the RRS spectra of the c-$In_{0.33}Ga_{0.67}N$ epilayer are shown for parallel $(z(xx)\bar{z})$ and crossed $(z(xy)\bar{z})$ geometries. In the $(z(xy)\bar{z})$ geometry the S-peak almost disappears, as it would be the case due to symmetry restrictions in a QD. Therefore, it has been concluded that the S-peak, which is marked by an arrow in Figure 9.67, is due to QD vibrations.

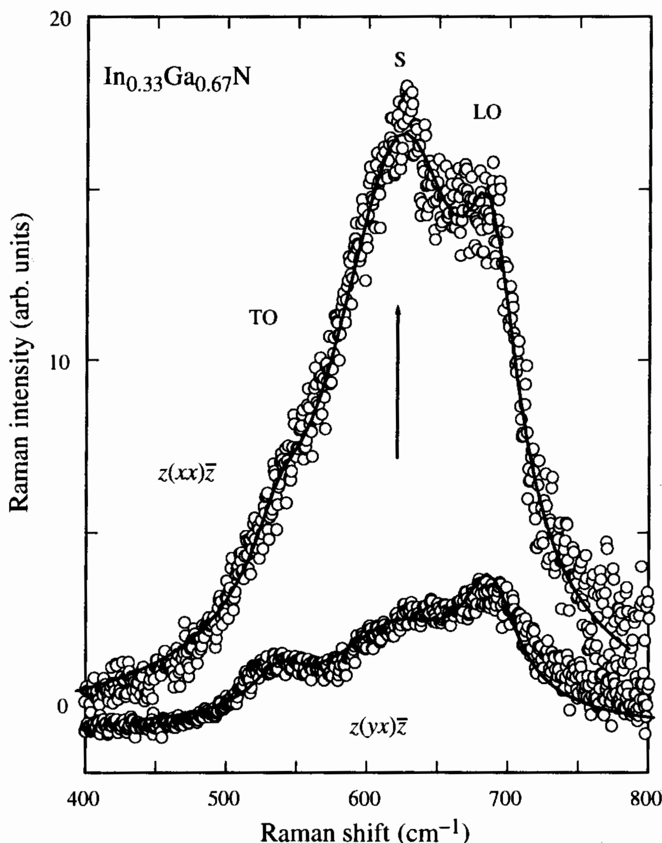

Figure 9.67 Polarized resonant Raman spectra of the c-$In_{0.33}Ga_{0.67}N$ epilayer excited with 2.4 eV. The solid lines are fittings to Lorentzian line shapes. The arrow points to the QD-related signal.

The S-peak in the Raman-spectra further shows a pronounced resonant excitation behavior with a maximum at about 2.4 eV and a linewidth exceeding 200 meV. In the range of excitation between 2.34 eV and 2.4 eV, the S-peak is even the strongest feature in the spectrum. Assuming the maximum to correspond to an outgoing resonance process and using the measured phonon energy of 78 meV, it is possible to estimate the energy of the resonant electronic state as 2.32 eV. This value is found to agree perfectly with the lowest luminescence emission energy of the samples investigated (see Figure 9.68a) and links the emission observed with c-$In_{0.33}Ga_{0.67}N$ layers to the In-rich phases present in the samples.

PL of the c-$In_xGa_{1-x}N$ layers has been excited by the 2.81 eV line of an HeCd laser in order to avoid luminescence from the underlaying GaN buffer. Room-temperature and 30 K PL-spectra obtained for various c-$In_xGa_{1-x}N$ epilayers are depicted in Figure 9.68. The lineshape of all spectra can be wellfitted by Gaussian functions with PL peak energies E_P and linewidths Γ (FWHM). For the c-$In_{0.07}Ga_{0.93}N$ layer, a second peak is observed at higher energies at room temperature (dashed curves in Figure 9.68a). At both temperatures the luminescence lines show a red shift and an increase of Γ with increasing In content. At room temperature (30 K), the red shift is 127 meV (197 meV) and Γ increases from 264 meV to 337 meV (240 to 339 meV) as x increases from 0.07 to 0.33. The integrated PL intensity shows only a weak variation between 300 K and 30 K, and the total shift in peak position, E_P, with temperature is 31 meV for the $In_{0.33}Ga_{0.67}N$ sample and 54 meV for $In_{0.18}Ga_{0.82}N$ sample, respectively. This shift is significantly smaller than the temperature variation of the bandgap of bulk c-GaN (80 meV). Both temperature effects are further characteristic for QD emission [290]. Defect-related processes that have been observed in c-GaN by CL at about 2.4 eV can be excluded as the origin for the emission, because the defect related luminescence is totally suppressed at low temperature.

Therefore, the emission can be analyzed in terms of quantum confinement effects. In Figure 9.69 the energy of the PL-emission and the measured energy gap of c-$In_xGa_{1-x}N$ are compared. The open circles and the open triangles are the gap measurements from the spectroscopic ellipsometry and from absorption measurements, as presented earlier. The solid curve represents a parabolic fit to these data assuming a value of 1.9 eV for the bandgap energy of c-InN. One immediately sees that the PL-emission is not related to the energy gap of the c-$In_xGa_{1-x}N$ alloys. However, as shown by RRS data, the emission is directly linked to the In-rich phase present in the samples. From x-ray and Raman measurements, the In-content of the In-rich phase is nearly independent of the composition of the c-$In_xGa_{1-x}N$ epilayer and is about 80 percent in all our samples. Because both polarization-dependent Raman measurements and the temperature-dependent PL measurements showed characteristics typical for QDs, the confinement energies ΔE

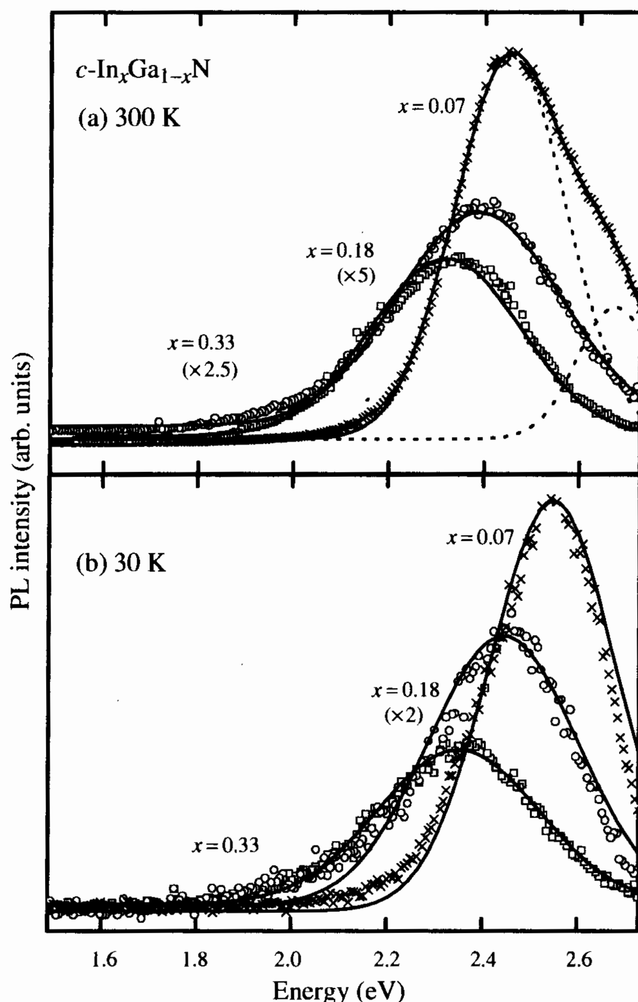

Figure 9.68 (a) 300 K and (b) 30 K PL-spectra of c-$In_xGa_{1-x}N$ epilayers excited with the blue line of the HeCd-laser ($E_L = 2.81$ eV). The solid lines are Gaussian line—shape fits to the experimental data. For the spectrum of the c-$In_{0.07}Ga_{0.93}N$ sample at 300 K, a superposition of two Gaussian functions is used for the fitting (- - -).

(arrows in Figure 9.69) can be estimated from the difference in the measured PL peak energy (dotted lines through the full circles) and the extrapolated gap energy of the c-$In_{0.8}Ga_{0.2}N$ alloy. The values of ΔE decrease from 0.453 eV to 0.326 eV if the x-value increase from 0.07 to 0.33, respectively. Because the In-content of the In-rich QDs does not chance in the different c-$In_xGa_{1-x}N$ epilayers the variation of ΔE can be explained only by a variation of the QD size, indicating an increase of QD size with increasing x

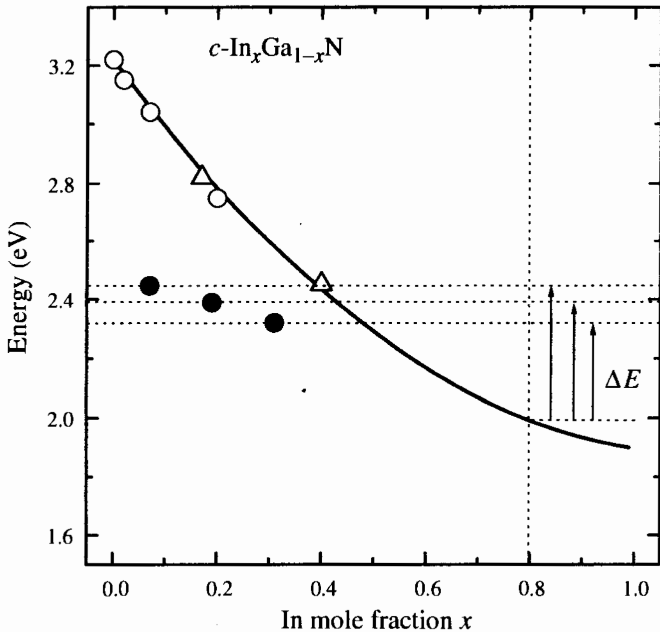

Figure 9.69 PL-emission energy (•) versus In molar fraction for c-In$_x$Ga$_{1-x}$N at 300 K. The open circles (○) are measurements of the energy gap of the c-In$_x$Ga$_{1-x}$N by spectroscopic ellipsometry [274], and the triangles are experimental data taken from Müllhäuser et al. [276]. The solid line is a parabolic fit to the experimental data. The dashed lines indicate the QD confinement energies, ΔE.

value. Assuming the presence of spherically shaped QDs, the confinement energy, ΔE, is directly related to its radius, R [291,292]. For infinite potential barriers and with $m_e^* = 0.16$ and $m_h^* = 0.84$ for the c-In$_{0.8}$Ga$_{0.2}$N effective masses [40] the radius of the QDs is estimated to vary between 3 nm and 4 nm. The origin of the luminescence of these epilayers is therefore best described as emission from QDs of approximately constant composition ($x \cong 0.8$) and with a radius that increases monotonically with the average In content of the layers.

9.8.7 In: An Ideal Surfactant?

Among the possible candidates to play the role of a surfactant for GaN during growth, In appears attractive due to its low sticking coefficient at the GaN growth temperature of about 700 °C. In fact, in hexagonal GaN several improvements in the quality of epilayers has been reported due to the presence of In. Improvements have been observed in the morphology (smoother surfaces), structural properties (decrease of the FWHM of ω-scans) [293], optical properties (the PL intensities increased, the PL

linewidths became narrower, the spatial distribution of luminescence became more homogeneous) [294,295], and electrical properties (free carrier mobility has increased, ideality factor of n-type Schottky diodes improved from 1.2 to 1.03, saturation current could be reduced by two orders of magnitude, and the formation of deep levels has been effectively suppressed) [296]. It has further been found that the presence of In modifies the diffusion kinetics in the growing GaN surface, leading to the observation of persistent RHEED intensity oscillations, which are characteristic of layer-by-layer growth [297].

Concerning the cubic phase of GaN, thus far only a few investigations have been performed to study the surfactant effects of In. By comparing In-doped cubic GaN with nominally undoped c-GaN on GaAs substrates, In-doped samples exhibit smoother surfaces and AFM measurements showed an improvement of rms roughness by a factor of 2. HRXRD measurements further indicate an narrowing of the FWHM in the ω-scans by a factor of about 0.8, whereas the FWHM in the $\omega - 2\Theta$ scan is within experimental error. Therefore, the presence of In seems to increase the diffusion length of the adatoms during c-GaN growth and reduces the formation of stacking faults. Furthermore, the integrated PL efficiency is higher than that of nominally undoped c-GaN samples. However, currently it is not clear if these improvements are due to the better crystallinity or to higher free carrier concentration as measured by Hall measurements. As noted earlier, the electron concentration measured at room temperature is in the order of 10^{18} cm^{-3}, which implies that at least in the cubic phase, In is either electrically active or introduces impurities that act as donors. At sufficiently high growth temperature, In acts as a surfactant in both cubic and hexagonal phases. It modifies the growth kinetics, resulting in improved structural and optical properties. However, it must be clarified if isoelectronic doping by In introduces donor levels in the forbidden energy gap of c-GaN.

Recently, Adelmann and colleagues [298] studied the kinetics change in the growth of c-GaN on thick 3C-SiC substrates by the presence of In segregated on the surface in situ by using RHEED oscillations. A growth rate increase has been observed in the N-rich regime, whereas no such an effect could be measured in the Ga-rich regime. These researchers explain this increase in growth rate as due to the fact that In should delay the Ga droplet formation, resulting in more Ga available for growth. They further observed that the effect of In is drastically dependent on the surface structure, that is, (0001) hexagonal or (001) cubic. Hexagonal and cubic surfaces behave quite differently, possibly due to the difference in the number of dangling bonds for N or Ga, depending on the surface under consideration. Their results also suggest that the sticking coefficient and/or the desorption probability of N atoms are thermally activated in both hexagonal and cubic case but with a rather different activation energy value.

9.9 GROWTH AND CHARACTERIZATION OF MBE GROWN CUBIC $Al_yGa_{1-y}N$

The primary interest in the $Al_yGa_{1-y}N$ alloy stems from the fact that advanced optoelectronic and electronic $Al_yGa_{1-y}N$/GaN-based devices can be fabricated. $Al_yGa_{1-y}N$ is used for cladding layers in LEDs and LDs. $Al_yGa_{1-y}N$/GaN HEMTs and heterojunction bipolar transistors (HBTs) are subjects of intense recent investigation and have emerged as attractive candidates for high-voltage, high-power operation at microwave frequencies [299]. However, hexagonal $Al_yGa_{1-y}N$/GaN heterostructures show an inherently strong spontaneous polarization oriented along the hexagonal c-axis as well as on strain-induced PZ polarisation. Such polarization-induced electric fields in strained QWs can cause the spatial separation of electrons and holes, resulting in a severe reduction of optical recombination efficiency. These PZ effects can be avoided by using the metastable cubic modifications of $Al_yGa_{1-y}N$ and GaN if they are grown in (001) direction [300]. Therefore, simplified design rules and improved optical performances are expected for both optoelectronic and electronic devices by making use of the zincblende structure.

9.9.1 Growth of Cubic $Al_yGa_{1-y}N$

In order to study their stuctural, optical, and electrical properties, cubic $Al_yGa_{1-y}N$/GaN films ($0.07 < y < 0.20$) were grown on GaAs (001) substrates by RF-plasma-assisted MBE. On top of a 350-nm-thick c-GaN layer, a 400-nm-thick c-$Al_yGa_{1-y}N$ film was deposited at a higher growth temperature of $T = 835\,°C$. The growth rate of c-$Al_yGa_{1-y}N$ was about 80 nm/hr. During deposition, the surface phase was continuously monitored by RHEED and the diffraction patterns exhibit a cubic symmetry along all major azimuths. For the $Al_yGa_{1-y}N$ growth, the Ga-flux has been adjusted to keep a c-(2×2) (Ga-stabilized) surface reconstruction pattern.

RBS experiments were performed for a precise determination of the Al content in the samples independent from lattice parameters and strain effects. The layer thickness and the Al concentration in the samples were estimated from the backscattered yield of a randomly oriented sample [127]. A 2.0 meV $^4He^+$ beam at a beam current of about 12 nA with a backscattering angle of 165° was used for data acquisition, and the measurements were evaluated with the program RUMP [129]. Figure 9.70 shows the normalized yield versus channel number, which is linearly correlated to the energy of the scattered ions. From the RUMP simulation (solid line in Figure 9.70) the thicknesses of the GaN and $Al_yGa_{1-y}N$ epilayers are determined to be 320 nm and 440 nm, respectively, and the Al content is estimated to be 12 percent. The interfacial regions of GaAs/GaN and GaN/$Al_{0.12}Ga_{0.88}N$ are

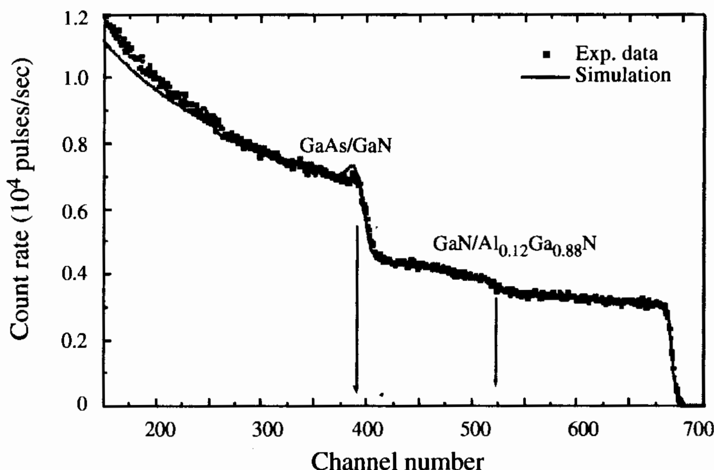

Figure 9.70 RBS of a $Al_{0.12}Ga_{0.88}N$/GaN/GaAs heterostructure measured in random orientation. The full squares are experimental data, the solid line is a calculated using the simulation program RUMP [129].

clearly resolved and marked by arrows in Figure 9.70. The RBS simulation reveals a homogenous distribution of the Al atoms in the $Al_yGa_{1-y}N$ layer.

A linear relation is found between the Al content in the epilayers as measured by RBS and XRD and the ratio of the elemental Al-flux J_{Al} to the sum of the group III-fluxes ($J_{Al}/(J_{Al} + J_{Ga})$). In addition, *c*-GaN can further be grown at 835 °C at the same high growth temperature as *c*-$Al_yGa_{1-y}N$. This ensures well-controllable and reproducible fabrication of the desired *c*-$Al_yGa_{1-y}N$/GaN heterostructures.

9.9.2 Structural and Vibrational Properties

The cubic nature and crystalline quality of the *c*-$Al_yGa_{1-y}N$/GaN layers were verified by HRXRD experiments. Figure 9.71 shows $\omega - 2\Theta$-scans along the symmetric (002) and asymmetric (113) reflexes of the *c*-$Al_xGa_{1-x}N$/GaN layers. All spectra can be well-fitted by two pseudo-Voigt functions. The peaks at $2\Theta = 39.9°$ and $69.1°$ are the (002) and (113) reflexes from the underlying GaN buffer layer. The peaks at higher Bragg angles are attributed to the ternary *c*-$Al_yGa_{1-y}N$ alloy having a smaller lattice constant. The Al content y was determined by computing the relative shift of the *c*-$Al_yGa_{1-y}N$ Bragg peak with respect to the GaN peak applying Vegard's law and assuming fully relaxed layers taking $a_{GaN} = 0.452$ nm and $a_{AlN} = 0.438$ nm [301]. There is excellent agreement between the Al contents derived from RBS and HRXRD measurements. For a detailed structural investigation of the *c*-$Al_yGa_{1-y}N$ films space reciprocal space

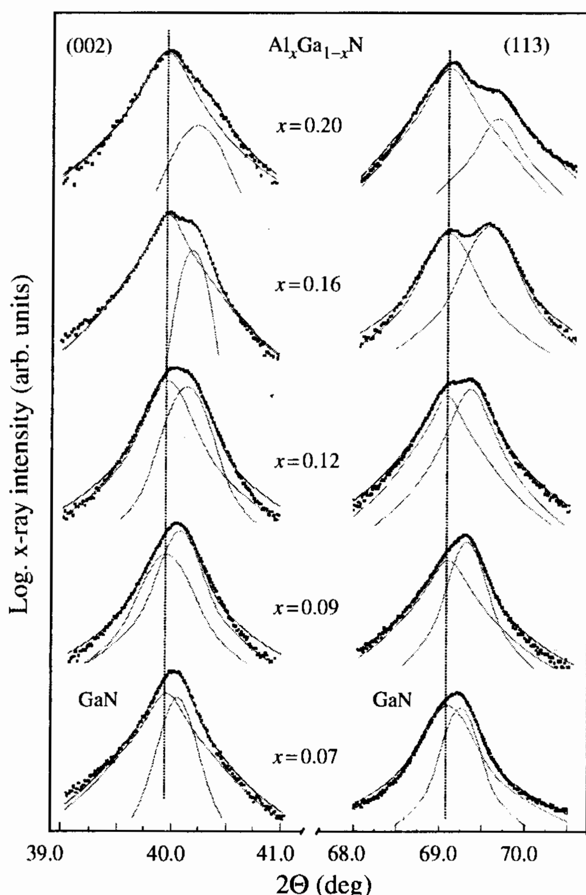

Figure 9.71 HRXRD $\omega - 2\Theta$-scans of the symmetric (002) and asymmetric (113) reflexes of c-GaN and c-$Al_yGa_{1-y}N$ layers with $0.07 < y < 0.20$.

map (RSM) are measured. Figure 9.72 displays the RSM of the (002) and (113) reflexes of a c-$Al_{0.16}Ga_{0.84}N$ sample. In the vicinity of the c-GaN (002) Bragg peak (top map), two reflexes can clearly by identified. The isointensity contours of the reflex with the highest intensity are centered at $q_{\parallel} = 0\,\text{Å}^{-1}$, $q_{\perp} = 2.785\,\text{Å}^{-1}$ and stem from cubic GaN. The second reflex at a position of $q_{\parallel} = 0\,\text{Å}^{-1}$, $q_{\perp} = 2.792\,\text{Å}^{-1}$ is that of the $Al_{0.16}Ga_{0.84}N$ layer. The FWHM of both reflexes is indicated by arrows of the respective peaks. The FWHM of the c-$Al_{0.16}Ga_{0.84}N$ and c-GaN peaks are almost identical, indicating a comparably good structural layer quality of the ternary alloy. For the asymmetric (113) reflexes, again two intensity maxima are clearly resolved (bottom map). The c-GaN and c-$Al_{0.16}Ga_{0.84}N$

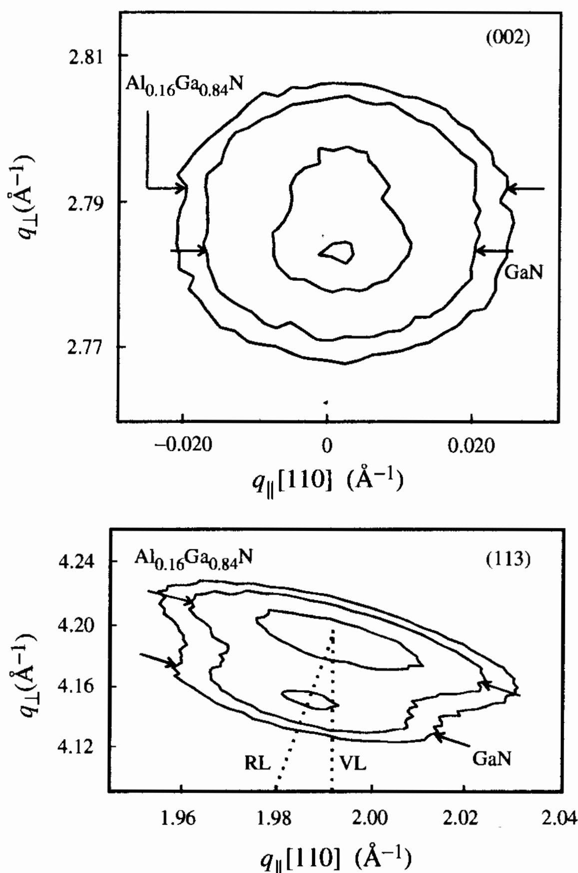

Figure 9.72 Reciprocal space map of the symmetric (002) and asymmetric (113) reflexes of the *c*-$Al_{0.16}Ga_{0.84}N$ epilayer. The arrows indicate the FWHM of the *c*-GaN and *c*-$Al_{0.16}Ga_{0.84}N$ peaks.

peaks are positioned at $q_{\|} = 1.995\ Å^{-1}$, $q_{\perp} = 4.20\ Å^{-1}$ and $q_{\|} = 1.99\ Å^{-1}$, $q_{\perp} = 4.15\ Å^{-1}$, respectively. The maximum intensity of the *c*-$Al_{0.16}Ga_{0.84}N$ reflex lies on a straight line pointing to the origin of reciprocal space (000), revealing that the 440-nm-thick *c*-$Al_{0.16}Ga_{0.84}N$ layer is totally relaxed. This observation is in agreement with a theoretical calculated value of the critical layer thickness, h_c, using a modified Matthews and Blakeslee model [302] given by Sherwin and colleagues [301]. The equation for the critical film thickness, h_c, is given by:

$$h_c = \frac{a(1-\nu/4)}{4\sqrt{2\pi}(1+\nu)\varepsilon}\left[\ln\left(\frac{\sqrt{2}h_c}{a}\right)+\Theta\right]$$

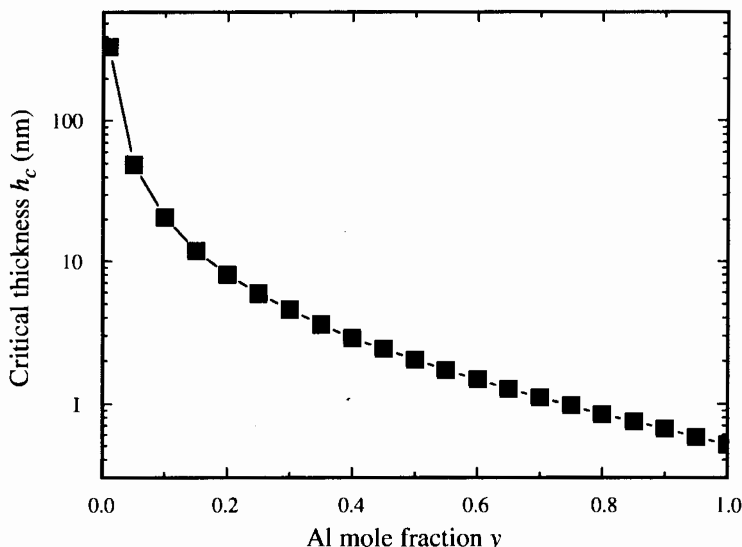

Figure 9.73 Critical layer thickness, h_c, versus Al mole fraction calculated for a single overlayer of c-$Al_yGa_{1-y}N$ on a c-GaN substrate using the equation given by Sherwin et al. [301].

where h_c is the film thickness, a is the substrate lattice constant, ν is the Poisson ratio, $\varepsilon = (a_{Al_yGa_{1-y}N} - a_{GaN})/a_{Al_yGa_{1-y}N}$ is the strain present in the film, and $\Theta \approx 1$ represents the dislocation core energy. For the c-$Al_{0.16}Ga_{0.84}N$, alloy grown on c-GaN, a value of about 11 nm is estimated for h_c. Figure 9.73 shows the dependence of the critical thickness h_c on the Al-mole fraction for c-$Al_yGa_{1-y}N$ on c-GaN substrates. According to this theoretical model, all of our c-$Al_yGa_{1-y}N$ layers with $0.07 < y < 0.20$ are well above the critical layer thickness and are therefore relaxed.

The vibrational properties of the c-$Al_yGa_{1-y}N$ layers have been studied by micro-Raman experiments at room temperature using the 514 nm line of an Ar-ion laser for excitation and keeping the power below 30 mW. The measurements are performed in backscattering geometry with a spectral resolution of about 5 cm^{-1}. Figure 9.74 displays the Raman spectra of various c-$Al_yGa_{1-y}N$/c-GaN samples. One can clearly see that a peak at about 555 cm^{-1} shifts to higher wavenumbers with increasing Al content. A similar effect is suggested above 730 cm^{-1} for a second peak. Both peak positions are indicated in the figure by arrows. The dotted lines correspond to the TO_{GaN} (555 cm^{-1}) and LO_{GaN} (740 cm^{-1}) modes of pure cubic GaN epilayers. A broad band ranging from the GaN TO to the LO phonon frequency dominates the spectra. Because Hall measurements gave a free electron concentration of 2×10^{20} cm^{-3} in these c-$Al_yGa_{1-y}N$ layers, it has been proposed that the broad structure in the Raman spectra is due

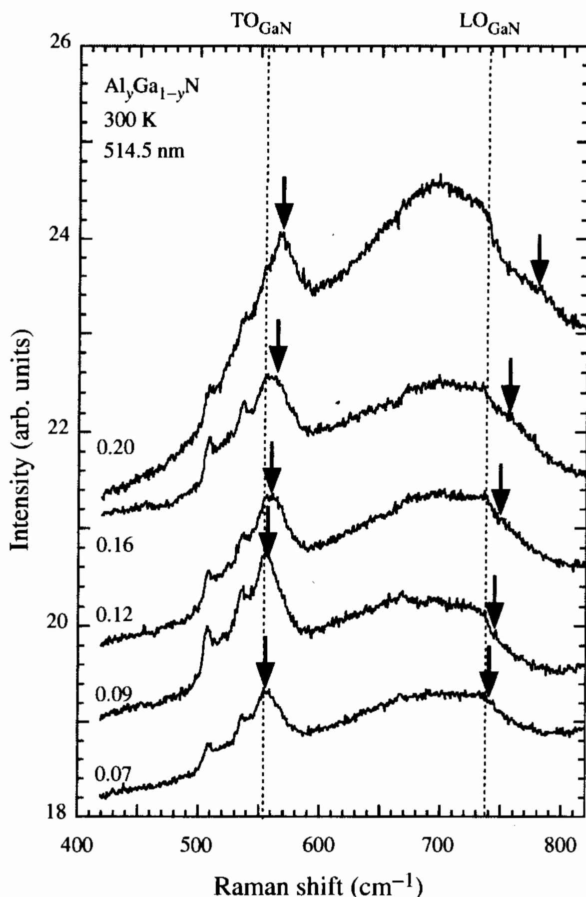

Figure 9.74 Raman spectra of various cubic $Al_yGa_{1-y}N$/*c*-GaN epilayers grown by MBE on GaAs(001) substrates. The spectra are excited by the 514 nm Ar^+-laser line and are measured at room temperature. The spectra are shifted upward for better representation.

an overdamped excitation of the free electron gas, similiar to the behavior observed by Ramsteiner and coworkers [303] in *n*-type *c*-GaN.

The peak frequencies indicated by arrows in Figure 9.74, are plotted versus the Al content in Figure 9.75 (full squares and full triangles). For the cubic $Al_yGa_{1-y}N$ alloy, theoretical calculations propose a one-mode- and two-mode-type behavior for the LO and TO modes, respectively [272]. The two-mode behavior of the TO phonon is a result of different vibrating masses, whereas the one-mode behavior of the LO phonon can be explained by the relatively small mass of the common anion nitorgen. The solid lines in Figure 9.75 represent the results of the theoretical calculations and, within

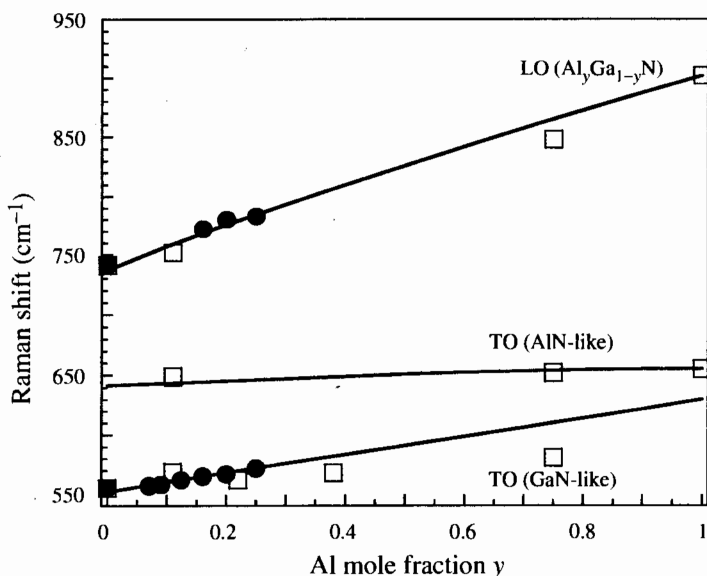

Figure 9.75 Raman shift of the TO and LO phonon modes of cubic $Al_yGa_{1-y}N$ versus Al mole fraction y. The full symbols are the experimental data indicated in Figure 9.4 by arrows. The solid lines represent the results of theoretical calculations [272] and the open circles are experimental data from Ramsteiner et al. [303], respectively.

experimental error, they agree with the experimental data (full circles). Based on the theoretical model, the high-frequency peak is attributed to the LO-mode of the cubic $Al_yGa_{1-y}N$ alloy and the low-frequency peak to the GaN-like TO-mode. Unfortunately, the AlN-like TO-mode at about $643\,cm^{-1}$ could not be observed because it is totally decorated by the strong contribution of the overdamped excitation of the free electron gas. However, recently reports of Raman measurements of cubic $Al_yGa_{1-y}N$ alloy grown by gas-source MBE on thick 3C-SiC epilayers [304], confirm the two-mode-type of TO-phonon and are shown in Figure 9.75 as open squares.

9.9.3 Optical and Electrical Properties

Spectroscopic ellipsometry (SE) was used to measure the dielectric properties of cubic $Al_yGa_{1-y}N$ epilayers at room temperature. In Figure 9.76 the refraction index and the extinction coefficient of c-GaN, c-$Al_{0.07}Ga_{0.93}N$, and c-$Al_{0.2}Ga_{0.8}N$ are plotted versus photon energy. With increasing Al content, a clear shift to higher energies is observed, indicating an increase of the energy of the fundamental absorption bandgap, E_{abs}. The corresponding E_{abs} values are marked by arrows in Figure 9.76. In addition, with increasing

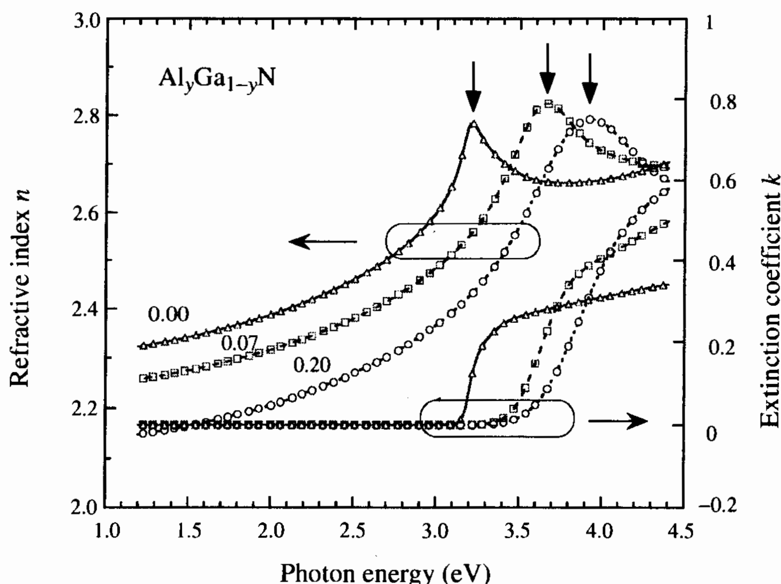

Figure 9.76 Refractive index and extinction coefficient of cubic $Al_yGa_{1-y}N$ with $y = 0$ (△), 0.07 (□), and 0.2 (○) as a function of the photon energy.

Al content, the structure at the gap energy range is less pronounced and becomes broader. This broadening is probably caused by increased alloy scattering and compositional fluctuations.

Figure 9.77 shows room-temperature CL-spectra of various c-$Al_yGa_{1-y}N$ alloys excited by a 5 keV e-beam and a current of 150 mA. The CL-spectra of these alloys are dominated by a broad-emission band, whose peak position shifts to higher energies with increasing y value. The FWHM of the luminescence bands are 300 meV and 500 meV for the $Al_{0.07}Ga_{0.93}N$ and the $Al_{0.2}Ga_{0.8}N$ epilayers, respectively. Enhanced alloy broadening and band-filling due to high free carrier concentrations may be the reasons for the broad structures observed. The fundamental absorption bandgap, E_{abs}, as measured by SE, is also included in Figure 9.77 and it is positioned at the high energy slope of the CL-spectra. On the low energy side of all spectra a weak emission at about 3.2 eV is measured, which is independent of the Al content and is therefore attributed to the underlaying c-GaN epilayer. The overall CL intensity decreases with increasing Al content, indicating an enhanced incorporation of nonradiative recombination centers at higher y values. Similar observations were reported by Nakadeira and Tanaka [305] for MOCVD-grown cubic $Al_yGa_{1-y}N$ epilayers.

Hall effect measurements between 15 K and 350 K show that all the c-$Al_yGa_{1-y}N$ samples are degenerated with free electron concentrations

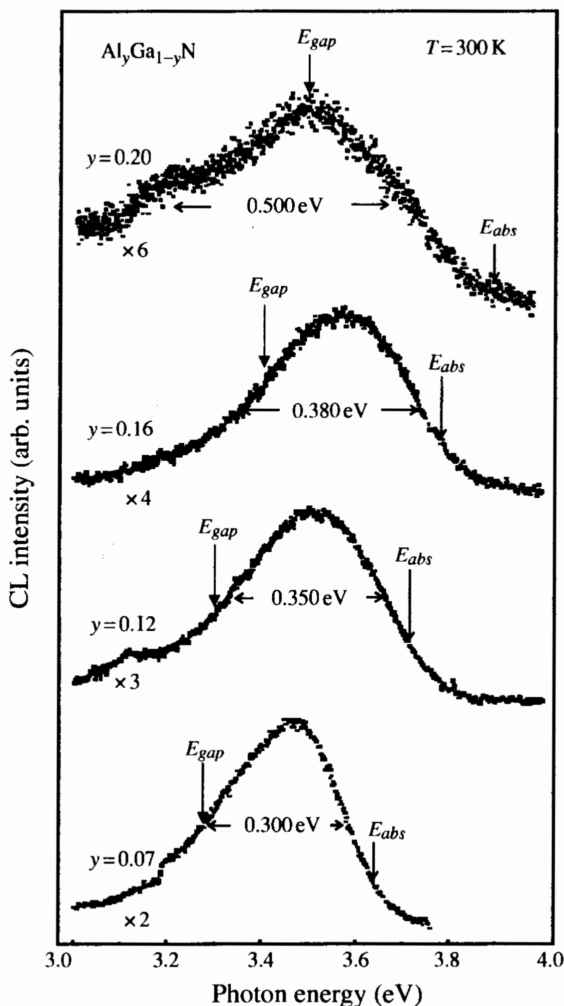

Figure 9.77 CL spectra of various cubic $Al_yGa_{1-y}N$ epilayers measured at room temperature (e-beam: 5 keV, 150 mA). The arrows indicate the enegy gap, E_{gap}, and E_{abs} measured by spectroscopic ellipsometry for various alloys. The spectra have been shifted upward for clarity.

of about 10^{20} cm^{-3} and mobilites of about 20 cm^2/Vs. Due to this high background carrier concentration, the Fermi energy is shifted into the conduction band and the optical properties measured by CL and SE are severely influenced by the Burstein-Moss shift (BMS) and bandgap renormalization (BGR). In a first approximation, the effect of the BGR can be approximated by the values measured in the heavily Si-doped *c*-GaN epilayers [19]. The position of the Fermi level in the conduction band can than be calculated

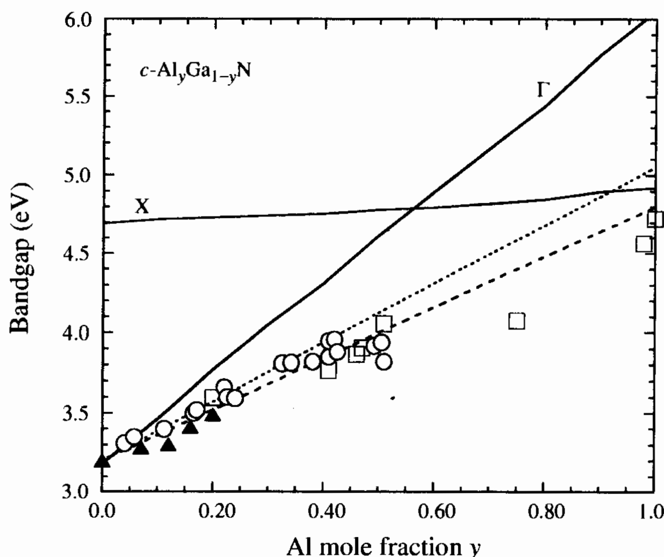

Figure 9.78 Bandgap versus Al mole fraction. The full triangles correspond to the values determined by the SE measurements after correction of the Burstein-Moss shift and the bandgap renormalization effect. The open squares and open circles and the dashed and dotted lines are data and linear relationships taken from References 305 and 306, respectively. The full lines are calculated values for the Γ and X bands for the cubic $Al_yGa_{1-y}N$ alloy [306].

using the measured free carrier concentration and the effective electron mass of pure *c*-GaN. By taking into account both effects, the bandgap, E_{gap}, at room temperature, which was derived from the SE data, is depicted by arrows in Figure 9.77.

Figure 9.78 depicts the estimated bandgap energy (full triangles) as a function of the Al mole fraction y. Within the experimental error, a linear increase of the bandgap energy with Al content is determined. This is in good agrees with experimental data recently published by Nakadaira and Tanaka [305] and Koizumi and colleagues [306], which are also indicated in Figure 9.78 by open circles and open squares, respectively. The dashed and dotted straight lines represent the corresponding linear dependences of $E_{gap}(y) = 3.20 + 1.85xy$ and $E_{gap}(y) = 3.20 + 1.6xy$. Theoretical calculations of the Γ and X band of *c*-$Al_yGa_{1-y}N$ [307] are plotted in Figure 9.78 as full lines. The theoretical predictions propose a direct-indirect transition at an Al content of about 0.57 and show a slope of E_{gap} versus y that is much steeper than the experimental data in the range $y < 0.5$. Because only a few data points were measured above an Al-mole fraction of 0.5, it is not clear if the direct-indirect transition really exists. Nakadaira and Tanaka [305] reported a decrease of the PL peak intensity for $y > 0.3$ of more than three

orders of magnitude, which may indicate that c-$Al_{0.51}Ga_{0.49}N$ has an indirect gap. However, no evidence supporting the direct-indirect conversion was found by Koizumi and coworkers [306] from CL data, although some ambiguity remains for the assignment of band-edge emission. To clarify the nature of the observed emission more precisely, further improvements of the epilayer quality and some kind of modulation spectroscopy, which is more sensitive to the band structure, are desirable.

9.10 CONCLUSIONS

The progress made in the field of the metastable cubic group III-nitrides has been remarkable, culminating in the realization of the first GaN p-n junction-based LEDs and opening the field of advanced optoelectronic devices in the near future. All the binary compounds (c-InN, c-GaN, c-AlN) and their alloys c-$In_xGa_{1-x}N$ and c-$Al_yGa_{1-x}N$ have been demonstrated to be producible in their metastable zincblende modification. Successful p-type and n-type doping of cubic GaN by Si and Mg has been performed.

Due to the ability to grow far from thermodynamic equilibrium, the MBE method has been predestinated to study the growth of the metastable cubic phases, and indeed, the MBE method has played a major role in the development of high-quality cubic group III-nitrides. Careful in situ control of the growth conditions was found to be necessary for growing phase-pure cubic group III-nitrides on several different cubic substrates like GaAs (001), GaP (001), 3C-SiC (001), and on nm-thin 3C-SiC–coated Si (001). These heteroepitaxial GaN epilayers contain a large amount of dislocations due to the large lattice-mismatch. Nevertheless, gain and stimulated emission experiments on cleaved c-GaN underline the possible application of this material for LDs with cleaved facets.

TEM, XRD, and RBS investigations of cubic GaN on GaAs (001) substrates show dislocation densities in the order 10^{11} cm^{-2}. XRD data clearly indicate a reduction of the density of dislocations with increasing epilayer thickness. However, from a practical point of view, the low growth rates in MBE prohibit the growth of epilayers so thick that the dislocation density is reduced below 10^8 cm^{-2}. Therefore, other methods, such as the insertion of low-temperature buffer layers of GaN, $In_xGa_{1-x}N$, and $Al_yGa_{1-y}N$, are necessary for a reduction in dislocations. This may be of absolute importance because different experiment results provide a clearer picture in which the dislocations in the cubic group III-nitrides are electrically active and clearly deleterious for transport properties. Acceptor-like states are introduced in the forbidden bandgap, and in p-n diodes the dislocations behave as current leakage pathways that severely reduce the overall efficiency of the optoelectronic cubic GaN devices. It remains unclear whether the dislocation-related acceptors are an intrinsic feature of dislocations in the nitrides, or if they

are caused by impurity segregation. Thus, the reduction of the dislocation density is now recognized to be one of the most important tasks for the improvement of cubic nitride devices.

The cubic alloy $In_xGa_{1-x}N$ shows spatial fluctuations of the composition and a tendency toward phase separation at higher In concentrations. Subband gap excitation and selective RRS on c-$In_xGa_{1-x}N$ has demonstrated that the light emitted near 2.4 eV is due to emission from QDs spontaneously formed from the In-rich phase separated by spinodal decomposition occurring in the epilayers. Both dot size and In-content fluctuations in the dots play an important role on the emission characteristics. A strong variation of the sticking coefficient of In with temperature complicates the epitaxial growth. However, the low sticking coefficient enables In to act as a surfactant in the c-GaN growth, improving the morphology, structural, optical, and electrical properties.

In cubic $Al_yGa_{1-y}N$, no phase separation has been observed. The Al sticking coefficient is almost constant with varying temperature. A linear increase of the energy gap of $Al_yGa_{1-y}N$ with Al content is found for $0 < y < 0.3$. The PL efficiency is decreasing with increasing y value, indicating an increased incorporation of nonradiative defects with increasing Al content. Although theoretical calculations propose a transition to an indirect gap semiconductor for c-$Al_yGa_{1-y}N$ at about $y \geq 0.45$, the experimental proof is still missing. To date, in MBE-grown c-$Al_yGa_{1-y}N$ a high background n-type doping, probably due to O, is found and it is expected that both controlled p-type and n-type doping of $Al_yGa_{1-y}N$ is more difficult due to an increase of the binding energies of donors and acceptors.

Within the last decade, the improvement in quality of several cubic group III-nitride epilayers has been encouraging, allowing the realization of low-dimensional structures in the near future. Recently, Daudin and colleagues [308] demonstrated the realization of cubic self-assembled GaN QDs by taking advantage of the Stranski-Krastanov growth mode of GaN on AlN/3C-SiC substrates. Because in c-III-nitrides the spontaneous polarization is zero, and in layers grown on (100) orientated substrates PZ fields are negligible, it is widely expected that advanced QW and QD structures of cubic group III-nitrides offer the possibility to avoid the deterimental influence of PZ effects on the optical properties.

In addition to MBE, more and more research groups also successfully apply MOCVD for the growth of cubic group III-nitrides on GaAs (001) substrates, paving the way for low-cost production in industrial manufacturing. In view of all the recent developments, cubic group III-nitride epilayers are revealing their prospective potential for future device applications and are an interesting alternative to hexagonal III-nitrides for the realization of cleaved LDs and hybrid high-temperature electronic devices on Si or GaAs substrates.

Acknowledgments

The author is much indebted to Prof. K. Lischka and Dr. D. Schikora at the University of Paderborn for their ongoing support and encouragement. I would like to thank a number of graduate students whose work is featured in this chapter: T. Frey, B. Schöttker, C. R. Wang, M. Bartels, J. Busch, A. Greiner, A. Khartchenko, U. Köhler, J. Kühler, A. Richter, A. Rüther, F. Schmilgus, U. Schramm, T. Simonsmeier, and S. Völlmeke. Technical and administrative support is acknowledged to B. Volmer, S. Igges, and I. Zimmermann. I further acknowledge the hospitality of Prof. J. R. Leite, Prof. Luisa M. R. Scolfaro, and their group (Dr. A. Tabata, Dr. A. P. Lima, E. Silveira, and R. Trentin) at the Universidade de São Paulo, Brazil, and Prof. V. Lemos (Universidade Estadual Campinas, Brazil) for several very impressive and fruitful research stays in Brazil. For excellent cooperation during the past years, I want to thank Prof. J. Mimkes, and M. Lübbers (University of Paderborn); Prof. A. Hoffmann, Prof. C. Thomsen, Dr. A. Goñi, Dr. L. Eckey, Dr. H. Siegle, J. Holst, A. Kaschner, and G. Kaczmarczyk (TU Berlin, Germany); Prof. B. K. Meyer, W. Kriegseis, and W. Burkhard (University of Giessen); Dr. R. Goldhahn, J. Schreiner, and S. Shokhovets (TU Ilmenau, Germany); Prof. J. Christen, Dr. H. Witte, M. Lisker, A. Krtschil (University of Magdeburg, Germany); and Prof. R. Brenn, J. Portmann and C. Haug (University of Freiburg, Germany). I gratefully acknowledge financial support of part of this work by the German science foundation agency DFG "Deutsche Forschungsgemeinschaft", VW-Stiftung, CAPES/DAAD/PROPAL project within the Brazil/Germany scientific collaboration program, and the "Forschungsreserve" of the Physics Department at the University of Paderborn.

References

1. J. W. Orton and C. T. Foxon, *Rep. Prog. Phys.*, **61**, 1 (1998).
2. S. Strite and H. Morkoc, *J. Vac. Sci. Technol.*, **B10**, 1237 (1992).
3. O. Brandt, J. R. Müllhäuser, B. Yang, H. Yang, and K. H. Ploog, *Physica*, **E2**, 532 (1998).
4. J. Holst, L. Eckey, A. Hoffmann, I. Broser, B. Schöttker, D. J. As, D. Schikora, and K. Lischka, *Appl. Phys. Lett.*, **72**(12), 1439 (1998).
5. H. Yang, L. X. Zheng, J. B. Li, X. J. Wang, D. P. Xu, Y. T. Wang, X. W. Hu, and P. D. Han, *Appl. Phys. Lett.*, **74**(17), 2498 (1999).
6. D. J. As, A. Richter, J. Busch, M. Lübbers, J. Mimkes, and K. Lischka, *Appl. Phys. Lett.*, **76**(1), 13 (2000).
7. H. Yang, O. Brandt, and K. Ploog, *Phys. Stat. Sol. (B)*, **194**, 109 (1996).
8. S. Nakamura and G. Fasol, in *The Blue Laser Diode* (Springer, Berlin, 1997).
9. D. Schikora, M. Hankeln, D. J. As, K. Lischka, T. Litz, A. Waag, T. Buhrow, and F. Henneberger, *Phys. Rev.*, **B54**(12), R8381 (1996).
10. D. J. As, F. Schmilgus, C. Wang, B. Schöttker, D. Schikora, and K. Lischka, *Appl. Phys. Lett.*, **70**(10), 1311 (1997).
11. S. Strite, D. Chandrasekhar, D. J. Smith, J. Sariel, H. Chen, N. Teraguchi, and H. Morkoc, *J. Cryst. Growth*, **127**, 204 (1993).

12. C. R. Abernathy, J. D. MacKenzie, S. R. Bharatan, K. S. Jones, and S. J. Pearton, *Appl. Phys. Lett.*, **66**(13), 1632 (1995).
13. B. Yang, O. Brandt, B. Jenichen, J. Müllhäuser, and K. H. Ploog, *J. Appl. Phys.*, **82**(4), 1918 (1997).
14. J. R. Müllhäuser, B. Jenichen, M. Wassermeier, O. Brandt, and K. H. Ploog, *Appl. Phys. Lett.*, **71**(7), 909 (1997).
15. E. Silveira, A. Tabata, J. R. Leite, R. Trentin, V. Lemos, T. Frey, D. J. As, D. Schikora, and K. Lischka, *Appl. Phys. Lett.*, **75**(23), 3602 (1999).
16. T. Frey, D. J. As, D. Schikora, K. Lischka, J. Holst, and A. Hoffmann, *Phys. Stat. Sol. (B)*, **216**, 259 (1999).
17. J. B. Li, H. Yang, L. X. Zheng, D. P. Xu, and Y. T. Wang, *MRS Symp. Proc.*, **537**, G3.25 (1999).
18. J. G. Kim, A. C. Frenkel, H. Liu, and R. M. Park, *Appl. Phys. Lett.*, **65**, 91 (1994).
19. D. J. As, A. Richter, J. Busch, B. Schöttker, M. Lübbers, J. Mimkes, D. Schikora, K. Lischka, W. Kriegseis, W. Burkhardt, and B. K. Meyer, *MRS Internet J. Nitride Semicond. Res.*, **5S1**, W3.81 (2000).
20. M. E. Lin, G. Xue, G. L. Zhou, J. E. Greene, and H. Morkoc, *Appl. Phys. Lett.*, **63**, 932 (1993).
21. D. J. As, T. Simonsmeier, B. Schöttker, T. Frey, D. Schikora, W. Kriegseis, W. Burkhardt, and B. K. Meyer, *Appl. Phys. Lett.*, **73**(13), 1835 (1998).
22. D. J. As, *Phys. Stat. Sol. (B)*, **210**, 445 (1998).
23. O. Brandt, H. Yang, H. Kostial, and K. H. Ploog, *Appl. Phys. Lett.*, **69**(18), 2707 (1996).
24. S. J. Pearton, GaN and Related Materials, in *Optoelectronic Properties of Semiconductors and Superlattices*, M. O. Manasreh, Series Ed. (Gordon and Breach, Amsterdam, 1997).
25. S. J. Pearton, GaN and Related Materials II, in *Optoelectronic Properties of Semiconductors and Superlattices*, M. O. Manasreh, Series Ed. (Gordon and Breach, Amsterdam, 1999).
26. B. Gil, *Group III Nitride Semiconductor Compounds—Physics and Applications* (Oxford University Press, Oxford, 1998).
27. J. H. Edgar, Properties of Group III Nitrides, emis, Datareviews Series, **11**, INSPEC (1994).
28. J. I. Pankove and T. D. Moustakas, Gallium Nitride (GaN) I, in *Semiconductors and Semimetals*, Vol. **50** (Academic Press, San Diego, 1998).
29. J. I. Pankove and T. D. Moustakas, Gallium Nitride (GaN) II, in *Semiconductors and Semimetals*, Vol. **57** (Academic Press, San Diego, 1999).
30. *MRS Internet J. Nitride Semicond. Res.*, http://nsr.mij.mrs.org.
31. W. J. Fan, M. F. Li, T. C. Chong, and J. B. Xia, *Sol. St. Commun.*, **97**(5), 381 (1996).
32. D. Vogel, P. Krüger, and J. Pollmann, *Phys. Rev. B*, **55**(19), 12836 (1997).
33. W. R. L. Lambrecht and B. Segall, in *Properties of Group III Nitrides*, Ed. by J. H. Edgar, emis Datareviews Series, **11**, INSPEC (1994), Ch. 4.
34. M. Suzuki and T. Uenoyama, in *Group III Nitride Semiconductor Compounds—Physics and Applications*, Ed. by B. Gil (Oxford University Press, 1998), Ch. 8.
35. Calculations performed using the method of Vogel et al. [32] by F. de Salla and F. Scholz, private communications.
36. W. J. Fan, M. F. Li, T. C. Chong, and J. B. Xia, *J. Appl. Phys.*, **79**(1), 188 (1996).
37. S. K. Pugh, D. J. Dugdale, S. Brand, and R. A. Abram, *J. Appl. Phys.*, **86**(7), 3768 (1999).
38. J. M. Luttinger and W. Kohn, *Phys. Rev.*, **97**, 869 (1955).
39. E. O. Kane, *J. Phys. Chem. Solids*, **1**, 249 (1957).
40. S. K. Pugh, D. J. Dugdale, S. Brand, and R. A. Abram, *Semicond. Sci. Technol.*, **14**(1), 23 (1999).
41. R. Enderlein, G. M. Sipahi, L. M. R. Scolfaro, and J. R. Leite, *Phys. Stat. Sol. (B)*, **206**, 623 (1998).
42. I. Petrov, E. Mojab, R. C. Powell, and J. E. Greene, *Appl. Phys. Lett.*, **60**, 2491 (1992).
43. T. Lei, M. Fanciulli, R. J. Molnar, T. D. Moustakas, R. J. Graham, and J. Scanlon, *Appl. Phys. Lett.*, **59**, 944 (1991).
44. S. Strite, D. Chandrasekhar, D. J. Smith, J. Sariel, H. Chen, N. Teraguchi, and H. Morkoc, *J. Cryst. Growth*, **127**, 204 (1993).

45. G. Ramirez-Flores, H. Navarro-Contreras, A. Lastras-Martinez, R. C. Powell, and J. E. Greene, *Phys. Rev.*, **B50**(12), 8433 (1994).
46. A. T. Meney, E. P. O'Reilly, and A. R. Adams, *Semicond. Sci. Technol.*, **11**, 897 (1996).
47. S. A. McGill, K. Cao, W. B. Fowler, and G. G. DeLeo, *Phys. Rev.*, **B57**(15), 8951 (1998).
48. C. G. Van de Walle and J. Neugebauer, *Appl. Phys. Lett.*, **70**(19), 2577 (1997).
49. K. Kim, W. R. L. Lambrecht, and B. Segall, *Phys. Rev.*, **B53**(24), 16310 (1996).
50. S. H. Park and S. L. Chuang, *J. Appl. Phys.*, **87**(1), 353 (2000).
51. H. Morkoc, *Nitride Semiconductors and Devices* (Springer, Berlin, 1999).
52. S. E. Hooper, C. T. Foxon, T. X. Cheng, L. C. Jenkins, D. E. Lacklison, J. W. Orton, T. Bestwick, A. Kean, M. Dawson, and G. Duggan, *J. Cryst. Growth*, **155**, 157 (1995).
53. H. Okumura, S. Misawa, and S. Yoshida, *Appl. Phys. Lett.*, **59**(9), 1059 (1991).
54. H. Okumura, K. Ohta, G. Feuillet, K. Balakrishnan, S. Chichibu, H. Hamaguchi, P. Hacke, and S. Yoshida, *J. Cryst. Growth*, **178**, 113 (1997).
55. S. Strite, J. Ruan, Z. Li, A. Salvador, H. Chen, D. J. Smith, W. J. Choyke, and H. Morkoc, *J. Vac. Sci. Technol. B*, **9**, 1924 (1991).
56. M. E. Lin, G. Xue, G. L. Zhou, and H. Morkoc, *Appl. Phys. Lett.*, **62**(26), 3479 (1993).
57. C. H. Hong, K. Wang, and D. Pavlides, *Inst. Phys. Conf. Ser. No.*, **141**, 107 (1994).
58. T. Lei, T. D. Moustakas, R. J. Graham, Y. He, and S. J. Berkowitz, *J. Appl. Phys.*, **71**(10), 4933 (1992).
59. Z. Sitar, M. J. Paiseley, B. Yan, and R. F. Davis, *MRS Symp. Proc.*, **162**, 2089 (1990).
60. K. Ploog, O. Brandt, H. Yang, B. Yang, and A. Trampert, *J. Vac. Sci. Technol. B*, **16**(4), 2229 (1998).
61. H. Liu, A. C. Frenkel, J. G. Kim, and R. M. Park, *J. Appl. Phys.*, **74**(10), 6124 (1993).
62. M. J. Paisely, Z. Sitar, J. B. Posthill, and R. F. Davis, *J. Vac. Sci. Technol. A*, **7**, 701 (1989).
63. H. Okumura, H. Hamaguchi, T. Koizumi, K. Balakrishnan, Y. Ishida, M. Arita, S. Chichibu, H. Nakanishi, T. Nagatomo, and S. Yoshida, *J. Cryst. Growth*, **189/190**, 390 (1998).
64. B. Daudin, G. Feuillet, J. Hübner, Y. Samson, F. Widmann, A. Philippe, C. Bru-Chevallier, G. Guillot, E. Bustarret, G. Bentoumi, and A. Deneuville, *J. Appl. Phys.*, **84**(4), 2295 (1998).
65. J. Wu, H. Yaguchi, H. Nagasawa, Y. Yamaguchi, K. Onabe, Y. Shiriki, and R. Ito, *J. Cryst. Growth*, **189/190**, 420 (1998).
66. A. Barski, U. Rössner, J. L. Rouviere, and M. Arlery, *MRS Internet J. Nitride Semicond. Res.*, **1**, 21 (1996).
67. Y. Hiroyama and M. Tamura, *Jpn. J. Appl. Phys.*, **37**, L630 (1998).
68. T. S. Cheng, L. C. Jenkins, S. E. Hooper, C. T. Foxon, J. W. Orton, and D. E. Lacklison, *Appl. Phys. Lett.*, **66**(12), 1509 (1995).
69. J. W. Orton, D. E. Lacklison, N. Baba-Ali, C. T. Foxon, T. S. Cheng, S. V. Novikov, D. F. C. Johnson, S. E. Hooper, L. C. Jenkins, L. J. Challis, and T. L. Tansley, *J. Electron. Mater.*, **24**, 263 (1995).
70. R. C. Powell, N. E. Lee, Y. W. Kim, and J. E. Greene, *J. Appl. Phys.*, **73**(1), 189 (1993).
71. J. I. Pankove, *MRS Symp. Proc.*, **97**, 409 (1987).
72. F. A. Ponce, in *Group III Nitride Semiconductor Compounds*, Ed. by B. Gil (Oxford Science, 1998), p. 122.
73. O. Briot, in *Group III Nitride Semiconductor Compounds*, Ed. by B. Gil (Oxford Science, 1998), p. 70.
74. G. Popovici, H. Morkoc, and S. N. Mohammad, in *Group III Nitride Semiconductor Compounds*, Ed. by B. Gil (Oxford Science, 1998), p. 19.
75. H. P. Maruska and J. J. Tietjen, *Appl. Phys. Lett.*, **15**, 367 (1969).
76. R. J. Molnar, *Semicond. Semimet.*, **57**, 1 (1999).
77. S. Nakamura, *Semicond. Semimet.*, **50**, 431 (1998).
78. S. P. DenBaars and S. Keller, *Semicond. Semimet.*, **50**, 11 (1998).
79. K. H. Ploog, in *Crystal Growth, Properties and Applications*, Vol. 3, H. C. Freyhard, Ed. (Berlin, Springer, 1980), p. 73.
80. E. H. C. Parker, *The Technology and Physics of Molecular Beam Epitaxy* (New York, Plenum, 1986).

81. C. T. Foxon and B. A. Joyce, in *Growth and Characterization of Semiconductors*, R. A. Stradling and P. C. Klipstein, Eds. (New York, Adam Hilger, 1990), p. 35.
82. M. Herrman and H. Sitter, in *Molecular Beam Epitaxy*, Vol. 7 (Springer, Berlin, 1989).
83. T. D. Moustakas, in *Semicond. Semimet.*, **57**, 33 (1999).
84. H. Tsuchiya, K. Sunaba, S. Yonemura, T. Suemasu, and F. Hasagawa, *Jpn. J. Appl. Phys. Lett.*, **36**, L1 (1997).
85. A. Yamaguchi, T. Manak, A. Sakai, H. Sunakawa, A. Kimura, M. Nido, and A. Usui, *Jpn. J. Appl. Phys. Lett.*, **35**, L873 (1996).
86. H. Tsuchiya, T. Okahisa, F. Hasagawa, H. Okumura, and S. Yoshida, *Jpn. J. Appl. Phys. Lett.*, **33**, 1747 (1994).
87. H. Tsuchiya, M. Akamatsu, M. Ishida, and F. Hasagawa, *Jpn. J. Appl. Phys. Lett.*, **35**, L748 (1996).
88. H. M. Manasevit, *Appl. Phys. Lett.*, **12**, 156 (1968).
89. H. Amano, N. Sawaki, I. Akasaki, and Y. Toyoda, *Appl. Phys. Lett.*, **48**(5), 353 (1986).
90. A. Nakadeira and H. Tanaka, *Appl. Phys. Lett.*, **70**(20), 2720 (1997).
91. J. Wu, H. Yaguchi, K. Onabe, R. Ito, and Y. Shiraki, *Appl. Phys. Lett.*, **71**(15), 2067 (1997).
92. J. Wu, H. Yaguchi, K. Onabe, and Y. Shiraki, *Appl. Phys. Lett.*, **73**(14), 1931 (1998).
93. J. Wu, H. Yaguchi, H. Nagasawa, Y. Yamaguchi, K. Onabe, Y. Shiraki, and R. Ito, *Jpn. J. Appl. Phys.*, **36**, 4241 (1997).
94. A. Nakadaira and H. Tanaka, *Phys. Stat. Sol. (A)*, **176**, 529 (1999).
95. D. P. Xu, H. Yang, L. X. Zheng, X. J. Wang, L. H. Duan, and R. H. Wu, *J. Cryst. Growth*, **191**, 646 (1998).
96. H. Amano, M. Kito, K. Hiramatsu, and I. Akasaki, *Jpn. J. Appl. Phys.*, **28**, L2112 (1989).
97. S. Nakamura, M. Senoh, and T. Mukai, *Jpn. J. Appl. Phys.*, **30**(10A), L1708 (1991).
98. H. Tanaka and A. Nakadaira, Proc. of the 2nd Int. Symp. on Blue Laser and Light Emitting Diodes, Ohmusha, Lts., Tokyo, 669 (1998).
99. Z. Yang, L. K. Li, and W. 1. Wang, *J. Vac. Sci. Technol. B*, **14**, 2354 (1996)
100. W. Kim, A. Salvator, A. E. Bothkarev, O. Aktas, S. N. Mohammed, and H. Morkoc, *Appl. Phys. Lett.*, **69**(14), 559 (1996).
101. C. R. Abernathy, in *GaN and Related Materials*, Ed. by S. J. Pearton, *Optoelectronic Properties of Semiconductors and Superlattices*, Vol. 2 (Gordon and Breach, Amsterdam, 1997), p. 11.
102. C. R. Abernathy, J. D. Mackenzie, and S. M. Donovan, *J. Cryst. Growth*, **178**, 74 (1997).
103. H. Okumura, S. Misawa, T. Okahisa, and S. Yoshida, *J. Cryst. Growth*, **136**, 361 (1994).
104. O. Brandt, H. Yang, B. Jenichen, Y. Suzuki, L. Däweritz, and K. H. Ploog, *Phys. Rev. B*, **52**(4), R2253 (1995).
105. T. H. Myers, M. R. Millecchia, A. J. Ptak, K. S. Ziemer, and C. D. Stinespring, *J. Vac. Sci. Technol. B*, **17**(4), 1654 (1999).
106. N. Newman, in *Semiconductors and Semimetals*, Vol. 50 (Academic, New York, 1998), p. 55.
107. D. J. As, D. Schikora, A. Greiner, M. Lübbers, J. Mimkes, and K. Lischka, *Phys. Rev. B*, **54**(16), R11118 (1996).
108. S. Yoshida, H. Okumura, G. Feuillet, P. Hacke, and K. Balakrishnan, *MRS Symp. Proc.*, **449**, 173 (1997).
109. O. Brandt, H. Yang, and K. Ploog, *Phys. Rev. B*, **54**(7), 4432 (1996).
110. H. Siegle, L. Eckey, A. Hoffmann, C. Thomsen, B. K. Meyer, D. Schikora, and K. Lischka, *Solid State Commun.*, **96**(12), 943 (1995).
111. J. Menninger, U. Jahn, O. Brandt, H. Yang, and K. H. Ploog, *Phys. Rev. B*, **53**, 1881 (1996).
112. A. P. Lima, T. Frey, U. Köhler, C. Wang, D. J. As, B. Schöttker, K. Lischka, and D. Schikora, *J. Cryst. Growth*, **197**, 31 (1999).
113. B. Schöttker, J. Kühler, D. J. As, D. Schikora, and K. Lischka, *Mater. Sci. For.*, **264–268**, 1173 (1998).
114. H. Yang, O. Brandt, M. Wassermaier, J. Behrend, H. P. Schönherr, and K. H. Ploog, *Appl. Phys. Lett.*, **68**(2), 244 (1996).

115. T. Lei, K. F. Ludwig, and T. D. Moustakas, *J. Appl. Phys.*, **74**(7), 4430 (1993).
116. A. Tabata, R. Enderlein, J. R. Leite, S. W. da Silva, J. C. Galzerani, D. Schikora, M. Kloidt, and K. Lischka, *J. Appl. Phys.*, **79**(8), 4137 (1996).
117. I. Loa, S. Gronemeyer, C. Thomsen, O. Ambacher, D. Schikora, and D. J. As, *J. Raman Spectroscopy*, **29**, 291 (1998).
118. K. H. Ploog, O. Brandt, H. Yang, and A. Tampert, *Thin Solid Films*, **306**, 231 (1997).
119. A. Trampert, O. Brandt, H. Yang, and K. H. Ploog, *Appl. Phys. Lett.*, **70**(5), 583 (1997).
120. J. W. Matthews, in *Epitaxial Growth*, Ed. by J. W. Matthews (Academic Press, New York, 1975), Part B, p. 560.
121. O. Brandt, H. Yang, A. Tampert, and K. H. Ploog, *MRS Symp. Proc.*, **395**, 27 (1996).
122. S. Ruvimov, Z. Lilliental-Weber, J. Washburn, T. J. Drummond, M. Hafich, and S. R. Lee, *Appl. Phys. Lett.*, **71**(20), 2931 (1997).
123. K. Lischka, *Phys. Stat. Sol. (B)*, **202**, 673 (1997).
124. H. Yang, O. Brandt, and K. Ploog, *J. Electr. Mat.*, **25**(5), 787 (1996).
125. J. E. Ayers, *J. Appl. Phys.*, **78**, 3724 (1995).
126. M. D. McCluskey, C. G. Van de Walle, C. P. Master, L. T. Romano, and N. M. Johnson, *Appl. Phys. Lett.*, **72**(21), 2725 (1998).
127. J. Portmann, C. Haug, R. Brenn, T. Frey, B. Schöttker, and D. J. As, *Nucl. Inst. Meth.*, **B155**, 489 (1999).
128. P. Blood, L. C. Feldman, G. L. Miller, and J. P. Remeika, *Nucl. Instr. Meth.*, **149**, 225 (1978).
129. RUMP(program), Computer Graphic Service, 52 Genung Circle, Ithaca, NY 14850-2042, USA.
130. J. Lindhard, *Mat.-Fys. Medd.: K. Dan. Vidensk. Selsk.*, **34**, 14 (1965).
131. J. H. Barret, *Phys. Rev.*, **B3**, 1527 (1971).
132. L. C. Feldman, J. W. Mayer, and S. T. Picraux, in *Materials Analysis by Ion Channeling* (Academic Press, New York, 1982).
133. J. Petalas, S. Logothetidis, S. Boultadakis, M. Alouani, and J. M. Wills, *Phys. Rev.*, **B52**, 8082 (1995).
134. E. Lin, B. N. Sverdlov, S. Strite, H. Morkoc, and A. E. Drakin, *Electron. Lett.*, **29**, 1759 (1993).
135. A. Vidal, G. Ramirez-Flores, H. Navarro-Contreras, A. Lastras-Martinez, R. C. Powell, and J. E. Greene, *Appl. Phys. Lett.*, **68**(4), 441 (1996).
136. I. Ohlidal, K. Navratil, and F. Lukes, *Surface Sci.*, **45**, 91 (1974).
137. I. Franz and W. Langheinrich, *Solid-State Electron.*, **13**, 807 (1970).
138. S. Shokhovets, R. Goldhahn, G. Gobsch, T. S. Cheng, C. T. Foxon, G. D. Kipshidze, and W. Richter, *J. Appl. Phys.*, **86**(5), 2602 (1999).
139. U. Köhler, D. J. As, B. Schöttker, T. Frey, K. Lischka, J. Scheiner, S. Shokhovets, and R. Goldhahn, *J. Appl. Phys.*, **85**(1), 404 (1999).
140. C. Wetzel, S. Fischer, J. Krüger, E. E. Haller, R. J. Molnar, T. D. Moustakas, E. N. Mokhov, and P. G. Baranov, *Appl. Phys. Lett.*, **68**(18), 2556 (1996).
141. N. N. Zinov'ev, A. V. Andrianov, B. Y. Averbukh, I. D. Yaroshetskii, T. S. Cheng, L. C. Jenkins, S. E. Hooper, C. T. Foxon, and J. W. Orton, *Semicond. Sci. Technol.*, **10**, 1117 (1995).
142. Z. X. Liu, A. R. Goñi, K. Syassen, H. Siegle, C. Thomsen, B. Schöttker, D. J. As, and D. Schikora, *J. Appl. Phys.*, **86**(2), 929 (1999).
143. J. R. Haynes, *Phys. Rev. Lett.*, **4**(7), 361 (1960).
144. C. Merz, M. Kunzer, U. Kaufmann, I. Akasaki, and H. Amano, *Semicond. Sci. Technol.*, **11**, 712 (1996).
145. Z. X. Liu, K. P. Korona, K. Syassen, J. Kuhl, K. Pakula, J. M. Baranowski, I. Grzegory, and S. Porowsky, *Solid State Commun.*, **108**, 433 (1998).
146. H. Siegle, A. R. Goñi, C. Thomsen, C. Ulrich, K. Syassen, B. Schöttker, D. J. As, and D. Schikora, *MRS Symp. Proc.*, **468**, 225 (1997).
147. C. Wang, D. J. As, B. Schöttker, D. Schikora, and K. Lischka, *Semicond. Sci. Technol.*, **14**, 161 (1999).
148. D. B. Holt and B. G. Yacobi, *SEM Micro-Characterization of Semiconductors, Techniques of Physics*, Eds. D. B. Holt and D. C. Joy (Academic Press, New York, 1989), p. 374.

149. W. Grieshaber, E. F. Schubert, I. D. Goepfert, R. F. Karlicek, Jr., M. J. Schurman, and C. Tran, *J. Appl. Phys.*, **80**(8), 4615 (1996).
150. A. Hoffmann, *Advan. Solid State Phys.*, **36**, 33 (1997).
151. K. L. Shaklee, R. E. Nahory, and R. F. Leheny, *J. Lumin.*, **7**, 284 (1973).
152. J. Holst, A. Hoffmann, I. Broser, B. Schöttker, D. J. As, D. Schikora, and K. Lischka, *Appl. Phys. Lett.*, **74**(14), 1966 (1999).
153. L. Eckey, J. Holst, A. Hoffmann, I. Broser, H. Amano, I. Akasaki, T. Detchprohm, and K. Hiramatsu, in *Proc. 23rd Int. Conf. Phys. Semicond.*, Ed. M. Scheffler and R. Zimmermann (World Scientific, Singapore, 1996), p. 286.
154. G. Lasher and F. Stern, *Phys. Rev. B*, **133**, A553 (1964).
155. J.-Chr. Holst, L. Eckey, A. Hoffmann, I. Broser, H. Amano, and I. Akasaki, *MRS Internet J. Nitride Semicond. Res.*, **2**, 25 (1997).
156. J. I. Pankove, *Optical Processes in Semiconductors* (Dover, New York, 1971).
157. I. K. Shmagin, J. F. Muth, R. M. Kolbas, S. Krishnankutty, S. Keller, U. K. Mishra, and S. P. DenBaars, *J. Appl. Phys.*, **81**(4), 2021 (1997).
158. H. H. Yang, T. J. Schmidt, W. Shan, J. J. Song, and B. Goldenberg, *Appl. Phys. Lett.*, **66**(1), 1 (1995).
159. A. Nakadaira and H. Tanaka, *Appl. Phys. Lett.*, **71**(6), 812 (1997).
160. M. Rubin, N. Newman, J. S. Chan, T. C. Fu, and J. T. Ross, *Appl. Phys. Lett.*, **64**(1), 64 (1994).
161. Y. Hayashi, T. Soga, M. Umeno, and T. Jimbo, *Physica B*, **272**, 256 (1999).
162. D. C. Look, in *Electrical Characterization of GaAs Materials and Devices* (Wiley, Chichester, 1989), p. 83.
163. T. Tanaka, A. Watanabe, H. Amano, Y. Kobayashi, I. Akasaki, S. Yamazaki, and M. Koike, *Appl. Phys. Lett.*, **65**(5), 593 (1994).
164. W. Kim, A. Salvador, A. E. Botchkarev, O. Aktas, S. N. Mohammad, and H. Morcoc, *Appl. Phys. Lett.*, **69**(4), 559 (1996).
165. P. Blood and J. W. Orton, in *The Electrical Characterization of Semiconductors: Majority Carriers and Electron States* (Academic Press, London, 1992).
166. D. L. Rode and D. K. Gaskill, *Appl. Phys. Lett.*, **66**(15), 1972 (1995).
167. W. Götz, N. M. Johnson, R. A. Street, H. Amano, and J. Akasaki, *Mat. Res. Soc. Symp. Proc.*, **378**, 491 (1995).
168. W. Götz, D. B. Oberman, and J. S. Harris, Jr., *Mat. Res. Soc. Symp. Proc.*, **378**, 527 (1995).
169. B. Pödör, *Phys. Stat. Sol.*, **16**, K167 (1966).
170. S. A. Ding, S. R. Barman, K. Horn, H. Yang, B. Yang, O. Brandt, and K. Ploog, *Appl. Phys. Lett.*, **70**(18), 2407 (1997).
171. D. W. Jenkins and J. D. Dow, *Phys. Rev.*, **B39**(5), 3317 (1989).
172. P. Boguslawski, E. L. Briggs, and J. Bernholc, *Phys. Rev.*, **B51**, 17255 (1995).
173. J. Neugebauer and C. Van de Walle, *Phys. Rev.*, **B50**, 8067 (1994).
174. M. Weyers, M. Sato, and H. Ando, *Jpn. J. Appl. Phys.*, **31**(7A), L853 (1992).
175. A. Rubio and M. L. Cohen, *Phys. Rev.*, **B51**, 4343 (1995).
176. S. H. Wei and A. Zunger, *Phys. Rev. Lett.*, **76**, 664 (1996).
177. K. Uesugi, I. Suemune, T. Hasegawa, T. Akutagawa, and T. Nakamura, *Appl. Phys. Lett.*, **76**(10), 1285 (2000).
178. M. Kondow, T. Kitatani, K. Nakahara, and T. Tanaka, *Jpn. J. Appl. Phys.*, **38**(12A), L1355 (1999).
179. K. Iwata, H. Asahi, K. Asami, R. Kuroiwa, and S. I. Gonda, *Jpn. J. Appl. Phys.*, **37**(3B), 1436 (1998).
180. S. Ruvimov, Z. Liliental-Weber, J. Washburn, T. J. Drummond, M. Hafich, and S. R. Lee, *Appl. Phys. Lett.*, **71**(20), 2931 (1997).
181. H. Chen, H. F. Liu, Z. Q. Li, S. Liu, Q. Huang, J. M. Zhou, and Y. Q. Wang, *J. Cryst. Growth*, **201/202**, 336 (1999).
182. H. D. Jung, N. Kumagai, T. Hanada, Z. Zhu, T. Yao, T. Yasuda, and K. Kimura, *J. Appl. Phys.*, **83**(10), 5497 (1998).
183. J. Lu, L. Haworth, P. Hill, D. I. Westwood, and J. E. Macdonald, *J. Vac. Sci. Technol.*, **B17**(4), 1659 (1999).

184. G. Feuillet, H. Hamaguchi, K. Ohta, P. Hacke, H. Okumura, and S. Yoshida, *Appl. Phys. Lett.*, **70**(8), 1025 (1997).
185. J. Neugebauer, T. Zywietz, M. Scheffler, J. E. Northrup, and C. G. Van de Walle, *Phys. Rev. Lett.*, **80**(14), 3097 (1998).
186. S. Yoshida, T. Kimura, J. Wu, J. Kikawa, K. Onabe, and Y. Shiraki, *MRS Internet J. Nitride Semicond. Res.*, **5S1**, W3.41 (2000).
187. T. S. Cheng, L. C. Jenkins, S. E. Hooper, C. T. Foxon, J. W. Orton, and D. E. Lacklison, *Appl. Phys. Lett.*, **66**(12), 1509 (1995).
188. B. Ya. Ber, A. V. Merkulov, S. V. Novikov, V. V. Tret'yakov, T. S. Cheng, C. T. Foxon, L. C. Jenkins, S. E. Hooper, D. E. Lacklison, and J. W. Orton, *Semiconductors*, **30**(3), 293 (1996).
189. H. Okumura, H. Hamaguchi, G. Feuillet, Y. Ishida, and S. Yoshida, *Appl. Phys. Lett.*, **72**(23), 3056 (1998).
190. T. Mattila and A. Zunger, *Phys. Rev. B*, **58**(3), 1367 (1998).
191. T. Mattila and A. Zunger, *Phys. Rev. B*, **59**(15), 9943 (1999).
192. W. M. Jadwisienczak and H. J. Lozykowski, *MRS Symp. Proc.*, **482**, 1033 (1998).
193. X. Li, S. Kim, E. E. Reuter, S. G. Bishop, and J. J. Coleman, *Appl. Phys. Lett.*, **72**(16), 1990 (1998).
194. A. F. Tsatsul'nikov, B. Ya. Ber, A. P. Kartashova, Yu. A. Kudryavtsev, N. N. Ledentsov, V. V. Lundin, M. V. Maksimov, A. V. Sakharov, A. S. Usikov, Zh. I. Alferov, and A. Hoffmann, *Semiconductors*, **33**(7), 728 (1999).
195. A. Stötzler, R. Weissenborn, M. Deicher, and ISOLDE Collaboration, *MRS Symp. Proc.*, **595**, W12.9 (2000).
196. H. Siegle, I. Loa, P. Thurian, G. Kaczmarczyk, L. Filippidis, A. Hoffmann, C. Thomsen, D. Schikora, M. Hankeln, and K. Lischka, *Zeitschrift für Physikalische Chemie*, **200**, 187 (1997).
197. H. Siegle, A. Kaschner, A. Hoffmann, I. Broser, C. Thomsen, S. Einfeldt, and D. Hommel, *Phys. Rev. B*, **58**(20), 13619 (1998).
198. M. Ramsteiner, J. Menninger, O. Brandt, H. Yang, and K. H. Ploog, *Appl. Phys. Lett.*, **69**(9), 1276 (1996).
199. G. Kaczmarczyk, A. Kaschner, A. Hoffmann, and C. Thomsen, *Phys. Rev. B*, **61**(8), 5353 (2000).
200. S. Nakamura, T. Mukai, and M. Senoh, *Jpn. J. Appl. Phys.*, **30**, L1998 (1991).
201. J. Neugebauer and C. G. Van de Walle, *Festkörperprobleme*, **35**, 25 (1995).
202. J. Neugebauer and C. G. Van de Walle, *J. Appl. Phys.*, **85**(5), 3003 (1999).
203. J. W. Orton, *Semicond. Sci. Technol.*, **10**, 101 (1995).
204. B. Pödör, *Semicond. Sci. Technol.*, **11**, 827 (1996).
205. P. Boguslawski and J. Bernholc, *Phys. Rev.*, **56**(15), 9496 (1997).
206. P. Boguslawski, E. L. Briggs, and J. Bernholc, *Appl. Phys. Lett.*, **69**(2), 233 (1996).
207. F. Mireles and S. E. Ulloa, *Phys. Rev. B*, **58**(7), 3879 (1998).
208. A. Bosin, V. Fiorentini, and D. Vanderbilt, *MRS Symp. Proc.*, **395**, 503 (1996).
209. F. Bernardini, V. Fiorentini, and A. Bosin, *Appl. Phys. Lett.*, **70**(22), 2990 (1997).
210. C. E. C. Wood, D. Destimone, K. Singer, and G. W. Wicks, *J. Appl. Phys.*, **53**, 4230 (1982).
211. R. E. Honig and D. A. Kramer, *RCA Rev.*, **30**, 285 (1969).
212. B. Ya Ber, Yu A. Kudriavtsev, A. V. Merkulov, S. V. Novikov, D. E. Lacklison, J. W. Orton, T. S. Cheng, and C. T. Foxon, *Semicond. Sci. Technol.*, **13**(1), 71 (1998).
213. S. Guha, N. A. Bojarczuk, and F. Cardone, *Appl. Phys. Lett.*, **71(12)**, 1685 (1997).
214. P. D. Kirchner, J. M. Woodall, J. L. Freeouf, D. J. Wolford, and G. D. Petit, *J. Vac. Sci. Technol.*, **19**, 604 (1981).
215. J. Neugebauer and C. G. Van de Walle, *MRS Symp. Proc.*, **395**, 645 (1996).
216. M. Leroux, B. Beaumont, N. Grandjean, J. Massies, and P. Gibart, *MRS Symp. Proc.*, **449**, 695 (1997).
217. U. Kaufmann, M. Kunzer, M. Maier, H. Obloh, A. Ramakrishnan, B. Santic, and P. Schlotter, *Appl. Phys. Lett.*, **72**(11), 1326 (1998).
218. L. K. Teles, L. M. R. Scolfaro, J. R. Leite, L. E. Ramos, A. Tabata, J. L. P. Castineira, and D. J. As, *Phys. Stat. Sol. (B)*, **216**, 541 (1999).

219. L. Eckey, U. von Gfug, J. Holst, A. Hoffmann, B. Schineller, K. Heime, M. Heuken, O. Schön, and R. Beccard, *J. Cryst. Growth*, **189/190**, 523 (1998).
220. O. Brandt, in *Group III Nitride Semiconductor Compounds—Physics and Applications*, Ed. by B. Gil (Clarendon, Oxford, 1998), p. 417.
221. T. Yamamoto and H. Katayama-Yoshida, *MRS Symp. Proc.*, **468**, 105 (1997).
222. B. Monemar, O. Lagerstedt, and H. P. Gislason, *J. Appl. Phys.*, **51**, 625 (1980).
223. B. Monemar, H. P. Gislason, and O. Lagerstedt, *J. Appl. Phys.*, **51**, 640 (1980).
224. M. Boulou, G. Jacob, and D. Bois, *Rev. Phys. Appl.*, **13**, 555 (1978).
225. S. Nakamura, *J. Cryst. Growth*, **145**, 911 (1994).
226. S. Nakamura, T. Mukai, and M. Senoh, *Appl. Phys. Lett.*, **64**, 1687 (1994).
227. K. Wongchotigul, N. Chen, D. P. Zhang, X. Tang, and M. G. Spencer, *MRS Symp. Proc.*, **395**, 279 (1996).
228. C. R. Abernathy, J. D. MacKenzie, S. J. Pearton, and W. S. Hobson, *Appl. Phys. Lett.*, **66**(13), 1969 (1995).
229. Y. M. Houng, S. D. Lester, D. E. Mars, and J. N. Miller, *J. Vac. Sci. Technol. B*, **11**, 915 (1993).
230. U. Birkle, M. Fehrer, V. Kirchner, S. Einfeld, D. Hommel, S. Strauf, P. Michler, and J. Gutowski, *MRS Internet J. Nitride Semicond. Res.*, **4S1**, G5.6 (1999).
231. W. E. Hoke, P. J. Lemonias, P. S. Lyman, H. T. Hendricks, D. Weir, and P. Colombo, *J. Cryst. Growth*, **111**, 269 (1991).
232. K. Doverspike and J. I. Pankove, *Semiconduc. Semimet.*, **50**, 259 (1998).
233. E. F. Schubert, I. D. Goepfert, W. Grieshaber, and J. M. Redwing, *Appl. Phys. Lett.*, **71**(7), 921 (1997).
234. E. Iliopoulos, D. Doppalapudi, H. M. Ng, and T. D. Moustakas, *MRS Symp. Proc.*, **482**, 655 (1998).
235. X. Zhang, S.-J. Chua, W. Liu, and K.-B. Chong, *J. Cryst. Growth*, **189/190**, 687 (1998).
236. H. Tang, W. Kim, A. Botchkarev, G. Popovici, F. Hamdani, and H. Morkoc, *Solid-State Electron.*, **42**(5), 839 (1998).
237. N. G. Weimann, L. F. Eastman, D. Doppalapudi, H. M. Ng, and T. D. Moustakas, *J. Appl. Phys.*, **83**(7), 3656 (1998).
238. D. C. Look and J. R. Sizelove, *Phys. Rev. Lett.*, **82**(6), 1237 (1999).
239. J. L. Souchiere and V. T. Binh, *Surf. Sci.*, **168**, 52 (1986).
240. J. J. Hopfield, D. G. Thomas, and M. Gershenzon, *Phys. Rev. Lett.*, **10**(5), 162 (1963).
241. J. De-Sheng, Y. Makita, K. Ploog, and H. J. Queisser, *J. Appl. Phys.*, **53**(2), 999 (1982).
242. A. P. Abramov, I. N. Abramova, S. Yu. Verbin, I. Ya. Gerlovin, S. R. Grigorév, I. V. Ignatév, O. Z. Karimov, A. B. Novikov, and B. N. Novikov, *Semiconductors*, **27**(7), 647 (1993).
243. E. Burstein, *Phys. Rev.*, **83**, 632 (1954).
244. E. F. Schubert, *Doping in III-V Semiconductors* (Cambridge University Press, Cambridge, 1993), p. 38.
245. H. C. Casey, Jr. and F. Stern, *J. Appl. Phys.*, **47**, 631 (1976).
246. M. Yoshikawa, M. Kunzer, J. Wagner, H. Obloh, P. Schlotter, R. Schmitt, N. Herres, and U. Kaufmann, *J. Appl. Phys.*, **86**(8), 4400 (1999).
247. J. R. L. Fernandez, A. Tabata, J. R. Leite, A. P. Lima, V. A. Chitta, E. Abramov, D. J. As, D. Schikora, and K. Lischka, *MRS Internet J. Nitride Semicond. Res.*, **5S1**, W3.40 (2000).
248. D. C. Look, in *Electrical Characterization of GaAs Materials and Devices* (Wiley, Chichester, 1989), p. 67.
249. D. J. As and K. Lischka, *Phys. Stat. Sol. (A)*, **176**, 475 (1999).
250. S. Nakamura, T. Mukai, and M. Seno, *Jpn. J. Appl. Phys.*, **31**, 195 (1992).
251. X. Zhang, P. Kung, A. Saxler, D. Walker, and M. Razeghi, *J. Appl. Phys.*, **80**(1), 6544 (1996).
252. C. C. Yi and B. W. Wessels, *Appl. Phys. Lett.*, **69**, 3026 (1996).
253. J. D. Guo, M. S. Feng, and F. M. Pan, *Jpn. J. Appl. Phys.*, **34**, 5510 (1995).
254. H. M. Chen, Y. F. Chen, M. C. Lee, and M. S. Feng, *J. Appl. Phys.*, **82**(2), 899 (1997).
255. U. Kaufmann, M. Kunzer, H. Obloh, M. Maier, C. Manz, A. Ramakrishnan, and B. Santic, *Phys. Rev. B*, **59**(8), 5561 (1999).

256. L. Eckey, U. von Gfug, J. Holst, A. Hoffmann, A. Kaschner, H. Siegle, C. Thomsen, B. Schineller, K. Heime, M. Heuken, O. Schön, and R. Beccard, *J. Appl. Phys.*, **84**(10), 5828 (1998).
257. D. J. As, T. Simonsmeier, J. Busch, B. Schöttker, M. Lübbers, J. Mimkes, D. Schikora, K. Lischka, W. Kriegseis, W. Burkhardt, and B. K. Meyer, *MRS Internet J. Nitride Semicond. Res.*, **4S1**, G3.24 (1999).
258. Y. Kribes, I. Harrison, B. Tuck, T. S. Cheng, and C. T. Foxon, *J. Cryst. Growth*, **189/190**, 773 (1998).
259. C. Pernot, A. Hirano, H. Amano, and I. Akasaki, *Jpn. J. Appl. Phys.*, **37**, L1202 (1998).
260. P. Kozodoy, J. P. Ibbetson, H. Marchand, P. T. Fini, S. Keller, J. S. Speck, S. P. DenBaars, and U. K. Mishra, *Appl. Phys. Lett.*, **73**(7), 975 (1998).
261. J. H. Werner, *Appl. Phys. A: Solids Surf.*, **47**, 291 (1988).
262. V. A. Dimitiev, *MRS Internet J. Nitride Semicond. Res.*, **1**, 29 (1999).
263. N. Grandjean, J. Massies, P. Lorenzini, and M. Leroux, *Electron. Lett.*, **33**(25), 2156 (1997).
264. S. F. Chichibu, A. C. Abare, M. P. Mack, M. S. Minsky, T. Deguchi, D. Cohen, P. Kozodoy, S. B. Fleischer, S. Keller, J. S. Speck, J. E. Bowers, E. Hu, U. K. Mishra, L. A. Colderen, S. P. DenBaars, K. Wada, T. Sota, and S. Nakamura, *Mat. Sci. Eng.*, **B59**, 298 (1999).
265. X. L. Sun, Y. T. Wang, H. Yang, L. X. Zheng, D. P. Xu, and J. B. Li, *J. Appl. Phys.*, **87**(8), 3711 (2000).
266. A. P. Lima, A. Tabata, J. R. Leite, S. Kaiser, D. Schikora, B. Schöttker, T. Frey, D. J. As, and K. Lischka, *J. Cryst. Growth*, **201–202**, 396 (1999).
267. A. Tabata, A. P. Lima, L. K. Teles, L. M. R. Scolfaro, J. R. Leite, V. Lemos, B. Schöttker, T. Frey, D. Schikora, and K. Lischka, *Appl. Phys. Lett.*, **74**(3), 362 (1999).
268. R. Brenn, D. N. Jamieson, A. Cimmino, K. K. Lee, T. Frey, D. J. As, and S. Prawer, *Nucl. Inst. Meth.*, **B161–163**, 435 (2000).
269. R. Carles, N. Saint-Cricq, J. B. Renucci, M. A. Renucci, and A. Zwick, *Phys. Rev. B*, **22**, 4804 (1980).
270. G. Kaczmarczyk, A. Kaschner, S. Reich, A. Hoffmann, C. Thomsen, D. J. As, A. P. Lima, D. Schikora, K. Lischka, R. Averbeck, and H. Riechert, *Appl. Phys. Lett.*, **76**(15), 2122 (2000).
271. I. F. Chang and S. S. Mitra, *Phys. Rev.*, **172**, 924 (1968).
272. H. Grille, Ch. Schnittler, and F. Bechstedt, *Phys. Rev. B*, **61**(9), 6091 (2000).
273. R. Goldhahn, J. Scheiner, S. Shokhovets, T. Frey, U. Köhler, D. J. As, and K. Lischka, *Phys. Stat. Sol. (B)*, **216**, 265 (1999).
274. R. Goldhahn, J. Scheiner, S. Shokhovets, T. Frey, U. Köhler, D. J. As, and K. Lischka, *Appl. Phys. Lett.*, **76**(3), 291 (2000).
275. R. Goldhahn and S. Shokhovets, Optical Properties of III-Nitrides—Experiments, in *Optoelectronic Properties of Semiconductors and Superlattices*, M. O. Manasreh, Series Ed. (Gordon and Breach, Amsterdam, 2000).
276. J. R. Müllhäuser, O. Brandt, A. Trampert, B. Jenichen, and K. H. Ploog, *Appl. Phys. Lett.*, **73**, 1230 (1998).
277. A. F. Wright and J. S. Nelson, *Appl. Phys. Lett.*, **66**, 3051 (1995).
278. M. D. McCluskey, C. G. Van de Walle, C. P. Master, L. T. Romano, and N. M. Johnson, *Appl. Phys. Lett.*, **72**, 2745 (1998).
279. J. Holst, A. Hoffmann, D. Rudloff, F. Bertram, T. Riemann, J. Christen, T. Frey, D. J. As, D. Schikora, and K. Lischka, *Appl. Phys. Lett.*, **76**(20), 2832 (2000).
280. J. Holst, A. Hoffmann, I. Broser, D. Rudloff, F. Bertram, T. Riemann, J. Christen, T. Frey, D. J. As, D. Schikora, and K. Lischka, *Phys. Stat. Sol. (B)*, **216**, 471 (1999).
281. M. Pophristic, F. H. Long, C. Tran, I. Ferguson, and R. F. Karlicek, Jr., *Appl. Phys. Lett.*, **73**(24), 3550 (1998).
282. C. R. Abernathy, P. Wisk, F. Ren, and S. J. Pearton, *J. Vac. Sci. Technol. B*, **11**, 179 (1993).
283. T. L. Tansley and C. P. Foley, *Proc. 3rd Int. Conf. on Semi-Insulating III-V Materials*, Warm Springs, OR, Eds. D. C. Look and J. S. Blakemore (Shiva, Nantwich, England, 1984), p. 497–500.
284. T. L. Tansley and C. P. Foley, *Electron. Lett.*, **20**, 1066 (1984).
285. I. Ho and G. B. Springfellow, *Appl. Phys. Lett.*, **69**(18), 2701 (1996).

286. L. K. Teles, J. Furthmüller, L. M. R. Scolfaro, J. R. Leite, and F. Bechstedt, *Phys. Rev. B*, **62**(3), (2000).
287. T. Okumura, M. Ishida, and T. Kamikawa, *Jpn. J. Appl. Phys.*, **39**(3A), 1044 (2000).
288. K. P. O'Donnell, R. W. Martin, and P. G. Middleton, *Phys. Rev. Lett.*, **82**(1), 237 (1999).
289. E. Roca, C. Trallero-Giner, and M. Cardona, *Phys. Rev. B*, **49**(19), 13704 (1994).
290. P. Ramvall, P. Riblet, S. Nomura, Y. Aoyagi, and S. Tanaka, *J. Appl. Phys.*, **87**(8), 3883 (2000).
291. Y. Kayanuma, *Phys. Rev. B*, **38**(14), 9797 (1988).
292. R. W. Martin and K. P. O'Donnel, *Phys. Stat. Sol. (B)*, **216**, 441 (1999).
293. X. Q. Shen, P. Ramvall, P. Riblet, and Y. Aoyagi, *Jpn. J. Appl. Phys.*, **38**(4B) L411 (1999).
294. X. Q. Shen and Y. Aoyagi, *Jpn. J. Appl. Phys.*, **38**(1A/B) L14 (1999).
295. C. T. Foxon, S. E. Hooper, T. S. Cheng, J. W. Orton, G. B. Ren, B. Ya. Ber, A. V. Merkulov, S. V. Novikov, and V. V. Tret'yakov, *Semicond. Sci. Technol.*, **13**, 1469 (1998).
296. H. M. Chung, W. C. Chuang, Y. C. Pan, C. C. Tsai, M. C. Lee, W. H. Chen, and W. K. Chen, *Appl. Phys. Lett.*, **76**(7), 897 (2000).
297. F. Widmann, B. Daudin, G. Feuillet, N. Pelekanos, and J. L. Rouvière, *Appl. Phys. Lett.*, **73**(18), 2642 (1998).
298. C. Adelmann, R. Langer, E. Marinez-Guerrero, H. Mariette, G. Feuillet, and B. Daudin, *J. Appl. Phys.*, **86**(8), 4322 (1999).
299. O. Ambacher, *J. Phys. D: Appl. Phys.*, **31**, 2653 (1998).
300. J. A. Majewski, G. Zandler, and P. Vogl, *Semicond. Sci. Technol.*, **13**, A90 (1998).
301. M. E. Sherwin and T. J. Drummond, *J. Appl. Phys.*, **69**(12), 8423 (1991).
302. J. W. Matthews and A. E. Blakeslee, *J. Cryst. Growth*, **27**, 118 (1974).
303. M. Ramsteiner, O. Brandt, and K. H. Ploog, *Phys. Rev. B*, **58**(3), 1118 (1998).
304. H. Harima, T. Inoue, S. Nakashima, H. Okumura, Y. Ishida, S. Yoshida, T. Koizumi, H. Grille, and F. Bechstedt, *Appl. Phys. Lett.*, **74**(2), 191 (1999).
305. A. Nakadaira and H. Tanaka, *Jpn. J. Appl. Phys.*, **37**(3B), 1449 (1998).
306. T. Koizumi, H. Okumura, K. Balakrishnan, H. Harima, I. Inoue, Y. Ishida, T. Nagatomo, S. Nakashima, and S. Yoshida, *J. Cryst. Growth*, **201/202**, 341 (1999).
307. S. K. Pugh, D. J. Dugdale, S. Brand, and R. A. Abram, *J. Appl. Phys.*, **86**(7), 3768 (1999).
308. B. Daudin, F. Widmann, G. Feuillet, Y. Samson, J. L. Rouvière, and N. Pelekanos, *Mat. Sci. Eng. B*, **59**, 330 (1999).